



Chem Soc Rev

A review of composite solid state electrolytes for lithium batteries: Fundamentals, key materials and advanced structures

Journal:	<i>Chemical Society Reviews</i>
Manuscript ID	CS-SYN-03-2020-000305.R2
Article Type:	Review Article
Date Submitted by the Author:	26-Aug-2020
Complete List of Authors:	Zheng, Yun; University of Waterloo, Department of chemical engineering Yao, Yuze; University of Waterloo Ou, Jiahua; University of Waterloo Li, Matthew; University of Waterloo, Chemical Engineering Luo, Dan; University of Waterloo Dou, Haozhen; University of Waterloo, Chemical Engineering Li, Zhaoqiang; Shandong University, School of Mater Sci Eng Amine, Khalil; Argonne National Laboratory, Yu, Aiping; University of Waterloo, Chemical Engineering Chen, Zhongwei; University of Waterloo, Chemical Engineering

SCHOLARONE™
Manuscripts



Invited review

ARTICLE

A review of composite solid state electrolytes for lithium batteries: Fundamentals, key materials and advanced structures

Received 00th January 20xx,
Accepted 00th January 20xx

Yun zheng,^a Yuze Yao,^b Jiahua Ou,^a Matthew Li,^a Dan Luo,^a Haozhen Dou,^a Zhaoqiang Li,^a Khalil Amine,^c Aiping Yu,^a Zhongwei Chen^{a*}

DOI: 10.1039/x0xx00000x

www.rsc.org/

All-solid-state lithium ion batteries (ASSLBs) have been considered as the next-generation device for energy storage due to their advantages in safety and potentially high energy density. As the key component in ASSLBs, solid-state electrolytes (SSEs) with non-flammability and good adaptability to lithium metal anodes have attracted extensive attention in recent years. Among current SSEs, composite solid state electrolytes (CSSEs) with multiple phases have a more flexible approach to customize and combine the advantages of each single-phase electrolyte, which have been widely investigated recently and regarded as promising candidates for commercial ASSLBs. Based on existing investigation, this paper puts forth a comprehensive overview of recent developments in CSSEs. Here, we first introduce the historical development from solid-state ionic conductors to CSSEs, then summarize the fundamentals including mechanisms of lithium ion transport, key evaluation parameters, design principles, and key materials. Four main types of advanced structures for CSSEs are classified and highlighted according to recent progress. Moreover, advanced characterization and computational simulation techniques including machine learning are reviewed for the first time, main challenges and perspectives of CSSEs are also provided for future development.

1. Introduction of CSSEs

Increasing global consumption of fossil fuels and consequently undesired climate change, as well as environmental destruction are severe challenges to our humankind¹⁻³. Renewable storage and conversion are extremely important to deal with those challenges and should therefore be further developed.⁴⁻⁷ Among all current energy storage and conversion systems, lithium batteries, such as lithium-ion,^{8,9} lithium metal,¹⁰ and lithium-sulfur batteries,¹¹ are regarded as one of the most convenient and efficient devices for energy utilization due to their advantages such as high energy density, low self-discharge rate, long cycle life, light weight^{12,13}.

Lithium batteries with liquid electrolytes can present good performance, in which the electrolyte solutions can offer high conductivity and excellent wetting of electrode surfaces.¹⁴ However, the liquid electrolytes based on highly volatile and flammable organic solvent suffer from some drawbacks such as low ion selectivity, inadequate stability, and the huge challenge of safety concern especially.¹⁵ By comparison, the application of all-solid state lithium battery (ASSLB) can not only mitigate those persistent issues, especially for the safety and long-term electrochemical and thermal stabilities, but can also further improve the energy/power densities

and reduce the requirements for packaging and state-of-charge monitoring circuits^{12,16}. Due to these benefits, a rapidly increasing trend of investigations for solid state electrolytes used in lithium batteries has emerged in recent years.¹⁷⁻²⁰

Generally, the widely investigated SSEs can be divided into two main categories, including inorganic ceramic electrolytes and organic polymeric electrolytes. The former is commonly based on oxides and sulfides, the sulfide based ones, such as $\text{Li}_2\text{S}-\text{P}_2\text{S}_5$ and $\text{Li}_2\text{S}-\text{P}_2\text{S}_5-\text{MS}_x$, show significantly high ionic conductivities under room temperature ($10^{-4} - 10^{-2} \text{ S cm}^{-1}$) and good mechanical strength and flexibility.²¹ However, there are some drawbacks including low oxidation stability, sensitive to H_2O , and poor compatibility with cathode materials.²² Oxide based solid electrolytes such as garnet $\text{Li}_7\text{La}_3\text{Zr}_2\text{O}_{12}$ (LLZO), perovskite $\text{Li}_{1-x}\text{La}_x\text{TiO}_3$ (LLTO), NASICON (lithium superionic conductor) $\text{LiTi}_2(\text{PO}_4)_3$, and LISICON (sodium superionic conductor) $\text{Li}_{14}\text{Zn}(\text{GeO}_4)_4$ are widely studied because their good conductivity ($10^{-4} \text{ S cm}^{-1}$) and outstanding stability.²³ While the nature of ceramics is rigid and the corresponding electrolytes are difficult to process²⁴ (e.g. the Young's modulus of monocryalline oxide garnets LLZO is about 150 GPa²⁵). In brief, the ionic conductivity of inorganic SSEs is excellent while their mechanical properties and interfacial impedance with electrodes are undesirable, thus it is a challenge to achieve a large-scale manufacturing for further applications²⁶.

The latter type of SSEs usually consists of polymer (e.g. poly(ethylene oxide) (PEO), poly(vinylidene fluoride) (PVDF), polyacrylonitrile (PAN), and poly(methyl methacrylate) (PMMA)) as matrix and some lithium salts (e.g., LiClO_4 , LiTFSI ($\text{LiN}(\text{CF}_3\text{SO}_2)_2$), LiAsF_6 , and LiPF_6).^{1,27,28} Unlike crystalline inorganic electrolytes that are brittle, the features of organic polymer electrolytes are light,

^a Department of Chemical Engineering, Waterloo Institute for Nanotechnology, Waterloo Institute for Sustainable Energy, University of Waterloo, 200 University Avenue West, Waterloo, Ontario N2L 3G1, Canada.
Email: zhwchen@uwaterloo.ca

^b Department of Chemical and Biological Engineering, The Hong Kong University of Science and Technology, ClearWaterBay, Kowloon, HongKong

^c Chemical Sciences and Engineering Division, Argonne National Laboratory, 9700 Cass Ave, Lemont, IL 60439, USA.

flexible and scalable, which is compatible with electrode and more feasible to match with the state-of-the-art manufacturing process.¹³ While the thermal stability is limited, mechanical strength is insufficient (e.g. the Young's modulus of typical pristine PEO/LiTFSI is only 0.4 MPa.²⁹), dendrite growth at the electrolyte/electrode interface, and ionic conductivity which range from 10^{-6} to 10^{-5} S cm^{-1} typically at room temperature, is too poor to be accepted in commercial batteries. Although some methods are proposed to improve the ionic conductivity of polymer based SSEs, such as the further addition of lithium salts or the introduction of liquid plasticizers into the polymer matrix, the stability and/or the mechanical strength of polymer SSEs in most cases will worsened.^{30–32}

To overcome the shortcomings of the single-phase inorganic or polymer SSEs and even leverage their advantages, several recent researches proposed that the marriage of those two or more different components to form the composite solid-state electrolytes (CSSEs) have exhibited varying degrees of performance improvement and been considered as one of the most promising electrolytes in next-generation lithium batteries.^{33–35} Moreover, the CSSEs are also suitable for the development trend of flexible devices.

For better understanding of this topic, the early research process from solid state ionic conductors to current CSSEs is introduced first. As listed in Table 1, the development of solid electrolyte begins from the early 1830s, Faraday found that the solid Ag_2S and PbF_2 showed remarkable ionic properties at 177 °C and near 500 °C respectively, exhibiting conductivities comparable to metals³⁶. In 1851, Hittorf further investigated this problem and confirmed that the Ag_2S is decomposable via electrolysis. After that, an increasing number of solid ionic conductors were discovered³⁷.

In the end of the 19 century, people used the term “*solid electrolyte*” and discovered more influencing factors for their behaviours, which was typically introduced in a series of books *The Science of Electricity* edited by Wiedemann (1893–1898)³⁸. In 1899, Nernst proposed an anionic conductor as “glower” of electric lamp, which is made from ZrO_2 with some Y_2O_3 or CeO_2 . The particularly favourable composition is 85% ZrO_2 and 15% Y_2O_3 , which is so-called “*Nerst mass*” and further applied commercially^{39,40}. Frankly speaking, very few materials were developed as high ionic conductor in the solid state, especially under room temperature. However, the 1960s is a significant turning point for SSEs with high ionic conductivity, a typical sign is the term “*Solid State Ionics*”. In the early 1960s, Takahashi and Yamamoto developed a new solid electrolyte Ag_3SI , which had a very high Ag^+ conductivity of 1×10^{-2} $\Omega \text{ cm}^{-1}$ at 20 °C, and further proposed an all solid state battery of $\text{Ag}/\text{Ag}_3\text{SI}/\text{I}_2$ on this basis^{41,42}. In 1967, β -alumina, with the empirical formula $\text{Na}_2\text{O} \cdot 11\text{Al}_2\text{O}_3$, was reported by Yao and Kummer, which exhibited high Na^+ conductivity⁴³. On this base, Kummer and Weber proposed the first Na/S battery using β -alumina as solid electrolyte^{44,45}. Another case is the discovery of Ag_4MI_5 ($\text{M} = \text{Rb}, \text{K}, \text{NH}_4$ etc), a high-conductivity solid electrolyte proposed by Bradley and Greene in 1966–1967^{46,47} and further studies in 1970s⁴⁸. After the successful discoveries of high conductivity solid electrolytes, the related practical applications have then been developed rapidly^{16,49}.

In addition to inorganic solid ionic conductors mentioned above, a crystalline complexes of sodium and potassium salts with poly(ethylene oxide) (PEO) was reported in 1973⁵⁰, which is regarded

as solid polymeric electrolyte and thus extending the scope of solid state electrolyte into organic materials. In 1986, a new high energy density battery system with long life and good safety, so-called Zebra battery, was proposed by Coetzer et al., which is combination with a liquid sodium anode, a solid-state cathode, and a β -alumina electrolyte^{51,52}. Since 1980s, the term “*Solid State Ionics*” is widely recognized and this topic attracted increasing attention in worldwide.

Aside from the ionic (e.g. Ag^+ , Na^+ , O^{2-} etc.) solid electrolytes introduced above, Armand and co-workers perceptively proposed the solid polymeric electrolytes of “PEO+Li salts” system in 1979⁵³, and many subsequent researches were reported in the 1980s,^{54,55} which exhibit high lithium-ion conductivity. After these, various lithium-ion conductive polymer materials including PAN, PMMA and PVDF have been further developed for lithium batteries¹⁶. On the other hand, with respect to inorganic lithium-ion solid state electrolyte, a lithium phosphorus oxynitride (LiPON) material was exploited from Oak Ridge National Laboratory in 1992^{56,57}. Only one year later after the first commercialized lithium ion battery by Sony in 1991⁵⁸. Since then, several types of inorganic lithium-ion conductive materials have been widely investigated, including the oxide types such as perovskite, NASICON, LISICON, garnet, etc.; the sulfide types such as Li_2S – P_2S_5 , Li_2S – P_2S_5 – MS_x , etc; as well as the hydride type and halide type.

Furthermore, in 2000s, the scope of solid state electrolytes was widely expanded in emerging lithium metal batteries including lithium-air batteries, lithium-sulfur batteries and lithium-bromine batteries.^{16,32} Very recently, to further combine the advantages of two or more kinds of SSEs, CSSEs are proposed and used in ASSLBs to further improve their performance and safety. Generally, current researches of CSSEs used in ASSLBs can be divided into three categories, inorganic-organic CSSEs, organic-organic CSSEs and inorganic-inorganic CSSEs,^{27,59} the former is the most widely investigated and will be mainly focused in this review.

Despite the current market not yet fully embracing the CSSEs, patent applications as well as production scale for CSSE have risen significantly the past decade.^{60,61} Besides patents for specific solid electrolyte materials, most patented battery designs involve some sort of CSSE. Notably, Toyota announced large-scale production of a new Prius EV utilizing all-solid-state batteries by mid 2020s. From their published patents, it can be surmised that the general structure of at least one of their batteries utilizes a layered inorganic-inorganic CSSE where the anode contacting layer may be a thin layer of melted glass, a high conductivity ceramic bulk layer, and possibly a thin cathode-compatible inorganic solid electrolyte⁶². Ionic Materials[®] patented a layered organic-organic CSSE with one layer engineered specifically against the anode surface⁶³; PolyPlus[®] patented an organic-inorganic CSSE design involving a thin, but porous protective ceramic layer on the anode surface and a composite organic electrolyte or even liquid electrolyte as the bulk electrolyte which can also inhibit part of the porous ceramic layer⁶⁴. Rarely does a real world engineering application require only one element to achieve optimal success. Yet few systematic resources are yet available for researchers to review known interactions between different elements and structures of CSSE. Hence we have organized this comprehensive review to specifically focused on CSSEs used in ASSLBs, which is significant but rarely summarized in published review papers, although this subject is necessary and might have a great impact on the efforts

accelerating the progress of R&D as well as the technology's commercialization of lithium batteries.

In this review, the inorganic/polymer CSSEs used in lithium batteries will be focused. First, aside from the historical development of CSSEs introduced systematically above, the fundamentals such as the mechanisms for Li transfer in CSSEs will be illuminated in detail. Based on mechanism understanding and theoretical modelling, the key topics discussed in this paper include design principles and strategies, key materials and advanced structures, characterization and

analysis methods, in which the researches using machine learning are reviewed for the first time in this field. Finally, future research directions are proposed to address challenges for technology application and commercialization. We believe that this review paper would appeal to the scientific research, academic, and industrial communities worldwide, and also strongly believe that the CSSEs for lithium batteries can be widely used for energy storage and conversion with further research and development in the future.

Table 1 Early history from solid-state ionic conductors to composite solid-state electrolytes (CSSEs)

Time	Materials	Descriptions	Ref.
1834	Ag ₂ S and PbF ₂	Faraday discovered the remarkable ionic properties of Ag ₂ S and PbF ₂ at 177°C and near 500°C respectively.	36
1851	Ag ₂ S	Decomposable electrolytically	65
1893	--	The term 'solid Electrolyte' was in use	38
1899	ZrO ₂ with Y ₂ O ₃ or CeO ₂	Nernst produced the anionic conductor as a "glower".	39,40
1960s	--	the term "Solid State Ionics" was named.	42
1966	Ag/Ag ₃ SI/I ₂	An all solid state battery was proposed Takahashi and Yamamoto.	41,42
1967	β-alumina (Na ₂ O·11Al ₂ O ₃)	Exhibited high Na ⁺ conductivity.	43
1966-1967	Ag ₄ MI ₅ (M = Rb, K, NH ₄ etc)	A high-conductivity solid electrolyte proposed by Bradley and Greene.	46,47
1973	PEO with Na ⁺ and K ⁺ salts	Discovery of solid polymer electrolyte,	50
1979	PEO with Li ⁺ salts	"PEO+Li salts" system	53
1986-1987	Zebra battery with β-alumina electrolyte	Practical specific energy of 130 W·h·Kg ⁻¹ , long life (>1000 cycles), and high degree of safety.	51,52
1986	PEO/LiCF ₃ SO ₃ /polystyrene	"PEO+Li salts" system	54
1986	PEO/(LiClO ₄) _x	"PEO+Li salts" system	55
1992	LiPON	Propose of inorganic lithium-ion solid state electrolyte system	56,57

* PEO, poly(ethylene oxide); LiPON, lithium phosphorus oxynitride.

2. Fundamentals of lithium ionic transport in solid state electrolytes

The optimization and development of SSEs with high ionic conductivities and high stabilities are significantly important for further application of ASSLBs, which depend on a better understanding of fundamentals of SSEs⁶⁶. Therefore, the fundamentals of each component in CSSEs are introduced in this section.

2.1. Basic structures and electrochemical processes of ASSLBs with CSSEs

The basic structure of ASSLBs with CSSEs is shown in Fig. 1 (a), which is consisted of an anode, a cathode and the CSSE, here the electrolyte acts as a lithium ionic conductor and a separator. Specifically, according to the currently proposed structures and components of CSSEs, we summarized them into four main categories, as shown in Fig. 1 (b) to (d), including (1) inorganic fillers in polymer matrix, where fillers are range from 0D to 2D, (Fig. 1(b)), (2) heterogeneous layered structure (Fig.1 (c)), (3) 3D inorganic continuous frameworks with polymer infiltration (Fig.1(d)), and (4)

open-framework related composite electrolytes, some open-framework materials combined with polymers or other matrixs show similar structures (Fig. 1(b)).

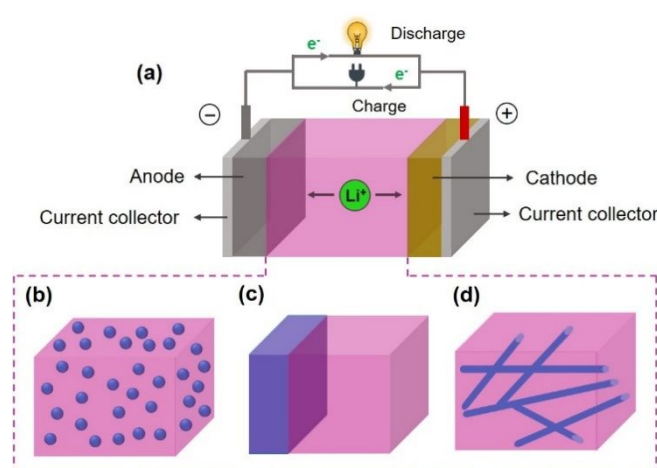


Fig. 1 Schematic diagram of all-solid-state lithium batteries (ASSLBs) with various composite solid state electrolytes (CSSEs). (a) structure of ASSLBs, (b) nanoparticle filled in matrix, (c) heterogeneous layered structure, (d) inorganic continuous framework with filled polymer, all these schematics are presented as a sample for each category.

As for the electrochemical processes, it is similar to those in the lithium ion battery with liquid electrolytes. During charging, lithium ions are de-intercalated from the crystal structure of cathode (e.g. LiFePO₄) and then conducted across the CSSEs into the anode (e.g. lithium foil), while the generated electrons transfer from cathode to anode via the external circuit. On the other hand, the processes are opposite during the discharge for providing energy. It is worth mentioning that the lithium ion transport process in CSSEs is more complicated than that of common pure electrolyte, which will be introduced in detail in following sections.

2.2. Key parameters to evaluate the performance of CSSEs

To better understand the CSSEs, some important physico-chemical parameters in performance optimization of CSSEs are summarized in this section, which includes ionic conductivity, ion transport number, thermodynamic properties, chemical stability, and electrochemical stability⁶⁷.

(1) Ionic conductivity

As one of the most important indicators to evaluate a SSE, lithium ionic conductivity (σ) is highlighted here. In general, the ionic conductivity can be modelled with reference to Arrhenius or/and Vogel–Tammann–Fulcher (VTF) behaviours,^{67–69} the former is usually used to describe ionic transport in inorganic/ceramic solid electrolyte materials, which is related to the lattice defects mechanism and will be introduced in detail later, and also the ionic transport in some crystalline polymers. The conductivity can be expressed as the sum of all the moving charged species (i), and the Arrhenius behavior of ionic conductivity can be shown as the following Eqn (1).^{70,71}

$$\sigma = \sum_i q_i c_i \mu_i = \sigma_0 \exp\left(\frac{-E_a}{kT}\right) \quad (1)$$

where the q_i , c_i , μ_i are the charge number, charge concentration, and the mobility of the charged species, respectively. σ_0 is the pre-exponential factor, which is related to the number of charge carriers, E_a is the activation energy for lithium ionic conductivity; k and T are the Boltzmann constant and temperature. More details of the derivative process of this equation from ionic hopping probability (p), hopping frequency (ν) and motional free energy (ΔG_m) can be seen in the reference⁷¹.

With respect to solid polymer electrolyte materials, ionic transport is achieved by intra- or inter-chain hopping which is coupled with the movement of segmental polymer chain with sequential coordinated sites. Although some controversial points still exist, the prevailing view to describe the ionic conductivity behaviour in amorphous solid polymer is the VTF model, as shown in Eqn (2)^{32,67}:

$$\sigma = \sigma_0 T^{-\frac{1}{2}} \exp\left(-\frac{B}{T-T_0}\right) \quad (2)$$

where B is so-called pseudoactivation energy, which is expressed in units of E_a/k ; and the T_0 is reference temperature and about 10 to 50 K lower than the glass transition temperature (T_g). VTF behaviours are generally observed in solid polymer electrolytes above the glass transition temperature (T_g) of the polymer matrix.⁶⁷

When it comes to the CSSEs, those two equations will be combined to calculate the overall conductivity, depending on their specific compositions and structures. For instance, the ion conduction behavior in binary polymer (polymer with lithium salt) or nanofillers/polymer (namely, polymer, lithium salt, and additive) CSSEs are also described by VTF model showed as Eqn (2) commonly. Some mechanisms and calculation models for the ionic

conductivity at local interfacial region in CSSEs with various structures are also proposed and would be further introduced later.

(2) Li⁺ ion transference number

In addition to ionic conductivity, Li⁺ transference (or transport) number (t_B) is also an important parameter to evaluate the process occurred in CSSEs. To be specific, the electrolyte with a high t_B can enable a fast charge–discharge capability even with relatively low ionic conductivity,^{72,73} suppression of the lithium dendrite,⁷⁴ and even long-cycling with Li metal anode.^{75,76} The t_B of a given ion B in solution is defined as the contributed fraction of the total current carried through the electrolyte by this ion B, namely, the $t_B = I_B/I$. Where the I_B is the contributed current carried by ion B and the I is total current carried through the electrolyte. The overall transference number is $\sum t_B = \sum t_+ + \sum t_-$, where the t_+ and t_- are the transference number of cations and anions, respectively. For a single salt of monovalent ions, where the ions in the same electric potential gradient, the t_B can be presented as below:

$$t_+ = \frac{\mu_+}{\mu_- + \mu_+} \quad t_- = \frac{\mu_-}{\mu_- + \mu_+} \quad (3)$$

where the μ_+ and μ_- are the ionic mobilities of cations and anions, respectively, with the unit of $\text{m}^2 \cdot \text{s}^{-1} \cdot \text{V}^{-1}$. There are some methods including Hittorf method⁷⁷, boundary moving method⁷⁸, and EMF (Electromotive Force) method⁷⁹, which are usually applied to the research of liquid electrolyte. Regarding the solid electrolytes (e.g. polymer electrolyte especially) for lithium batteries, Bruce *et al.*⁸⁰ proposed the ac/dc method based on the steady state technique to combine the dc polarization and impedance spectroscopy to determine the t_B value. In this regard, a small dc pulse is applied on a symmetrical Li|solid electrolyte|Li cell, then the initial (I_0) and steady-state (I_{ss}) current which flow through the cell, as well as the initial (R_0) and steady states (R_{ss}) resistance of the two Li interfaces are measured to calculate the transference number of Li⁺ ion (t_{Li^+}) according to the Evans–Vincent–Bruce equation^{80–82}, as shown in Eqn (4):

$$t_{Li^+} = \frac{I_s(\Delta V - I_0 R_0)}{I_0(\Delta V - I_s R_s)} \quad (4)$$

Where the ΔV is for dc pulse, namely, the dc polarization voltage applied across the solid electrolyte. Unlike the solid polymer electrolytes, the inorganic solid electrolytes, especially the oxides based inorganic electrolyte, are commonly used as a single lithium ion conductor, thus the transference number of them is roughly equal to one. On the other hand, as another established, non-electrochemical method, Pulse Magnetic Field Gradient (PMFG) NMR (Nuclear Magnetic Resonance) can also be used for measuring the self-diffusion coefficients (D_i) and calculating t_{Li^+} and according to Eqn (5):⁸³

$$t_{Li^+} = \frac{D_+}{D_+ + D_-} \quad (5)$$

Where the D_+ and D_- are the self-diffusion coefficients of cations and anions, respectively. And it is noticeable that the ion–ion interactions is assumed negligible in this method.

When it comes to the inorganic/polymer CSSEs, some researchers still use the Evans–Vincent–Bruce equation to calculate the t_B value. For instance, J Ou *et al.*⁸⁴ developed an ionic liquid-assisted PEO-LAGP (Li_{1.5}Al_{0.5}Ge_{1.5}P₃O₁₂)-EMITFSI (Lithium bis(trifluoromethane-sulfonyl) imide) composite electrolyte for

advanced solid state lithium ion batteries, in which the t_{Li^+} was calculated with reference to the Evans–Vincent–Bruce equation. This model might be able to match the CSSE consisting of polymer and a few ceramic particles, but other models and related equations need to be further developed for other advanced structural CSSEs, such as interconnected nanowires or three-dimensional (3D) framework, even the vertically aligned structure mentioned above.

(3) Mechanical property

Mechanical properties are those which affect the mechanical strength and ability of a material to be molded in suitable shape, which include strength, toughness, brittleness, hardness, resilience, and so on.⁸⁵ When it comes to SSEs used in lithium batteries, their mechanical strength, i.e. the ability to withstand the stress of physical forces, plays an important role in lithium batteries with long cycling, high energy density and high voltage.²³ Typically, the indicators of Yang's elastic moduli (E , MPa) and shear moduli (G , MPa) as defined in Eqns (6) and (7) respectively, are widely used to describe the mechanical strength.^{25,86}

$$E = V_l^2 \rho \frac{(1 + \nu)(1 - 2\nu)}{(1 - \nu)} \quad (6)$$

$$G = \frac{E}{2(1 + \nu)} \quad (7)$$

where V_l is Longitudinal velocity, ρ is the density, ν is Poisson's ratio (e.g. $\nu = 0.257$). Those parameters can be measured by techniques such as acoustic impulse excitation, nanoindentation, etc.²⁵ In addition to the Yang's moduli and shear moduli, some other indicators including maximum stress (MPa), strain at break (mm mm^{-1}), and toughness (MJ m^{-3}) are also very useful to describe the mechanical properties of SSEs used in lithium batteries.⁸⁵

(4) Electrochemical stability

A good electrochemical stability should also be considered in the design of the electrolyte for lithium batteries. To be specific, some parameters, including electrode/solid electrolyte interfacial resistance, solid electrochemical interface (SEI) formation, and the materials' electrochemical behaviors during battery cycling tests are measured by electrochemical impedance spectroscopy (EIS)⁶⁷. For lithium batteries, SEIs are formed thermodynamically favorably at the electrode-electrolyte interfaces, especially with incompatible electrode-electrolyte interfaces and may consume the electrolyte such as in the case of liquid electrolyte and lithium anode. This will limit both operating voltage and deliverable capacity. The interfacial behavior can be evaluated by the resistance change during the running of a symmetrical Li|electrolyte|Li cell. The imaginary (Z'') and real (Z') part of Nyquist plot measured from impedance spectroscopy can be separated and analysed into various resistances contributed from bulk, grain boundary and the electrode/electrolyte interfacial region. The interface between electrode and solid electrolyte behaves like a parallel resistance–capacitance circuit (RC) and can be presented as a semicircle in Nyquist plot.

Aside from interfacial resistance with operation time measured by EIS, the range of electrochemical window, namely, the reduction and oxidation potential limits, is also an important indicator to evaluate the electrochemical stability of a solid electrolyte. Specifically, electrolytes with wide electrochemical window is conducive to obtain a better interfacial stability and compatibility with higher voltage operation, thus further enhancing energy density of lithium batteries.^{87,88} In general, the electrochemical window is

measured by applying linear sweep voltammetry (LSV) or cyclic voltammetry (CV) on a standard or half-cell configuration, the latter is usually consisted of a solid electrolyte, a Li metal used both as a reference and counter electrode, and a cathodic current collector as the working electrode. For instance, K. Fu *et al.*⁸⁹ proposed an SSE with 3D garnet nanofiber networks for lithium batteries, the results of the LSV on Li|electrolyte|stainless steel half-cell showed a wide electrochemical window range from 0 to 6 V vs. Li/Li⁺. Moreover, in addition to experiments, density functional theory (DFT) simulations are also performed to pre-evaluate the electrochemical stability for SSEs⁹⁰. For instance, the thermodynamic electrochemical stability window of typical solid electrolytes $\text{Li}_{10}\text{GeP}_2\text{S}_{12}$ and cubic $\text{Li}_7\text{La}_3\text{Zr}_2\text{O}_{12}$ are calculated using first principles computation and combining with an experimental method to identify their intrinsic stability windows⁹¹.

(5) Battery test

The final battery performance is usually regarded as one of the most important evaluation indicators in a research work, in addition to evaluating the performance for SSEs separately, the feasibility and stability of them worked as a component in an assembled lithium battery is of the essence. The anode|electrolyte|cathode and/or symmetrical Li|electrolyte|Li cells are usually assembled and cycled in an appropriate voltage range to study the cycling behavior with various temperatures, current densities, and/or discharge rates (C)⁶⁷. Based on this method, the specific capacity ($\text{mA}\cdot\text{h}\cdot\text{g}^{-1}$) and the charging/discharging efficiency can be calculated according to the obtained voltage profile of the continued lithium plating/stripping cycling with time.

Aside from those parameters measured via electrochemical methods mentioned above, some other points such as thermal properties and chemical stability are also important for solid electrolyte materials, which can be evaluated by differential scanning calorimetry (DSC) and thermogravimetry (TGA).

2.3. Mechanisms of Li ionic transport in CSSEs

Mechanisms of Li ionic transport in SSEs need to be highlighted first, because the lithium ion conductivity can be regarded as one of the most important indicators to evaluate the performance of a solid state electrolyte. The understanding of the Li ionic transport mechanism is also crucial for designing and optimizing the high conductive SSEs. For CSSEs, the lithium ions can transfer in the inorganic, organic, or their interfacial regions of the CSSE. Lithium ions may transfer in only one and up to all three regions. More details for the theories of Li-ion conduction in CSSEs are presented as follows.

2.3.1. Mechanisms of Li ionic transport in active inorganic region

In crystalline solid materials, ionic conductivity strongly relies on the defects of the crystal structure, which mainly includes point defects, line defects, planar defects, volume defects, and electron defects⁶⁶. Among them, the point defects play an important role in lithium ions diffusion mechanisms, the schematic diagram of some typical point defects is shown in Fig. 2(a)¹⁶. The most representative point defects are the Frenkel defect (anion vacancy accompanied by a cation interstitial) and Schottky defect (cation vacancy accompanied by anion vacancy). To be specific, the mechanisms based on point defects can be divided into vacancy (defect) mechanisms and non-

vacancy (non-defect) mechanisms, in which the former category includes simple vacancy mechanism and vacancy mechanism, and the later one includes interstitial mechanism, collective mechanism, and interstitial-substitutional exchange mechanism⁹².

The schematic of vacancy mechanism is shown in Fig. 2(b), where the Lithium ions can move from the previous equilibrium position to the adjacent vacancy to achieve the diffusion⁹³. Much smaller lattice strain during atom hopping is involved for vacancy mechanism, which leads to a much lower activation energy barrier. Obviously, the transport kinetics are primarily influenced by vacancy concentration in the lattice, which can well explain the different lithium migration pathway and energy barrier for mono-vacancy and more vacancies (diffusion via aggregates of vacancies)⁹⁴. Moreover, some other factors such as the category of ions near the diffusion path, or the configuration and distance of the surrounding vacancy or the doped cations can also affect the energy barrier of lithium ions diffusion⁹⁵.

Regarding the non-vacancy mechanisms, one of the representatives is interstitial mechanism, which including the direct interstitial diffusion and the interstitial knock-off diffusion, as shown in Fig. 2 (c) and (d). For the former, the interstitial ion can directly move to an adjacent interstitial site, which is called direct interstitial mechanism. Generally, the interstitial atoms are much smaller than the matrix ones, and a large lattice strain will be formed during this migration process. The other interstitial diffusion is indirect, while it is commonly observed for lithium ions diffusion in lithium ion

batteries, especially for high lithium ion concentration. In this case, the interstitial atom first kicks the matrix atom, and this removed matrix atom subsequently migrates to another adjacent interstitial site, as shown in Fig. 2 (d). The size of interstitial atom can be similar or even the same as the matrix one. This indirect interstitial diffusion mechanism is known as knock-off mechanism or also can be regarded as a collective mechanism, which is due to that there are at least two atoms moving simultaneously in this process⁹².

Another situation can be referred to as interstitial-substitutional exchange mechanism, which is also a collective mechanism and can be divided into two categories. The direct exchange and the ring diffusion are as shown in Fig. 2(e). For the former, two atoms move simultaneously and swap the lattice sites with each other, and in the latter, a group of atoms (three or more) move as a ring for one atom distance to new positions. Comparing with vacancy mechanism, the non-vacancy mechanisms, namely the non-defects diffusion, is much more difficult because of the higher migration barrier energy. Similar to the diffusion mechanisms in inorganic crystalline electrolyte, the lithium ionic transport process in inorganic amorphous materials (typically glass) also involves the migration from one local site into the neighboring sites^{16,96}. Aside from framework and ionic arrangement, the interaction between the structural skeleton and charge carriers is also important during the diffusion process. However, some inorganic solid electrolyte materials can't be clearly distinguished into ceramics or glasses, the lithium ion diffusion process should be further confirmed.

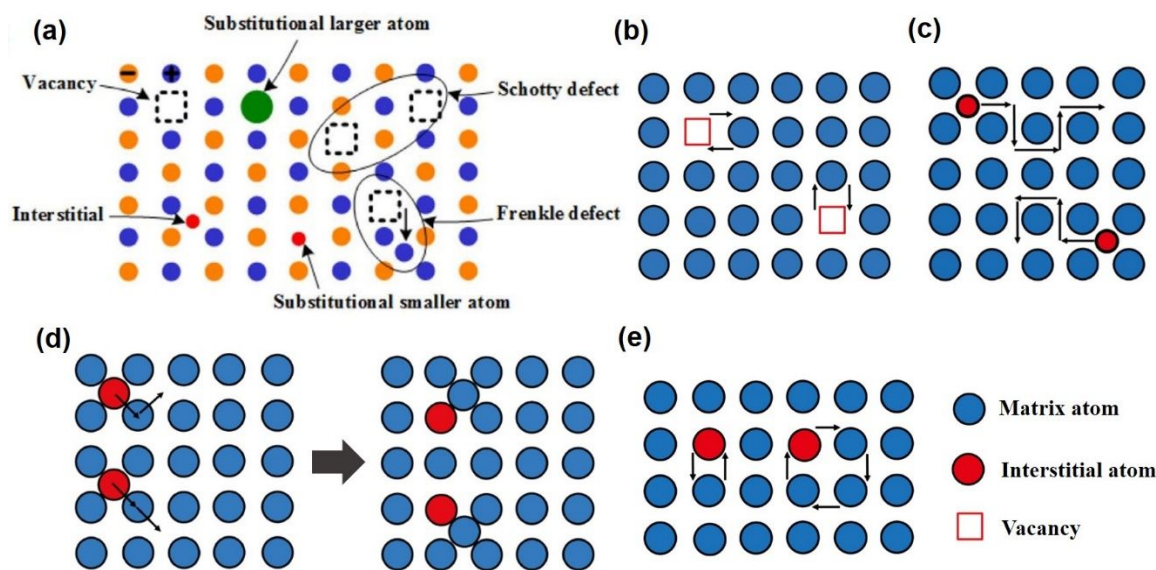


Fig. 2 schematic diagram of (a) some typical point defects in inorganic part of CSSEs⁶⁶, reprinted with permission from ref. 66. Copyright 2018, Elsevier Ltd. (b) vacancy diffusion mechanism, (c) direct interstitial mechanism, (d) interstitial knock-off mechanism, and (e) direct exchange and ring mechanism⁹⁷. Reprinted with permission from ref. 97. Chinese Physical Society and IOP Publishing Ltd.

2.3.2. Mechanisms of Li ionic transport in active organic (polymer) region

In most cases, organic (polymer) electrolytes are usually used as the matrix in CSSEs. The polymer electrolyte materials for lithium batteries can be divided into two classes, gel polymer and dry polymer, the latter one can be used in ASSLB and will be focused in this review

article. In general, lithium salts (Li^+ and anion groups.) are commonly added and dissolved in the solid polymers with sequential polar groups (e.g. $-\text{O}-$, $=\text{O}$, $-\text{S}-$, $-\text{N}-$, $-\text{P}-$, $-\text{C}=\text{O}$, and $-\text{C}=\text{N}$) to enable the lithium ionic conductivities of polymer based solid electrolytes⁹⁸. The mechanisms of Li ionic transport in solid polymer electrolyte swollen

with lithium salts will be introduced in this section, which mainly includes free-volume model and ion conduction model⁸³.

Generally speaking, ion transport in solid polymer electrolytes mainly occurs in amorphous regions above their T_g .^{99,100} Accordingly, the free-volume model and related derived theories are widely accepted to describe ionic transport mechanism in amorphous regions. Specifically, the lithium ions are located at suitable coordination sites (e.g., $-O-$ in polyethylene oxide, $-CN$ in polyacrylonitrile, $-NR$ in polyamide, etc.) of the segmental chain. And the polymer chains undergo local segmental motions in a quasi-liquid behavior, as if there are some free volume around it. Thus the Li^+ can hop from one coordination site to the others through these free volumes in one chain or between different chains under the effect of an electric field.^{98,101} The relationship between temperature and ion conductivity based on free-volume model can be described by the VFT equation mentioned above.

In addition to the ionic transport mechanism mainly in amorphous regions, ionic conduction model can be applied in crystalline phases of solid polymer electrolytes, in which the Li^+ transport is less dependent on the segmental motion and can be mainly described by the Arrhenius equation. Although it's widely recognized that the ionic transport kinetics in amorphous regions with activated chain segments is much faster than that in crystalline phase before,^{102,103} it's verified that the ionic transport in crystalline phases can be achieved and even higher than that in amorphous in more and more cases. Gadjourova et al. proposed that ionic conductivity of crystalline phase in the static, ordered environment can be higher than the equivalent amorphous phase above T_g .¹⁰⁰ As shown in Fig. 3, in the crystalline phase of PEO_6LiXF_6 ($X = P, As$ or Sb), the pairs of polymer (the PEO) chains fold to form cylindrical tunnels, within which the lithium ions are located at the coordination sites ($-O-$ in PEO), while the anions XF_6^- are located outside and uncoordinated by the anions. In this structure, the Li^+ ions can transfer along the tunnels via the adjacent coordination sites, which is without the aid of segmental motion of polymer chains^{98,104}. On this basis, Stoeva¹⁰⁴, Christie¹⁰⁵, Zhang¹⁰⁶ and Lilley¹⁰⁷ et al. in the same group also proposed that the ionic conductivity can be improved by 1.5 to 2 orders of magnitude with further modification for these stoichiometric crystalline complexes by replacing the XF_6^- ions.

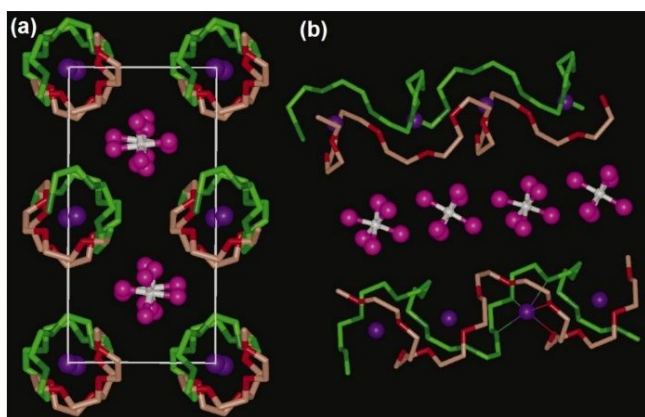


Fig. 3 The structure of a typical solid polymer electrolyte material (poly(ethylene oxide)₆LiAsF₆) (a) view along the chain axis for Li^+ transport pathway, (b) view of relative position of the chains and their conformation. (Blue, Li; white, As; pink, F; light and dark greens are for C and O in chain 1; light and dark reds are for C and O in chain 2)^{100,108}. Reprinted with permission from ref. 100,108. Copyright 2001 and 1999 Nature Publishing Group.

light and dark greens are for C and O in chain 1; light and dark reds are for C and O in chain 2)^{100,108}. Reprinted with permission from ref. 100,108. Copyright 2001 and 1999 Nature Publishing Group.

In short, the ion transport mechanisms in polymer electrolyte materials is a complex and even controversial topic, which is due to the nature of those materials, depending on the factors such as the temperature, polymer type, molecular weight, polymer structure, dissociation ability and concentrations of Li salts in polymers, etc.⁸³. It seems that mechanisms of Li ionic transport in polymer phase is still not fully understood and needs continued research endeavor.

2.3.3. Mechanisms of Li ionic transport at interfacial region

In general, there are three parts for each CSSE, including the bulk of each of the main components, and their interfacial regions. The components can be the inorganics or the organics (typically polymer). Moreover, the main components are either passive, active, or a combination of both. A case in point is the inorganic/polymer CSSEs, where the inactive component such as SiO_2 , Al_2O_3 , and ZrO_2 can be used as the fillers in polymer matrix, or the frameworks with filled polymer¹⁰⁹, so do the active components such as LLZO, LLTO, LATP. On the other hand, the polymer can also be divided into passive or active in CSSEs. For example, polyimide (PI)/PEO with lithium salt, namely the polymer/polymer CSSE, was proposed by Jiayu Wan *et al.*³¹, in which the PI acted as the passive structure and provided the aligned framework for the active component, PEO.

The mechanisms of Li^+ ion transport in the bulks of those active inorganic or polymer electrolytes have been introduced in the previous section. However, the mechanism at interfacial regions are much more complicated and largely depends on the specific constitution and structure of the various CSSEs. Regarding one typical type of CSSEs, which consists of inactive inorganic fillers and active polymer matrix, there are two reasons to explain the conductivity improvement at interfacial regions: (1) the addition of inorganic fillers can modify the local structure of polymer chains by decreasing their crystallinity and glass transition temperature. And (2) the inorganic fillers can also help the further dissociation of Li salts according to the Lewis acid-base theory³². More details will be introduced case by case in Chapter 3.

2.4. Performance requirements for CSSEs

In an ASSLB with CSSEs, the electrolyte is sandwiched between the cathode and anode, playing a crucial role in the electrochemical performance and stability of batteries during long term operation. Based on the fundamental parameters described in this section, the performance requirements include high ionic conductivity, appreciable Li^+ transference number, good electrochemical stability, excellent chemical and thermal stability, as well as preferable mechanical strength and flexibility⁹⁸. More details are introduced below.

(1) High ionic conductivity

In general, the ionic conductivity (σ) for a solid electrolyte should be higher than $10^{-3} S \cdot cm^{-1}$ at ambient temperature and even enhanced to reach that of traditional liquid electrolytes ($10^{-2} S \cdot cm^{-1}$)¹¹⁰. For CSSEs, one of the biggest challenges for all-solid-state polymer electrolyte is lower ionic conductivity for practical application. Furthermore, it is much more preferable to organics (e.g. the σ of PEO

is about 10^{-4} S·cm⁻¹ under 65-78°C¹⁶). While some ceramic electrolytes have achieved ionic conductivities in the range of 10^{-2} S cm⁻¹, that can only be achieved with a dense pellet with high interfacial resistance, is not a practical stand-alone candidate. Therefore, CSSEs can further facilitate ionic transport and self-discharge can be minimized during battery operation⁹⁸, and is more comparable with the ionic conductivities of liquid electrolytes (10^{-2} to 10^{-3} S·cm⁻¹ typically).

(2) Appreciable Li⁺ ion transference number

The concentration polarization of electrolyte can be reduced with larger Li⁺ ion transference number (t_{Li^+}), which can further improve power density⁹⁸. The t_{Li^+} for typical inorganic solid electrolytes is close to one, which is definitely preferable to that of CSSEs which may contain polymer components with lower t_{Li^+} . Therefore, some strategies need to be taken for improving the t_{Li^+} of CSSEs before structure designing or material selection. For instance, reducing the mobility of anions in polymer components of CSSEs is an effective strategy to increase the t_{Li^+} significantly⁹⁸ by anchoring anions to the polymer backbone^{111,112} or introducing anion receptors to complex with anions selectively¹¹³ can work for this purpose.

(3) Good electrochemical stability

In order to ensure the reversibility and stability of oxidation reaction and the reduction reaction, the electrolyte must be attached to both cathode and anode. For this purpose, the reduction potential limit should be lower than that of lithium metal in anode and the oxidation potential limit should be higher than embedding potential of lithium ions in the cathode⁹⁸. Therefore, the difference between the potentials of the oxidation reaction and the reduction reaction, namely, the electrochemical window should be wide enough to guarantee the reversibility and long term life cycle of the battery. To enable the highest voltage output of a ASSLB, a wide electrochemical stability window (0.0–5.0 V) is desired for an ideal CSSE⁹¹.

(4) Excellent chemical and thermal stability

Side reactions should be avoided when the solid electrolyte is in contact with the two electrodes, thus the basic requirement for a SSE is chemical stability with the contacting components, which is a little more difficult for CSSEs which consist of two or more different parts to ensure safety, charge retention, and life cycle of the battery. On the other hand, it's very promising if the lithium battery can be operated under a wider temperature range, thus the thermal stability for the materials of CSSE is also very important for basic research and even further applications of ASSLB. This can ensure the safety use of a battery even in severe situations such as overcharge, short circuit or thermal abuse⁹⁸. Particularly, aside from the interface between SSE and electrodes, the chemical and thermal stabilities of the composite materials are also required to be seriously considered before the design of CSSEs.

(5) Preferable mechanical strength and flexibility

Good mechanical strength and flexibility of solid electrolyte is very important for large-scale manufacture further practical application of lithium batteries. The typical advantage of CSSEs used in ASSLB is combining some preferable properties of consisted components. A case in point is the preferable mechanical strength and flexibility of ceramic/polymer CSSEs, which can combine the good dimensional stability of ceramics and the elasticity of polymers as well. In the case of polymer electrolytes and CSSE containing polymer electrolytes, much research has been and is dedicated

towards lowering the temperature required to achieve desirable ionic conductivity at ambient temperature by plasticizing the polymer phase. However, this sometimes come at the cost of its mechanical strength, especially with organic plasticizers.

2.5. Basic single polymer or inorganic phase in CSSE

2.5.1 Solid polymer electrolyte

Solid polymer electrolytes (SPE) refer to lithium salts dissolved in solid polymer materials which have inherent abilities to conduct ions. One of the most promising material is poly(ethylene oxide) (PEO), which was the first polymer host to be introduced as an SPE with alkali metal salt⁵⁰. The ether oxygen in the repeating ethylene oxide (EO) groups has a high donor number for Li⁺ which is crucial for solvation of lithium salt. Coupled with the mobility of polymer chains and high dielectric constant, PEO is one of the most widely studied polymer host for SPE¹¹⁴. SPE have the advantage of not hosting any liquids therefore mitigating the risk of electrolyte leakage. However, the main drawback of SPE is its low conductivity, typically from 10^{-8} to 10^{-6} S cm⁻¹ at ambient temperature depending on the molecular weight of PEO and lithium salt¹¹⁵.

There exists a jump in ionic conductivity for PEO as temperature increases past its melting point (T_m). The traditional interpretation of this phenomenon assumes the crystalline phase of PEO to have lower conductivity than its amorphous counterpart due to its rigid nature. As the crystalline phase decreases with increasing temperature, the improved segmental movement of the PEO chains allow Li⁺ to diffuse easier, resulting in a jump in conductivity. However, Stoeva et al¹⁰⁴ demonstrated for PEO-LiXF₆ (X = P, As, Sb) the crystalline phase shows much higher conductivity than that of amorphous phase at low temperatures. Nevertheless, the SPE crystalline phase only exhibited 6.3×10^{-8} S cm⁻¹ at 28°C.

Efforts to plasticize PEO through solid fillers still proved to improve ionic conductivity. Most notably, inactive ceramic fillers such as Al₂O₃, TiO₂, LiAlO₂, and SiO₂ which do not conduct ions independently have shown capabilities to improve the ionic conductivity of PEO SPE at ambient temperatures as well as above T_m , suggesting the fillers play more roles than simply suppressing the recrystallization of PEO^{116–128}. Research has demonstrated the Lewis acidic groups on the surface of the ceramic fillers can promote ion pair dissociation, weakening bonds between Li⁺ and the salt anions, and the EO groups on the PEO backbone, further increasing ionic conduction even above the melting point where no crystalline PEO phase remains^{129,130}.

Normally, solid type fillers in SPE have the ability to disrupt recrystallization of PEO as well promote Li⁺ dissociation to increase ionic conductivity and provide improvements to thermal and mechanical properties. However, as the improvement in ionic conductivity depend on surface interactions between the fillers and PEO, the benefits are limited by the maximum filler loading, after which the ionic conductivity drops due to filler agglomeration and tortuous Li⁺ pathway. Further modifications to nanofillers such as surface functional groups or grafting onto PEO chains may provide satisfactory ionic conductivity. More cases of this type of CSSE with inorganic fillers in polymer matrix will be introduced in Chapter 3.

2.5.2. Inorganic solid electrolyte

Inorganic solid electrolytes, often referred to as “ceramic electrolytes” encompass crystalline, partial crystalline (glass-ceramics), and amorphous glasses which have the ability to conduct Li^+ . Inorganic solid electrolytes are known to have high thermal stability and ionic conductivity amongst solid electrolytes. Inorganic solid electrolytes have the distinctive feature of being single-ion conductors, where lithium ions lithium transference number is near unity except halides. Compared to liquid electrolytes where dissolved ions move in a solvent, ceramic electrolytes conduct ions through vacancies or interstitial sites which involves periodic bottlenecks in energy. Most inorganic solid electrolytes can generally be divided into oxides and sulfides. Lesser studied inorganic solid electrolytes such as Li-hydrides (LiBH_4 , Li_3AlH_6 , $\text{Li}_2\text{BH}_4\text{NH}_2$, etc)^{131–135}, and Li-halides ($\text{Li}_{1.8}\text{N}_{0.4}\text{Cl}_{0.6}$, Li_2CdCl_4 , Li_3YCl_6 , $\text{Li}_3\text{InBr}_3\text{Cl}_3$, etc)^{136–138} are currently viewed as inferior due to disadvantages such as instability against cathode materials or low ionic conductivity.

A crucial property of inorganic solid electrolyte is its electrochemical stability. Unstable electrolytes can lead to decomposition of electrolyte, dendrite penetration, and overall low cyclability of the cell. Most inorganic solid electrolytes despite showing wide electrochemical stability window of 0–5 V, are not truly thermodynamically stable³. Decomposition of the electrolyte at the electrolyte-electrode interface forms a passivating layer known as the solid-electrolyte-interface (SEI) layer which has a higher stability thus extending the electrochemical stability window. The SEI layer is often the cause of cell aging due to its higher ionic resistivity and uneven formation. The exact mechanisms are widely unknown and is an intensely researched topic.

(1) Oxide Solid Electrolyte

The most well-rounded type of inorganic solid electrolyte may be the oxide solid electrolytes. With its higher stability against ambient air and high temperature, manufacturing such material is viewed to be most realistic in scaling up for industrial applications. Oxide solid electrolytes can be mainly separated into perovskite, NASICON-type, LISICON-type, garnet, and LiPON groups with corresponding structure as listed in Table 2. **Error! Reference source not found.** showing their respective total ionic conductivity and activation energy.

(1.1) Perovskite. One of the most well-researched perovskite type (ABO_3) solid electrolyte is the $\text{Li}_{3x}\text{La}_{2/3-x}\text{TiO}_3$ (LLTO). This is largely due to its high room temperature bulk ionic conductivity of $1 \times 10^{-3} \text{ S cm}^{-1}$ with $x = 0.1$ ¹³⁹. The conduction mechanism depends on the A-site vacancy and thus the value of x plays a large role in ionic conductivity¹⁴⁰. However, the high grain boundary resistance which can up be to two orders of magnitude higher than bulk resistance, remains a major bottleneck for achieving high total ionic conductivity. Studies on sintering conditions and elemental doping has yielded some favorable results, increasing the total ionic conductivity up to $3.17 \times 10^{-4} \text{ S cm}^{-1}$ at 25°C ¹⁴¹. Furthermore, due to LLTO's instability against lithium metal or intercalated electrodes with cathodic potential above 2.8V, the Ti^{4+} can be reduced to Ti^{3+} which grants the electrolyte electronic conductivity, leading to decomposition of the electrolyte and short-circuiting of the cell¹⁴².

(1.2) NASICON-type. NASICON was originally named as sodium super ionic conductor, with the general structure of $\text{AM}_2(\text{BO}_4)_3$ first coined by Goodenough and Hong et. al. for their work on $\text{Na}_{1+x}\text{Zr}_2\text{P}_{3-x}\text{Si}_x\text{O}_{12}$ in 1976¹⁴³. Lithium-containing

NASICON-type electrolytes can be obtained by substituting Na^+ with Li^+ in the A-site and utilized as high ion conducting lithium solid electrolytes. Such electrolyte gained traction when the $\text{Li}_{1+x}\text{M}_x\text{Ti}_{2-x}(\text{PO}_4)_3$ system was discovered to exhibit high ionic conductivity, with Al^{3+} substitution for M at $x = 0.3$ (LATP), yielding total ionic conductivity of $7 \times 10^{-4} \text{ S cm}^{-1}$ at 25°C ¹⁴⁴. However, LATP suffers from the same Ti^{4+} reduction issue as LLTO and requires a lithium protective layer to be utilized practically as an electrolyte. A more recent NASICON-type electrolyte was found to exhibit room temperature ionic conductivities between 7.5×10^{-5} and $5 \times 10^{-4} \text{ S cm}^{-1}$ ^{145–147}. Though reduction of Ge^{4+} to Ge^{3+} can still occur against lithium metal, LAGP exhibits a more stable interface than LATP with electrochemical stability up to 6 V versus Li/Li^+ ^{145,148}.

(1.3) LISICON-type. LISICON (Lithium super ionic conductor)-type structure include Li_4SiO_4 and $\gamma\text{-Li}_3\text{PO}_4$ with XO_4 -based ($\text{X} = \text{Al}, \text{S}, \text{Si}, \text{Ge}, \text{Ti}, \text{or P}$) tetrahedral units, and Li-O polyhedrals. The first LISICON-type electrolyte was discovered by Hong et. al. with the general structure of $\text{Li}_{16-2x}\text{D}_x(\text{TO}_4)_4$, where $\text{D} = \text{Mg}^{2+}$ or Zn^{2+} , and $\text{T} = \text{Si}^{4+}$ or Ge^{4+} . Ionic conductivity of $1.3 \times 10^{-1} \text{ S cm}^{-1}$ was achieved at 300°C with the $\text{Li}_{14}\text{Zn}(\text{GeO}_4)_4$ composition¹⁴⁹. LISICON-type electrolytes generally exhibit ionic conductivity of roughly $10^{-5} \text{ S cm}^{-1}$ at room temperature which is amongst the lower range of oxide solid electrolytes. LISICON-type electrolytes show high stability even in moist air, allowing for ease of manufacturing and handling. However, stability against lithium metal is relatively poor.

(1.4) Garnet. Ideal Garnets have a general formula of $\text{A}_3\text{B}_2(\text{CO}_4)_3$ with cubic phase ($\text{Ia}\bar{3}\text{d}$ space group), where A is Ca, La, Mg, Y, or rare earth elements; B is Al, Fe, Ga, Ge, Mn, Ni, or V; C is Al, As, Fe, Ge, or Si^{150,151}. The first discovery of garnet-type lithium electrolyte is $\text{Li}_5\text{La}_3\text{M}_2\text{O}_{12}$ ($\text{M} = \text{Nb}, \text{Ta}$) by Thangadurai, where $\text{Li}_5\text{La}_3\text{Ta}_2\text{O}_{12}$ achieved total ionic conductivity of $3.4 \times 10^{-6} \text{ S cm}^{-1}$ at 25°C ¹⁵². Garnet-type solid electrolytes show exceptional stability against lithium metal anodes, with electrochemical stability $\geq 6 \text{ V}$ vs Li^+/Li at room temperature¹⁵³. Notably, $\text{Li}_7\text{La}_3\text{Zr}_2\text{O}_{12}$ (LLZO) have been shown to stable against molten lithium metal and exhibits ionic conductivity of $3 \times 10^{-4} \text{ S cm}^{-1}$ at 25°C ¹⁵⁴. Due to the high stability and promising ionic conductivity of $\text{Li}_7\text{La}_3\text{Zr}_2\text{O}_{12}$, much work has been done in elemental doping to further improve the performance of LLZO in terms of improving ionic conductivity, and lowering sintering temperature and activation energy.¹⁵⁵

(1.5) LiPON. Lithium phosphorous oxide nitride (LiPON) is an amorphous phase solid electrolyte. The first LiPON electrolyte was fabricated through d.c. magnetron sputtering with a Li_3PO_4 target in N_2 gas, which yielded $\text{Li}_{2.9}\text{PO}_{3.3}\text{N}_{0.46}$ with $3.3 \times 10^{-6} \text{ S cm}^{-1}$ at 25°C . Due to its high stability against lithium metal up to 5.5 V, it has been a popular solid electrolyte^{156–158}. However, limited by its low conductivity, it has often been utilized as a lithium protective layer due to sputtering techniques being able to control the thickness to under $1 \mu\text{m}$ ¹⁵⁹.

(2) Sulfide Solid Electrolyte

Sulfide solid electrolytes generally show higher ionic conductivity as presented in Fig. 4, where $\text{Li}_{10}\text{GeP}_2\text{S}_{12}$ is able to compete with liquid electrolyte with above $10^{-2} \text{ S cm}^{-1}$ conductivity at room temperature. The improvement over oxide electrolyte is attributed to the lower electronegativity of S compared to O. Li^+ less

limited. However, the new pathway, or even expressway for Li-ion conduction at inorganic/polymer interfacial region are also exist according to some very recent reports^{22,109}, which can be regarded as a series and parallel network consisting of inorganics and polymer ionic conductive domains. Therefore, in theory, the effectively continuous lithium ionic pathway can be formed in each phase and the interfacial region between the two phases of CSSEs by controlling their geometrical characteristic properly¹⁷². In this regard, the geometrical characteristic, namely, the advanced structures of inorganic/polymer CSSEs have been proposed by several researchers and summarized in this section.

To be specific, the typical advanced structures of CSSEs used in lithium batteries are summarized and divided into four categories as mentioned above, including the (1) inorganic fillers in polymer matrix, (2) heterogeneous layered structures, (3) 3D inorganic continuous framework with filled polymer, and (4) open-framework related composite electrolytes. Moreover, each of these categories are further described according to the key material composition, performance enhancement mechanism, and even construction method. More details can be seen in the following four sections.

3.1 Inorganic fillers in polymer matrix

So called nanoparticles can be inactive fillers (e.g. SiO₂, TiO₂, ZrO₂ and Al₂O₃) or active fillers (e.g. Li₃N, LiAl₂O₃, lithium garnets, LISICON-like particles, perovskites, etc.) in polymer matrix as 0 dimensional CSSEs in this paper, in which the fillers are divided into those two main categories according to their lithium ionic conductivities. By comparing, the active nanofillers have much better ionic conductivities ($> 10^{-3}$ S cm⁻¹) and higher lithium transference numbers (> 0.5), but the downsides of them are complex synthesis process, difficult-to-tune surface interaction against the polymer matrix, and sensitivity of the particles towards moisture and carbon dioxide^{173,174}. The inactive nanofillers are tunable, easily preparation, and inexpensive, but their resulting CSSE ionic conductivities are much lower ($< 10^{-4}$ S cm⁻¹) and interfacial contact with electrodes are also poorer¹⁷⁵. More details for 0D CSSEs with those nanofillers in polymer matrix are introduced as follows.

3.1.1 Inactive/passive nanofillers

3.1.1.1 0D nanofillers (nanoparticles)

Dispersing inactive inorganic nanofillers (or nanoparticles, NP) into polymer matrix with lithium salt is an effective strategy to improve the electrical properties (e.g. ionic conductivities), mechanical properties, and even interfacial stability of single polymer phase¹⁷⁶⁻¹⁷⁸. This type of structure is the most widely investigated in CSSEs of lithium batteries. The inactive nanofillers in polymer based CSSEs is separated into two main categories, (1) metal oxide fillers including inert oxide ceramics (Al₂O₃, TiO₂, SiO₂, ZrO₂, etc.), treated SiO₂, rare-earth oxide ceramics, and ferroelectric materials; and (2) non-metal oxide fillers including nano carbon materials, molecular sieves and zeolites, and so on. Regarding active fillers, most ceramic electrolytes introduced previously can be incorporated into CSSE, mainly including Perovskite, NASICON, Garnet types, and some others.

(1) Metal oxide fillers

The typical CSSE system with inactive metal oxide fillers are summarized in Table 3. As conventional compounds, oxide ceramics such as Al₂O₃¹⁷⁹, TiO₂^{117,179}, ZrO₂^{180,181} and ZnO¹⁸² maybe the most widely investigated inorganic fillers. Al₂O₃ with particle size of 300mesh was first proposed as a filler in CSSEs leading to improved mechanical strength of PEO based CSSEs, but at the same time, the conductivity of CSSE stayed almost the same¹⁸³. However, after that, F. Croce *et al.*, reported that the addition of nanometer-sized ceramic powders including Al₂O₃ and TiO₂ can also improve the conductivity and ion transference number. It is believed that the nano Al₂O₃ and TiO₂ particles can perform as a solid plasticizers and kinetically inhibited the crystallization of PEO matrix through Lewis acid–base interactions between ceramic filler and both polymer segment and lithium salt anion¹⁷⁷. Since it is the interphase between inactive ceramic filler and polymer matrix that facilitates the conduction of lithium ion, particle size and surface area of fillers play a very important role in the improving of conductivity.

Moreover, the content and concentration of the NPs are considered as another critical factors for affecting the ionic conductivity of CSSEs^{180,184}. In this regard, J. Adebahr *et al.* investigated the different contents of nano-sized ceramic particles in polymer based CSSEs, which can influence the polymer morphology and the ionic transport. The ⁷Li NMR results in their research showed that when the amount of NP fillers is lower than the critical point, addition of NP fillers can lead to the filler–lithium ion interaction and further change the lithium ion environment. But when the amount of NP fillers is higher than the critical point, aggregation of filler particles will occur and decrease the conductivity of CSSEs. On the other hand, ¹H NMR results indicated that the fillers can also break up the chemical crosslinks between the polymer chains, thus further increasing their segmental mobility of the chains.

H. Xiong *et al.* treated the ZnO nanoparticles with low molecular weight poly-(ethylene glycol) methyl ether(PEGME) and acetate group(Ac) respectively. Then, the treated ZnO nanoparticles are used as filler in PEO matrix. The PEFME treated ZnO nanoparticles can be homogeneously dispersed in PEO matrix, resulting in a higher conductivity but Ac treated ZnO nanoparticles aggregated heavily leading to a low lithium ion conductivity¹⁸². The in situ synthesis of monodispersed SiO₂ nanospheres in PEO as shown in Fig. 5 (a), Tetraethyl orthosilicate is added in. Strong chemical/mechanical interactions could be formed between the monodispersed SiO₂ spheres and polymer chains, thus avoiding agglomeration of the fillers and further decreasing the high degree of polymer crystallinity¹⁸⁵.

Additionally, surface chemistry of the fillers is also a factor to influence the performance of CSSE. Surface chemistry can influence two aspects: the ability to interact with its surroundings, and the aggregation behavior of filler particles. In F. Croce *et al.*'s work¹⁷⁷, the CSSEs with TiO₂ filler has larger ionic transference number compared with that with Al₂O₃ filler. This phenomenon is attributed to the more acidic surface of TiO₂. A. D'Epifanio *et al.* found that compared with Al₂O₃ filler which is almost covered by -OH functional group on surface, ZrO₂ filler can lead to a thinner passivation layer against lithium metal anode.

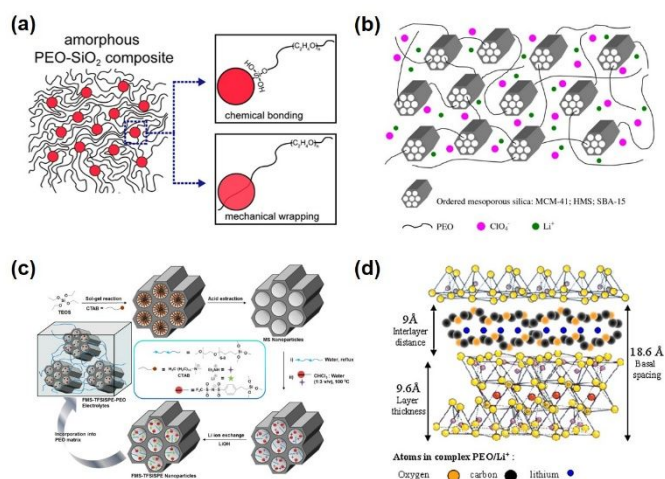


Fig. 5 Schematic figures of (a) the structure of amorphous PEO-SiO₂ composite;¹⁸⁵ Reprinted with permission from ref. 185. Copyright 2016, American Chemical Society. (b) PEO/LiClO₄ based composite solid state electrolyte with ordered mesoporous silica as filler;¹⁸⁶ Reprinted with permission from ref. 186. Copyright 2016, Royal Society of Chemistry. (c) process to prepare a functionalized mesoporous silica (FMS-TFSISPE) nanoparticles with anion and oligo-PEG moieties in the pore wall;¹⁸⁷ Reprinted with permission from ref. 187. Copyright 2017, American Chemical Society. (d) the structure of the nanocomposites PEO@bentonite-Li⁺.¹⁸⁸ Reprinted with permission from ref. 188. Copyright 2011, Elsevier Ltd.

While choosing different materials is one method to change the surface chemistry of the filler, another effective way to change filler's the surface chemistry is surface modification. Proper surface modification can further improve the polarity of filler surface and dispersion of fillers in polymer matrix. For instance, Y. Matsuo *et al.*,¹⁸⁹ found that silica (SiO₂), a well-known material with surface hydroxyl groups, was able to improve the ionic conductivity of PEG/LiCF₃SO₃, but the system with surface treated SiO₂ showed much better improvement than that containing untreated ones, similar results are also reported in PEO/LiClO₄/SiO₂¹⁹⁰ or PEO/LiBF₄/SiO₂ systems¹⁹¹. In addition to the conductivity, the surface-functionalized SiO₂ was also proven to improve the interfacial stability between the CSSE and lithium metal anode, as well as the their mechanical properties by forming chain entanglements^{191,192}.

Aside from the inert oxide ceramics mentioned above, some other inactive metal oxides are also investigated as fillers used in polymer based CSSEs, such as ferroelectric materials (e.g. SrBi₄Ti₄O₁₅,^{193,194} BaTiO₃,¹⁹⁵⁻¹⁹⁸ PbTiO₃,^{199,200} and LiNbO₃)¹⁹⁹ which can increase the polarity of the polymer chains and further improve the charge separation and ionic conductivity. Solid super acids (e.g. SO₄²⁻/ZrO₂)²⁰¹⁻²⁰⁴ can reduce the recrystallization of polymer chains and act as nucleus of polymer spherulites to increase their amount, due to the solid super acids possessing strong acidic centers to interact with the oxygen atoms¹⁷⁹. Some of those typical systems are illustrated in Table 3.

Table 3 Typical inactive metal oxides as fillers in polymer based CSSEs

	Fillers (NP)	Polymer/ Lithium salt	σ (S cm ⁻¹)	Enhancement (vs. filler-free, S cm ⁻¹)	Ref.
Inert oxide ceramics	TiO ₂	PEO ₈ /LiClO ₄	10 ⁻⁵ – 10 ⁻³ at 30-80°C	10 times, 10 ⁻⁴ and 10 ⁻⁸	179
	10 wt% TiO ₂	PEO/LiClO ₄	2 × 10 ⁻⁴ at 60°C	10-20 times	117
	Al ₂ O ₃	PEO ₈ /LiClO ₄	10 ⁻³ – 10 ⁻⁵ at 80-30°C	10 times, 10 ⁻⁴ and 10 ⁻⁸	179
	Al ₂ O ₃	PEO ₈ /LiCF ₃ SO ₃	10 ⁻⁶ at 30°C	2-5 times	179
	10 wt% Al ₂ O ₃	PEO/LiClO ₄	10 ⁻⁵ at 60°C	2-10 times	117
	2.5 wt% ZrO ₂	PVDF/PVC/LiBOB	4.38 × 10 ⁻⁴ at 20°C	5 times, 8.3 × 10 ⁻⁵ at 20°C	184
	ZnO	PEO/LiTFSI	5 × 10 ⁻⁵ at 20°C	250 times, 2 × 10 ⁻⁷ at 20°C	182
Treated SiO₂	Monodispersed SiO ₂	PEO/LiClO ₄	1.2 × 10 ⁻³ at 60°C, 4.4 × 10 ⁻⁵ at 30°C	20-1000 times, 4.5 × 10 ⁻⁵ at 60°C, 5 × 10 ⁻⁸ at 30°C	185
	SiO ₂	PEG/LiCF ₃ SO ₃	4.8 × 10 ⁻⁵ at 40°C	--	189
Ferroelectric materials	12.5 wt% SrBi ₄ Ti ₄ O ₁₅	PEG/LiClO ₄	2.4 × 10 ⁻⁶ at RT	100 times, 2.3 × 10 ⁻⁸ at RT	193
	12.5 wt% SrBi ₄ Ti ₄ O ₁₅	PEO/LiN(CF ₃ SO ₂) ₂	6.4 × 10 ⁻⁷ at RT	25-30 times, 2.4 × 10 ⁻⁸ at RT	194
	5 wt.% BaTiO ₃	PEO/LiTFSI	1.8 × 10 ⁻⁵ at 25°C	3-4 times, 5.3 × 10 ⁻⁶ at 25°C	195
	7.5 wt.% BaTiO ₃	P(VDF-HFP)/PVAc/E C/LiTFSI	2.3 × 10 ⁻³ at 30°C	2-3 times, 1 × 10 ⁻³ at 30°C	196
	15 wt.% BaTiO ₃	PEO/PVDF/PC/LiClO ₄	1.2 × 10 ⁻⁴ at RT	2 times, 6.8 × 10 ⁻⁵ at RT	197
Solid super acid	7 wt.% SO ₄ ²⁻ /ZrO ₂	PEO ₁₂ /LiClO ₄	2.1 × 10 ⁻⁵ at RT	140 times, 1.5 × 10 ⁻⁷ at RT	201
	5 wt.% SO ₄ ²⁻ /ZrO ₂	PEO ₂₀ /LiClO ₄	2.5 × 10 ⁻⁴ at 60°C	10-15 times, 2.1 × 10 ⁻⁵ at 60°C	204

* NP, Nanoparticle; PEO, poly(ethylene oxide); PEG, poly(ethylene glycol); PVA, poly(vinyl alcohol); PMMA, poly(methyl methacrylate); PVDF, poly(vinylidene fluoride); PVC, poly(vinylchloride); LiBOB, lithium bis(oxalato)borate; Ref., references; σ , conductivity; LiTFSI, LiN(CF₃SO₂)₂, lithium bis(trifluoromethanesulfonyl)imide; P(VDF-HFP)/PVAc, poly(vinylidene fluoride-hexafluoro propylene)/poly(vinyl acetate); EC, ethylene carbonate; PC, propylene carbonate;

(2) Non-metal oxide

Non metal oxide fillers are summarized and listed in Table 4. One typical type of non-metal oxide fillers is the nano carbon materials, carbon is usually used as the important anode material but much less use as the electrolyte materials in lithium batteries, which may due to owing to its electrical conductivity. However, some

researchers still believe that the addition of appropriate amount of electrical conductivity materials, carbon materials typically, can also improve the performance of the polymer based CSSEs^{205,206}. G.B. Appetecchi *et al.*²⁰⁶ added a small volume fraction (< 1.5%) of carbon particles with moderate high surface area (about 60 m²·g⁻¹) in PEO/LiCF₃SO₃ system, which showed excellent ionic conductivity

and interfacial stability. Aside from carbon particle, the fullerene (C₆₀) also used as fillers in hyperbranched star polymer HBPS-(PMMA-b-PPEGMA)₃₀ with hyperbranched polystyrene as the core and polymethyl methacrylate-block-poly(ethylene glycol) methyl ether methacrylate, which exhibit a wide electrochemical window of 5.2 V, good interfacial stability, and compatibility²⁰⁵. However, the mechanism of conductivity enhancement in carbon/polymer CSSEs is still unclear and need to be further investigated.

Another type of non-metal oxide fillers is molecular sieves and zeolites/nanoporous materials. Molecular sieve, a material with pores (very small holes) of uniform size, has been widely investigated in many areas^{207–210}, can be divided into microporous material (<2 nm), mesoporous material (2–50 nm), and macro porous material (>50 nm) according to the pore size. Compared with traditional nanofillers mentioned above, some molecular sieves possess much stronger Lewis acid centers in their frameworks and inside the channels, which might be much more effective in decreasing the crystallization tendency of the polymer chains^{211–213}. Some representative molecular sieves in polymer/lithium salt based CSSEs are listed in Table 4.

One typical class of microporous material (<2 nm) in molecular sieves is zeolite^{214,215} such as ZSM-5, a widely studied material in catalysis field due to its exceptionally high surface area, special channel structure, and strong Lewis acidity¹⁸⁶. When it comes to CSSEs, the ZSM-5 could also be used as fillers to significantly improve their ionic conductivity, lithium ion transference numbers, and also electrochemical stability²¹². Jingyu Xi *et al.*²¹² carried out polarized optical microscopy (POM) technique to investigate the mechanisms of the performance enhancement after filling with ZSM-5. It indicated that the ZSM-5 particles could also act as the nucleus of polymer spherulites to increase their amount in the nucleation stage, and decrease the recrystallization tendency of PEO chains through Lewis acid–base interactions in the growth stage. Therefore, much more amorphous phases of PEO could be created to accelerate lithium ions transport.

Regarding mesoporous material (2–50 nm) in molecular sieves, MCM-41 (Mobil Composition of Matter no. 41), HMS (Hexagonal Mesoporous Silica), and SBA-15 (Santa Barbara number 15) with ordered mesoporous channels are found to be good fillers in PEO/LiClO₄ based CSSEs^{213,216}. It is interesting that the polymer chains could intercalate into the channels of those mesoporous materials via some preparation methods such as solvent casting. As shown in Fig. 5(b), in comparison to traditional nonporous fillers, this kind of molecular sieves possess strong Lewis acid centers in their both internal and external surfaces, which can be regarded as physical cross-linking centers for polymer chains. Those Lewis acid sites can interact with the Lewis basic ether O of polymer, thus further suppressing the reorganization of polymer chains and increase their amorphous phases¹⁸⁶. Moreover, the T_g and T_m, and the tensile modulus of polymers will change after adding the inclusion of the mesoporous materials.

To further enhance the performance of CSSEs, the mesoporous materials can be modified to be functionalized nanofillers, such as surface tailored porous silica²¹⁷, functionalized mesoporous silica SBA-15^{187,218}, or MCM-41²¹⁹. For instance, as shown in Fig. 5(c), Youngdo Kim *et al.*¹⁸⁷ produced functionalized mesoporous silica (FMS) nanoparticles and use them as fillers into the PEO polymer matrix, in which the anionic weak-binding imide group, a dense brush

of oligo-poly(ethylene glycol) (oligo-PEG) moieties, and solvating Li⁺ are incorporated to functionalize the mesoporous silica via a two-step selective functionalization method. The obtained novel polymer–mesoporous silica nanohybrid solid electrolyte with the sole mobile Li ions showed very excellent mechanical and electrochemical performances (ionic conductivity is roughly 1×10^{-3} at 25°C), which is due to the continuous weak-binding and solvating nanopore channel of the mesoporous silica. Additionally, ionic liquid can also be used to decorate the mesoporous silica nanoparticles or some other fillers, thus achieving significantly attractive ionic conductivity^{220–223}, although strictly speaking, the electrolyte containing ionic liquid is not regarded as all-solid-state electrolyte for lithium battery.

Some other fillers such as clay, a finely-grained natural rock or soil material that combines clay minerals with possible traces of quartz, metal oxides and organic matter, can also be added into polymer matrix as filler to improve the electrochemical performance. One of the most widely investigated fillers in CSSEs is the montmorillonite (MMT)^{188,224–233}, a layered clay with good cationic exchange capability and the ability to participate in the processes of intercalation and swelling, can facilitate its own dispersion in polymer matrix as shown in Fig. 5(d)¹⁸⁸. Moreover, the intercalated structure of clay can construct some channels in nano-scale for the transport of cations (e.g. Li⁺) and decrease the crystallization of the polymer¹⁸⁶. Until now, most of the researchers have focused on the ionic conduction mechanism and the influence factors for electrical or electrochemical properties enhancement^{188,224,226–229}.

Aside from the direct addition, some modified nanoclays are also investigated to further improve the ionic conductivity of polymer based CSSEs^{225,227,228,230,231,234}. For instance, Tapabrata Dam *et al.*²²⁷, synthesized the dodecylamine modified MMT (DMMT) using solution casting method. The MMT is modified with dodecyl amine, thus changing the silicate layer from hydrophilic to hydrophobic and increasing their interlayer spacing. This can facilitate the intercalation of polymer-salt complex into the clay layers to further disturb the strength of the polymer-cation coordination bond, therefore further enhancing the mobility of the cations (e.g. Li⁺). Moreover, Ming Xie *et al.*²³¹ performed the organophilic modification for nano MMT (OMMT) to form a PVC/PVDF/LiTFSI/nano-OMMT solid polymer electrolyte for ASSLIB, in which the MMT was modified by cetyl trimethyl ammonium bromide [C₁₆H₃₃N(CH₃)₃]⁺Br[−] to acquire hydrophobic properties. The ionic conductivity of the obtained SSE reaches up to 1.67×10^{-4} S·cm^{−1} at room temperature, and good stability and reversibility were also achieved in the corresponding solid state battery.

Furthermore, sodium cations in MMT could also be exchanged into Lithium ions for a usage as Li ion sources to change the inactive nanofiller into active^{188,235–237}. Seok Kim *et al.*²³⁵ prepared Li-MMT by cation-exchange reaction and added them as fillers into PEO polymer matrix, demonstrating that the layered-structure Li-MMT can not only decrease the crystallinity and melting temperature of PEO based composite electrolyte, but also act as an anionic species to improve Li ions transport. Other than that, very recently, lithium montmorillonite was also introduced into solid state lithium ion batteries by L. Chen *et al.*²³⁶, the presented SSE was fabricated with pure Li-MMT, poly(ethylene carbonate) (PEC) polymer, lithium bis(fluorosulfonyl)imide (LiFSI), tiny fluoroethylene carbonate (FEC) additive, and poly(tetrafluoroethylene) (PTFE). It exhibited very high

ionic conductivity of $3.5 \times 10^{-4} \text{ S cm}^{-1}$, a wide electrochemical window of 4.6 V (vs Li^+/Li), and even a very high ionic transference number of 0.85 at 25°C. However, this type of so-called SSE is still

controversial because the liquid organic solvent is added into the polymer matrix with lithium salt, which can be regarded as the addition of liquid electrolyte.

Table 4 Typical inactive non-metal oxides as fillers in polymer based CSSEs

	Fillers (NP)	Polymer/ Lithium salt	σ (S cm^{-1})	Enhancement (VS. filler-free, S cm^{-1})	Ref.
Carbon	2.2 wt.% Carbon particles (40 nm)	PEO/LiCF ₃ SO ₃	2.9×10^{-6} at 20°C	3-5 times	206
	Fullerene (C60)	HBPS-(PMMA-b-PPEGMA) ₃₀ /LiTFSI	5.18×10^{-6} at 30°C, 8.22×10^{-5} at 60°C	--	205
	0.2 wt.% Carbon nanotube (CNT)	HBPS-(PMMA-b-PPEGMA) ₃₀ /LiTFSI	1.06×10^{-5} at 30°C, 1.73×10^{-4} at 60°C	--	205
Molecular sieves	10 wt.% ZSM-5	PEO ₁₀ /LiClO ₄	1.4×10^{-5} (25°C)	90-100 times, 1.5×10^{-7} (25°C)	212
	10 wt.% MCM-41	PEO ₁₂ /LiClO ₄	1.3×10^{-5} (25°C)	75-80 times	213
	5 wt.% m-MCM-41	PEO/LiClO ₄	4.4×10^{-5} (40°C)	6-8 times, 6.6×10^{-6} (40°C)	219
	10 wt.% HMS	PEO ₁₂ /LiClO ₄	1.5×10^{-5} (25°C)	80-90 times	213
	10 wt.% SBA-15	PEO ₁₂ /LiClO ₄	1.9×10^{-5} (25°C)	110-120 times	213
	1 wt.% Tailored porous silica (epoxy-SiO ₂)	PEO/CF ₃ SO ₃ Li	1.03×10^{-4} (25°C)	--	217
	1 wt.% Tailored porous silica (chem-SiO ₂)	PEO/CF ₃ SO ₃ Li	4.2×10^{-4} (25°C)	--	217
	FMS (functionalized mesoporous silica)	PEO/TFSISPE	1×10^{-3} (25°C)	100 times	187
	7.5 wt.% mesoporous Ti	P(EO/EM2)/LiClO ₄	1.4×10^{-5} (30°C)	>2 times	238
	5 wt.% mesoporous Al	P(EO/EM2)/LiClO ₄	8.9×10^{-6} (30°C)	2 times	238
Clay	5 wt.% MMT	PMMA/PEG/LiClO ₄	3.17×10^{-7} (29°C)	1.6×10^{-8} (29°C)	229
	5 wt.% MMT	PMMA/LiCF ₃ SO ₃	2.09×10^{-6} (30°C)	2.66×10^{-10} (30°C)	232
	5 wt.% MMT	PEO/PMMA/LiBF ₄	1.65×10^{-5} (27°C)	10 times	233
	10 wt.% MMT	PEO/LiTFSI	2.75×10^{-5} (25°C)	5.5 times, 5.0×10^{-6} (25°C)	224
	1 wt.% DMMT	PEO ₈ /LiClO ₄	9.16×10^{-5} (30°C)	208 times 4.44×10^{-7} (30°C)	228
	2 wt.% DMMT	PEO ₂₀ /LiAsF ₆	4.0×10^{-5} (RT)	40 times, 1.0×10^{-6} (RT)	227
	4 wt.% OMMT	PVDF/PVA/LiTFSI	4.31×10^{-4} (RT)	2.35×10^{-6} (RT)	230
	0.5 wt.% LCI-MMT	PEO/PLA/LiClO ₄	1.05×10^{-5} (20°C)	6.36×10^{-6} (20°C)	225
	3 wt.% Bentonite-Li ⁺ (Li-MMT)	PEO	1.81×10^{-7} (25°C)	1.23×10^{-9} (25°C)	188
	20 wt.% Li-MMT	PEO/LiClO ₄ /EC	5.3×10^{-6} (25°C)	6.3×10^{-8} (25°C)	235

* wt% with respected to polymer host; PEO, poly(ethylene oxide); LiTFSI, LiN(CF₃SO₂)₂, lithium bis(trifluoromethanesulfonyl)imide; HBPS-(PMMA-b-PPEGMA)₃₀, with hyperbranched polystyrene as core and polymethyl methacrylate-block-poly(ethylene glycol) methyl ether methacrylate; MCM-41, Mobil Composition of Matter no. 41; HMS, Hexagonal Mesoporous Silica; SBA-15, Santa Barbara number 15; DGE, di(ethylene glycol) dimethyl ether; EMIMTFSI, 1-ethyl-3-tai-methylimidazolium bis(trifluoromethanesulfonyl)imide; FMS, functionalized mesoporous silica; TFSISPE, 2-[(Trifluoromethane sulfonylimido)-N-4-sulfonyl phenyl]ethyl; epoxy-SiO₂, epoxy coated porous silica nanostructures; chem-SiO₂, porous silica nanostructures by chemical leaching; P(EO/EM2), Pluronic P123 (EO₂₀PO₇₀EO₂₀, EO and PO denote ethylene oxide and propylene oxide units, average M_w = 5800; m-MCM-41, mesoporous silica MCM-41 with surface modification of (3-glycidioxypropyl)trimethoxysilane (GLYMO); PMMA, poly(methyl methacrylate); MMT, montmorillonite; DMMT, dodecylamine modified MMT; OMMT, Organophilic modification of nano-MMT; PVC, Polyvinyl chloride; PVDF, poly(vinylidene fluoride); LiMNT, lithium montmorillonite; LiFSI, lithium bis(fluorosulfonyl)imide; EC, ethylene carbonate (solid at room temperature); LCI, liquid crystal ionomer; PVA, polyvinyl alcohol;

3.1.1.2. 1D fillers

It is well accepted that the improvement of lithium ion conductivity by using metal oxide filler are mainly attributed to two aspects: (i) creating percolation pathway with high conductivity and (ii) suppressing the crystallization of polymer matrix. But still, due to the agglomeration of metal oxide particles and the non-ionically-conductive nature of metal oxide, further increase in the content of filler cannot further improve the lithium ion conductivity of solid polymer composites when a critical content is already achieved.

Under this circumstance, replacing the 0D metal oxides with 1D metal oxides (nanotube, nanobar and nanofiber) is a reasonable choice to further increase the lithium ion conductivity via a much more continuous percolation pathway provided by the longer dimension of 1D materials with less chance of agglomeration. Based on the distribution of filler in polymer matrix, the 1D CSSEs can be mainly divided into two categories: CSSEs with (1) random distributed fillers and (2) aligned fillers.

One of the common 1D inactive fillers is the TiO_2 , Song et al. synthesized TiO_2 nanorods by hydrothermal method and prepared CSSEs by mixing TiO_2 nanorod, LiTFSI, poly(propylene carbonate) together and blading the mixture on cellulose membrane²³⁹. The TiO_2 /PPC(LiTFSI) CSSEs show a high lithium ion conductivity of $1.52 \times 10^{-4} \text{ S cm}^{-1}$ at RT and wide potential window more than 4.6 V. As shown in Fig. 6 (a), they believe the improved ionic conductivity should be ascribed to the high contact area between TiO_2 nanorods which promote the lithium salts dissociation and the continuous lithium ion transport channels provided by TiO_2 nanorods/PPC interphase.

Wei and his co-workers prepared YSZ nanowire/PEO(LiClO₄) CSSEs²⁴⁰. It is pointed out that yttrium doping can create high concentration of oxygen vacancies in ZrO_2 and the positively charged oxygen vacancies can serve as Lewis acid which can facilitate the dissociation of lithium salts as presented in Fig. 6 (b). Compared with the pure PEO(LiClO₄) electrolyte ($3.62 \times 10^{-7} \text{ S cm}^{-1}$) and electrolyte

with YSZ nanoparticles ($2.98 \times 10^{-6} \text{ S cm}^{-1}$ at 30°C), the conductivity of electrolyte with YSZ nanowire is enhanced to $1.07 \times 10^{-5} \text{ S cm}^{-1}$ at 30 °C. This improvement of conductivity is mainly due to the oxygen vacancies introduced by Yttrium doping and the more continuous fast ion transport pathway formed by YSZ nanowire/PEO interaction.

The surface chemistry of filler is quite important, to further improve the dissociation effect of filler in CSSEs, different inorganic fillers have been tried to further increase the conductivity of CSSEs. Hydrogen titanate nanotube (HTNT) has been synthesized by Fernando et al. and used as filler for PAN based CSSE due to its special surface chemistry²⁴¹. By using molecular dynamic simulation, they find perchlorate ions tends to stabilize on the surface of HTNT. The reason is that HTNT has an acidic surface and the hydrogen atoms on the surface of HTNT can strongly interact with oxygen atoms of perchlorate atoms. Due to the dissociation effect of acidic surface of HTNT and the relative continuous diffusion pathway of lithium ion, the conductivity can achieve $\sim 4 \times 10^{-4} \text{ S cm}^{-1}$.

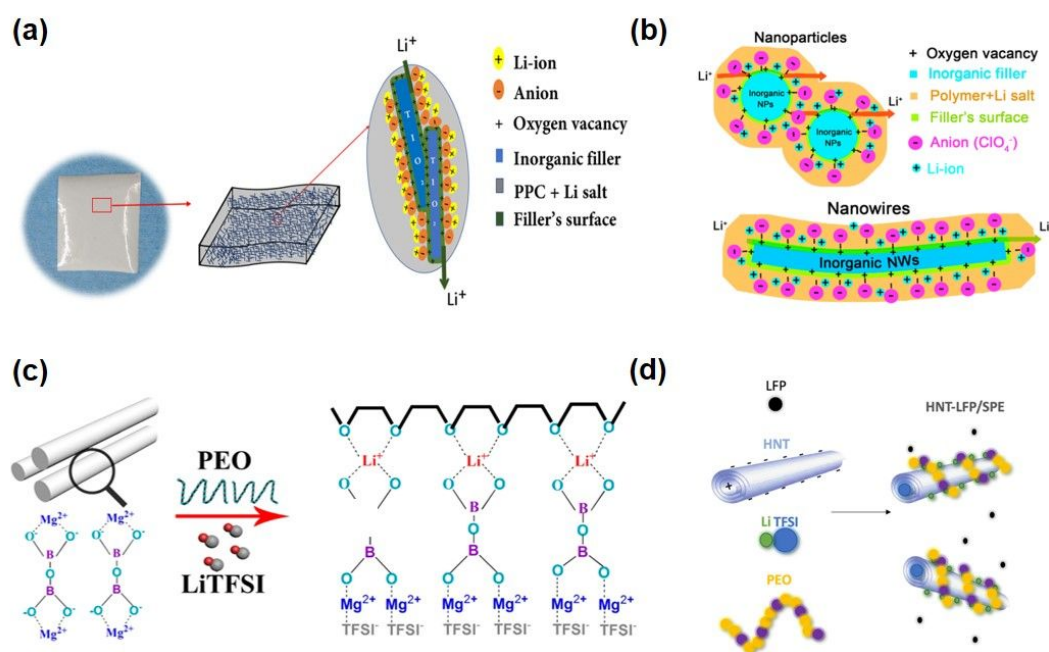


Fig. 6 CSSEs with 1D fillers in polymer matrix. (a) The surface structure of TiO_2 nanorods in polymer matrix²³⁹. Reprinted with permission from ref. 239. Copyright 2019, Wiley-VCH. (b) Lithium ion conduction in the CSSEs with YSZ nanoparticles and nanowire²⁴⁰. Reprinted with permission from ref. 240. Copyright 2016, American Chemical Society. (c-d) Polymer matrix and lithium interact with (c) $\text{Mg}_2\text{B}_2\text{O}_5$ ²⁴² nanowire, reprinted with permission from ref. 242. Copyright 2018, American Chemical Society. and (d) Halloysite nanotubes (HNTs)²⁴³, reprinted with permission from ref. 243. Copyright 2016, American Chemical Society.

O. Sheng and co-workers synthesized a multifunctional CSSEs with $\text{Mg}_2\text{B}_2\text{O}_5$ nanowire as filler²⁴². As shown in Fig. 6 (c), Mg^{2+} on the surface $\text{Mg}_2\text{B}_2\text{O}_5$ can interact with $-\text{SO}_2-$ group in the TFSI⁻ anion, by which more lithium ion is released and the lithium ion conductivity is improved to $1.53 \times 10^{-4} \text{ S cm}^{-1}$ at 40°C. Due the same reason, the ion transference number can be improved to 0.44. The interaction between $\text{Mg}_2\text{B}_2\text{O}_5$ and PEO can also improve the mechanical strength and flame resistance. The possible reason of improved flame resistance is that the presence of $\text{Mg}_2\text{B}_2\text{O}_5$ facilitate the formation and stabilization of carbon layer. This carbon layer can hinder the propagation of fire and heat, hence the fire resistance is improved.

Halloysite nanotubes have also been used as filler for PEO base CSSEs because of the unique structure, economical availability, and environmental amity^{243,244}. Halloysite nanotubes have siloxane external surface and internal alumina core. Therefore, the outer surface is overall negatively charged which is similar to SiO_2 . Zhu and co-workers prepared Halloysite nanotubes/PEO(LiTFSI) CSSEs as presented in Fig. 6(d)²⁴³. The conductivity of the electrolyte can achieve $9.23 \times 10^{-5} \text{ S cm}^{-1}$ at 25°C with improved electrochemical stability and mechanical properties. The conductivity improvement can be attributed to the effective lithium ion transport pathway which comes from the selective association of lithium cation and TFSI anion on the negatively charged outer surface and positively charged inner

surface respectively. Furthermore, the addition of halloysite nanotubes reduces the crystallinity of CSSEs which facilitates the transport of lithium ion in polymer matrix.²⁴⁴

Jiawei et al. believe that the compatibility of inorganic fillers is not good enough to ensure through mixing with polymer matrix of CSSEs. To avoid the drawback of inorganic filler, an organic polyphosphazene (PZS) nanotube is chosen as the filler of CSSEs²⁴⁵. The good compatibility can be simply revealed by the smooth surface of PZS nanotube/PEO(LiClO₄) CSSEs even when the PSZ filler content is as high as 10% and the conductivity is about 1.5×10^{-5} S cm⁻¹ at RT. In addition, the ion transference number of this CSSEs can achieve 0.35 which is much higher than that of CSSEs with silica nanoparticles (0.24). The possible reason is that the N, O, and S atoms at the surface of PZS nanotube can interact with lithium ions and dissociate lithium salt more efficiently.

Besides the surface chemistry, fillers can also be used to guide the crystal orientation of PEO-LiX solution. Zlatka and co-workers showed that the crystalline (PEO)₆-LiX can have one order magnitude higher conductivity compared with its amorphous equivalent when the lithium ion diffusion direction is along the polymer chain helix²⁴⁶. However, the polymer chain helix is usually parallel to the CSSEs membrane which is due to the conventional solution casting method. To solve this problem, Schaetzl et al. prepared Fe₂O₃ nanorods with γ -phase (maghemite)@ α -phase (hematite) core-shell structure²⁴⁷. This structure combines the good surface chemistry of α -Fe₂O₃ with the high ionic conductivity and high susceptibility of γ -Fe₂O₃ for alignment of PEO helices perpendicular to the CSSEs membrane surface. With these two factors, the conductivity of Fe₂O₃ nanorod/PEO(LiClO₄) composites increase by three orders of magnitude at room temperature.

3.1.1.3. 2D fillers

The mechanism of lithium ion conductivity with use of inactive fillers is mainly based on the polymer-filler interface. One of the shortcomings of inactive filler is that the inner part of fillers which is not in contact with the polymer phase can reduce the total ionic conductivity: they occupy the volume of electrolyte film but cannot provide ionic conductivity. Compared with 0D or 1D fillers, 2D fillers could be a better choice since there is no "inner" part inside the 2D materials. But the drawback of 2D filler is also obvious: (1) 2D materials may curl up or aggregate which make it hard to fully used their surface; (2) 2D materials may distribute perpendicular to the direction of lithium ion conduction which will hinder the diffusion of lithium ion. The 2D materials used as fillers are introduced in the following paragraphs.

Graphene is the most famous 2D material and has been widely used in electronic and electrochemical devices. But the electronically conductive nature makes it difficult to use it safely as filler in CSSEs. However, the oxidation state of graphene, GO, is a suitable material as filler for CSSEs²⁴⁸⁻²⁵². GO has a similar structure to graphite oxide which contains sp² hybridized carbon atoms and multiple oxygenated functional groups (such as C-O-C, -CO, -OH and -COOH) decorating the basal planes and edges. W. Jia et al. and S. Gao et al. both added GO in polymer matrix and observed an improved lithium ion conductivity of $\sim 10^{-4}$ S cm⁻¹^{248,250}. The conductivity improvement is mainly attributed to the reduced crystallinity of polymer matrix due to

GO/polymer chain interaction and the fast ion conduction layer formed at GO/polymer interface. In addition, GO can also improve the mechanical strength of CSSEs. The GO/Polymer interaction can also be improved by graft polymer chains on GO nanosheet. J. Shim et al. grafted PEO chains on the GO nanosheet through condensation reaction between -COOH on GO and -OH in PEG polymer chains²⁴⁹. The highest conductivity achieved was 2.1×10^{-4} S cm⁻¹ but part of the conductivity improvement comes from the polymer they synthesized.

Layered double hydroxides (LDHs), as a kind of typical 2D materials, have been used in numerous fields, such as catalysis, biomedical applications, and energy storage systems due to their high specific area and abundant electroactive sites. Of course, LDH can also be used in solid electrolyte as a 2D filler. C. Liao and W. Ye intercalated oligo(ethylene oxide) with phosphonate anion into the gallery region of LDH and form a PEO-modified LDH^{253,254}. The modified LDH has higher compatibility with PEO polymer matrix and can be finely dispersed in polymer matrix which can effectively retard the crystallization of PEO. The conductivity of CSSEs is improved to 2.1×10^{-4} S cm⁻¹ at 30°C.

MXene is another kind of 2D material. Z. Huang et al. studied the crystallization behavior of PEO/Ti₃C₂T_x MXene nanocomposite²⁵⁵. The results show that PEO polymer chains have a strong interaction with MXene surface through the highly polar function groups on MXene surface. Suitable content (2% ~ 5% wt%) of MXene can slow down the crystallization rate of PEO polymer chains. Q. Pan et al. prepared the PEO based solid electrolyte with MXene as filler²⁵⁶. The conductivity is improved to 2.2×10^{-5} S cm⁻¹ at 28°C when the filler content is 3.6 wt%.

Exfoliated natural mineral fillers are also effective in improving the ionic conductivity of polymer based solid electrolytes. Minerals/clays are usually silicates with a polar surface and can be further exposed by delamination. In addition, the mechanical strength, electrochemical stability, and thermal stability can also be improved. Exfoliated Vermiculite is chemically and thermally stable with robust mechanical properties. The surface of vermiculite nanosheets is negatively charged because the Al replacement of Si which ensures a strong interaction with PEO polymer chains. Together with the ion exchange with lithium, a lithium conductive layer on the vermiculite nanosheets can be formed to improve the total conductivity of CSSEs. W. Tang et al. prepared a vermiculite nanosheets/PEO composites by mixing vermiculite nanosheets, PEO, and LiTFSI together²⁵⁷. The highest conductivity of this kind of composites achieve 2.9×10^{-5} S cm⁻¹ at 25°C.

B. Wang et al. used lepidolite as filler in PEO matrix with LiClO₄ as lithium salt and the CSSEs achieved it highest conductivity of 1.39×10^{-6} S cm⁻¹ at RT²⁵⁸. It is valuable to point out that even pure compressed lepidolite pellet and PEO/lepidolite composite without lithium can also give ionic conductivity of 1.6×10^{-7} S cm⁻¹ and 1.2×10^{-7} S cm⁻¹ at RT respectively which prove that in lepidolite/PEO(LiClO₄) composite, lithium ion can conduct in both polymer matrix and fillers.

3.1.2. Active nanofillers

3.1.2.1 0D nanofillers

Compared with inactive fillers which are inert in ionic conduction, active fillers which have high ionic conductivity can be a better choice as filler in polymer matrix. The ionic conduction improvement of CSSEs with inactive fillers are mainly attributed to the interface between fillers and polymer matrix. To improve the volume fraction of interface between fillers and polymer matrix, one method is to increase the content of filler. But when more fillers are added to the polymer matrix, the ionic conductive volume of CSSEs decreases even though the interface area increased due to the inactive nature of inactive fillers. Substituting the inactive filler with active filler can improve the volume fraction of highly conductive interface region without reduce conductive volume of CSSEs by simply adding more filler in polymer matrix.²⁵⁹ Moreover, lots of researches have tried to investigate the role of active fillers in ionic conduction improvement.

Similar with the CSSEs with inactive fillers, the interface between active fillers and polymer matrix also play an important role in ionic conduction when active filler is used. Z. Li et al. observed the space charge region between Ga doped LLZO nanoparticles and PEO matrix. The space charge region is around 3 nm in thickness and the driving force of forming such region is the reduction of free energy. Ga-LLZO nanoparticle has relative high free energy due to the defects on particle's surface. When Ga-LLZO nanoparticles are mixed with PEO matrix, the lithium ions and vacancies are re-distributed forming a space charge region and hence the free energy is reduced. This space charge region has high ionic conductivity and contributes a lot to the total conductivity of CSSEs²⁶⁰. W. Wang et al. studied the PEO based CSSEs with LATP as filler and arrived at similar conclusions.

By comparing the CSSEs with inactive (TiO_2 and Al_2O_3) to active (LATP) fillers, it can be found that the main factor for improving in ionic conductivity of the latter CSSEs is not the improved amorphous region via suppressing crystallinity. Unlike inactive fillers, active fillers are more likely to reconstruct the interface between filler particles and polymer matrix. It is believed that the conductivity enhancement is mainly attributed to the percolation across the interface, and the interfacial region could easily expand to twice of particle radius²⁶¹. The percolation effect can be also proved by J. Zhang and his co-worker's work. They studied the size effect of LLZTO filler and the results shows that the percolation threshold decreases when filler with smaller particle size is used. The CSSEs with ~40 nm LLZTO particles shows nearly two orders of magnitude improvement compared with CSSEs with micro size ones. The PEO/LLZTO electrolyte can also effectively suppress the dendrite formation by well dispersed filler particles²⁶². The interaction between filler particles and polymer matrix can be varied when different fillers and polymer are used. The PVDF/LLZTO CSSEs were synthesized by X. Zhang et al. and the special interfacial structure were characterized. The PVDF/LLZTO CSSEs have a very interesting phenomenon: when LLZTO particles are introduced in PVDF the color of CSSEs changed. This phenomenon can be attributed to the chemical structure change in PVDF. The FTIR study shows that when filler is added in PVDF matrix, the deprotonation of CH_2 and the dehydrofluorination of PVDF chains occurs. In addition, the partially dehydrofluorinated PVDF and LLZTO particles can effectively dissociate lithium salts by complexing with Li ion which increases the lithium ion density, and hence, the ionic conductivity of CSSEs²⁶³. The interface between sulphur based filler and polymer

matrix is slightly different with that between oxide based filler and polymer matrix due to its soft mechanical properties. J. Zheng et al. prepared a LAGP/PEO(LiTFSI) CSSEs and studied the ionic conduction by NMR. The experimental results also proved that the ionic conduction is mainly through LAGP/PEO interface. They believe that the LLZO filler is too rigid to closely integrated with polymer matrix. In contrast, LAGP which is soft and cementing can easily maximize ionic conduction interface through ball milling mixing, leading to improved ionic conductivity²⁶⁴.

Surface modification has also been used to improve the interface property of CSSEs. Z. Huang used dopamine to modify the surface of LLZTO which significantly increased the wettability of LLZTO with PEO. This wettability improvement enables 80 wt% LLZTO to be dispersed in PEO(LiTFSI) matrix, leading to an ionic conductivity enhancement from 6.3×10^{-5} to 1.1×10^{-4} S cm^{-1} at 30°C ²⁶⁵. W. Li et al. used a molecular brush to modify LLZTO which provides an alteration of lithium ion conduction pathway, and the functional groups can attract anions and reduce the interaction between lithium ions and polymer chains. In addition, the modification can coordinate with the polymer matrix which increases the interaction between filler particles and polymer matrix and consequently reduces the crystallinity of the polymer matrix²⁶⁶.

Even though the importance of interface has been proved by numerous literatures, the ionic conduction mechanism in CSSEs with active filler is still ambiguous. Several papers tried to investigate the ionic conduction in CSSEs via NMR. J. Zheng et al. published two papers discussing the lithium ion conduction pathway in CSSEs and they found the ion conduction pathway is related to the content of fillers^{267,268}.

When the content of active filler is low (i.e. 5 wt%), the active lithium ions are solely form lithium salts, and the active particles mainly serve as a filler to suppress the crystallization of polymer matrix. Several papers used this methodology to synthesize CSSEs with different kinds of active fillers²⁶⁹⁻²⁷⁴. When the content of active filler increases (to around 20 wt%), the role of active filler changes. The active lithium ions not only come from lithium salts but also come from the lithium ions inside LLZO particles which actually increases the concentration of lithium ions in polymer matrix. At the same time, the percolated filler network gradually contributes more in lithium ion conductivity. This transition are influenced by many factors including particle size, particle morphology, surface chemistry of filler, uniformity of mixing and so on^{269,275-277}. When the content of active filler further increases (to around 50 wt%), the active fillers contribute more active lithium ions in CSSEs even without adding any lithium salts in polymer matrix^{260,278,279}. But with the increasing of filler content, the lithium ion mobility decreases and the lithium ion conduction pathway changes to the loosely connected filler particles possible due to the blockage of lithium ion conduction by filler particles. However, because the connection between filler particles are not sufficient to provide high ionic conductivity, the conductivity of high active filler content CSSEs usually cannot achieve relatively high ionic conductivity^{269,276,278-281}. Using plasticizer is an effective way to improve the mobility of polymer segment, dissociation of lithium salt and suppress the crystallization of polymer matrix, leading to improved lithium ion conductivity. The addition of plasticizer changes the ionic conduction pathway from connected filler particles to polymer matrix when the filler content is high. A variety of

plasticizers such as poly(ethylene glycol) dimethyl ether^{268,282}, succinonitrile^{273,283}, ionic liquid^{184,284}, boronized polyethylene glycol²⁸⁵, and etc. have been used in CSSE systems.

3.1.2.2 1D and 2D fillers

Compared with inactive fillers, active fillers with continuous surface can give a similarly improved ionic conductivity because of the continuous and highly conductive percolated pathway between different phases. Until recently, 1D and 2D active fillers could not be formed *in situ* with a handful of exceptions such as R.F. sputtering of glass LiPON on the nano- to microscale where tailored structure is not required. This was largely due to the higher chemical and structural complexity of active fillers, when possibly a lack of throughout investigation of growth mechanism of active filler under different environment prohibited the development of structured, *in situ* formed active fillers. Namely, preparation of 1D or 2D active fillers through bottom up method lacks theoretical guidance. And at the same time, it is almost impossible to synthesize 2D active filler by exfoliation not only because some of the active fillers are not layered structure but also because lithium ion is the specie most easily to be removed in active fillers. Hence, the exfoliated active filler is likely to become inactive.

Due to the above-mentioned reasons, 1D and 2D active fillers have mainly been prepared by template method^{286–295}. Electrospinning is the most widely used method to prepare active filler nano fiber. W. Liu et al. prepared LLTO nanofiber by calcinating the electrospun polyvinylpyrrolidone (PVP) fiber containing LiNO₃, La(NO₃)₃, Ti(OC₄H₉)₄ and acetic acid²⁹⁴. The synthesized nanofibers have a diameter of around 300nm with high aspect ratio. The CSSEs with such LLTO nanofiber as filler have a high ion conductivity of 2.4×10^{-4} S/cm at room temperature. The conductivity improvement is mainly attributed to the surface vacancies of LLTO nanofiber. Lithium ions can hop from one vacancy to the next one which results in increased ion mobility and hence increased ion conductivity. Li₇La₃Zr₂O₁₂ nanowire is synthesized with a similar method by T. Yang and his co-workers²⁹³. The CSSEs with LLZO nanowire as filler have a conductivity of 1.31×10^{-4} S cm⁻¹.

The study on 2D active filler is quite limited compared with other dimensions. The possible reason is that most of the current techniques cannot prepare large amount of material with fine morphology which can meet the requirements as a filler. S. Song. et al. tried to synthesize garnet nanosheets by co-precipitation method with graphene oxide as template²⁸⁶. The conductivity of CSSEs with the prepared nanosheets as filler can achieve 3.6×10^{-4} S/cm at ambient temperature which is 4 orders of magnitude higher than the undoped polymer based solid electrolyte. The conductivity improvement can be attributed to the interconnected structure which provide a continuous lithium ion transport pathway. However, rather than nanosheets, it is more accurate to describe the filler as “sheet like aggregates”. To achieve an ideal 2D filler, synthesis techniques and especially dispersing methods are crucial areas to pursue.

3.2. Heterogeneous layered structure

Aside from the inorganic fillers in polymer matrix, another typical structure, the layered CSSE consisting of inorganic and/or polymeric electrolytes used in ASSLB is becoming a hot research

point in the very recent two to three years. One obvious advantage of this structure is to combine the intrinsic advantages and address the drawbacks of each layer, such as the improvement of ionic conductivities and mechanical strength of polymeric electrolyte after adding inorganic layer to a polymer layer, or enhancement of the flexibility of ceramics after combining with polymer layers.¹⁶

In addition to improving the properties of composited electrolytes themselves, another typical superiority is the interfacial contact between electrolyte and electrode. Namely, the interfacial issues can be alleviated or even resolved using the CSSEs with layered architecture, which includes the issues at anode/electrolyte interface of poor contact or wetting, side reactions, and lithium dendrite²⁹⁶, or the problems such as large interfacial impedance, element interdiffusion, and also side reactions caused by high-voltage decomposition and space charge layer especially at cathode/electrolyte interface. In this regard, John B. Goodenough, Xueliang Sun, Lijun Wan, and Liangbin Hu’s groups published many works, all those related Heterogeneous layered structure can be divided into the double-layered type^{297,298} and sandwich-type (three-layered) architecture²⁹⁹.

3.2.1. Double-layered architecture

First, as for the CSSE with double-layered architecture, the polymer sandwiched between the ceramic electrolyte pellet and lithium metal anode usually acts as an artificial solid-electrolyte interphase (SEI) layer. Such as the PAS-PEO polymeric layer (PAS, poly(acrylamide-2-methyl-1-propane-sulfonate)) was processed to wet the interphase of Li_{6.5}La₃Zr_{1.5}Ta_{0.5}O₁₂ (LLZTO) ceramic pellet and lithium metal as shown in Fig. 7, thus leading a significantly reduced interfacial resistance between them.²⁹⁸ Moreover, another case proposed a novel perovskite electrolyte Li_{0.38}Sr_{0.44}Ta_{0.7}Hf_{0.3}O_{2.95}F_{0.05} (LSTHF5) synthesized via spark plasma sintering (SPS) and coat with a thin Li⁺-conducting polymer²⁹⁶, or adding 2 wt% LiF into LLZO layer and then combined with a gel polymer layer to form a LLZO-LiF/gel polymer solid electrolyte²⁹⁷.

3.2.2. Symmetrical sandwiched architecture

Regarding the CSSEs with sandwiched architecture, the polymeric layer is usually used as a soft interphase to improve the contact between hard inorganic electrolyte and both cathode and anode. As a typical example, Weidong Zhou et al.²⁹⁹ proposed a polymer/ceramic/polymer symmetrical sandwich electrolyte (PCPSE) to deal with the interfacial problems. To be specific, a cross-linked Li⁺ polymer conductor, poly(ethylene glycol) methyl ether acrylate (CPMEA) (Fig. 7 (c)), was first synthesized and further combined with an active ceramic membrane of Li_{1.3}Al_{0.3}Ti_{1.7}(PO₄)₃ (LATP) to form a sandwiched CSSE, in which the lithium salt anion transfer can be blocked to reduce the double-layer electric field, and the Li-ion flux at the interface of polymer and lithium metal anode is much more homogeneous due to their soft contact and almost random ion conduction pathways allowing for even diffusion. As a consequence, the corresponding LiFePO₄/Li cell exhibits superior long-term electrochemical stability and a high columbic efficiency (99.8-100%). Very recently, another similar CSSE PEO/LLZTO/PEO (LLZTO, Li_{6.4}La₃Zr_{1.4}Ta_{0.6}O₁₂) combined with 3D Li metal anode (Fig. 7 (d)) was also proposed and the corresponding symmetrical cell and full cell with LiFePO₄ as cathode exhibited a good cycle stability during

700 hours and 200 hours running at 90°C, respectively.³⁰⁰ On these bases, the middle inorganic layer can be further modified to improve the durability, such as ALD modification for LAGP layer to form a PEO/ALD-coated (Al₂O₃) LAGP/PEO CSSE to achieve a further significantly enhanced cycling performance.³⁰¹

Another symmetrical sandwiched architecture is the opposite, namely, the sandwiched inorganic/polymer/ inorganic architecture. Here a two-dimensional (2D) boron nitride nanosheets (BNNs) is coated onto the surface of PEO polymeric layer to form the opposite structure as shown in Fig. 7 (e)³⁰², which enables the PEO layer to achieve a good mechanical stability and homogeneous Li⁺ ion flux distribution. Consequently, the corresponding Li/LFP ASSLB cell show a specific discharge capacity of 110 mA h g⁻¹ at 2C over 200 cycles.

Strictly speaking, comparing to the dry polymers mentioned above, gel polymers containing liquid electrolyte can't be regarded as

all-solid-state electrolyte. However, considering the tradeoff between the performance (ionic conductivity especially) and safety, some studies still introduced them into the electrolytes with similar symmetrical sandwiched structure³⁰³. For example, as shown in Fig. 7 (f), Boyang Liu et al. proposed the composite electrolyte of gel polymer/ceramic/gel polymer to deal with the poor interfacial contact of garnet ceramic Li₇La_{2.75}Ca_{0.25}Zr_{1.75}Nb_{0.25}O₁₂ (LLCZNO) electrolyte and the electrodes³⁰³. The gel polymer layers composed of dry polymer (PVDF-HFP) and liquid electrolyte. Liquid electrolytes are used in this case due to that the gel electrolyte interlayers can be manufactured at lower temperature, which is more scalable for actual application. On this basis, some researchers changed one polymeric layer in gel polymer/ceramic/ gel polymer into a 20 nm germanium layer to form a Ge/LLZO/gel polymer solid electrolyte as shown in Fig. 7 (g)³⁰⁴, thus turning to a three-layer CSSE with an asymmetric sandwiched architecture, which will be detailed below.

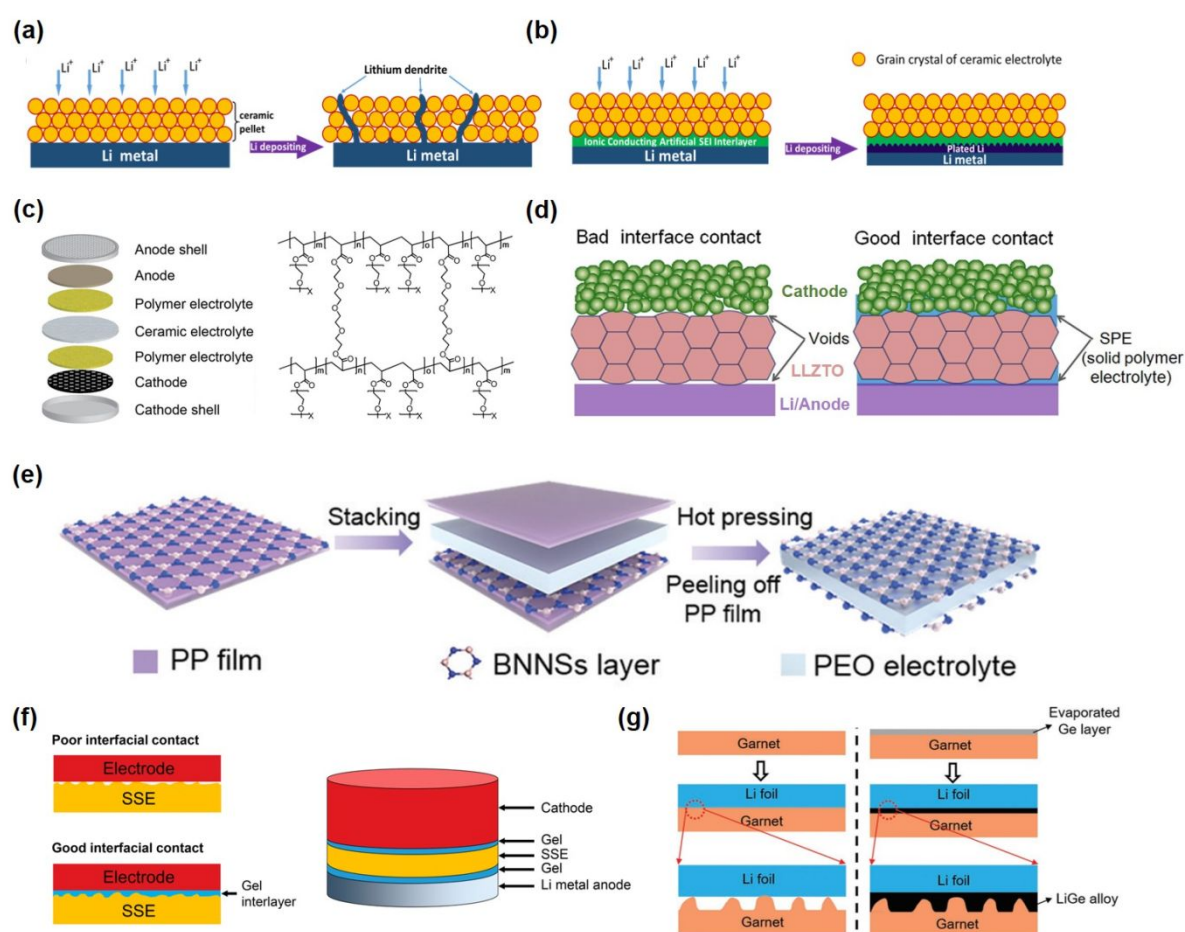


Fig. 7 Schematic diagrams of lithium plating process in an ASSLB with SSE (a) without and (b) with an Li-ion conductive PAS-PEO layer to wet the metallic lithium anode and garnet electrolyte.²⁹⁸ Reprinted with permission from ref. 298. Copyright 2018, Elsevier Ltd. Schematics of the sandwiched CSSE and related ASSLBs. (c) The design of ASSLB with symmetrical sandwiched structure and the structure of polymer cross-linked poly(ethylene glycol) methyl ether acrylate (CPMEA)²⁹⁹, reprinted with permission from ref. 299. Copyright 2016, American Chemical Society. (d) the bad/good interface contact without/with solid polymer electrolyte between the LLZTO layer and electrodes³⁰⁰; reprinted with permission from ref. 300. Copyright 2019, Elsevier Ltd. (e) the preparation process for CSSE of boron nitride nanosheets (BNNs)/PEO/BNNs³⁰²; reprinted with permission from ref. 302. Copyright 2019, Royal Society of Chemistry. (f) the interface improvement without and with gel interlayer (left), and the related structure of full battery (right)³⁰³; reprinted with permission from ref. 303. Copyright 2017, American Chemical Society. (g) interfacial contact between garnet and Li metal with or without the surface engineering of a thin Ge layer³⁰⁴, reprinted with permission from ref. 304. Copyright 2017, Wiley-VCH.

3.2.3. Asymmetric sandwiched architecture

As for asymmetric sandwiched architecture, another typical case in point is a thin asymmetric CSSE with engineered layers, as shown in Fig. 8 (a)³⁰⁵. Aside from the middle LLZO layer, a 7.5 nm polymer electrolyte is modified on the surface of dense LLZO layer on the lithium metal side, and an additional three-layer architecture is attached to the cathode side, which is consisted of a LLZO-coating film (5.7 μm), a commercial Celgard 2400 separator, and a polymer electrolyte (5.4 μm). As a consequence, not only can lithium dendrite penetration be prevented in anode side, but also sufficient contact

between electrolyte and active materials can be achieved on the cathode's side. All this result in a high ionic conductivity of $1 \times 10^{-4} \text{ S cm}^{-1}$ at 55°C, a wide electrochemical windows up to 4.8 V, and an exceptional dendrite-free Li cycling over 3200 hours as shown in Fig. 8 (b).

Furthermore, Kun (Kelvin) Fu *et al.*³⁰⁶ proposed a 3D bilayer garnet solid electrolyte used in lithium metal-sulfur batteries as shown in Fig. 8 (c). The porous LLZO layer is coated with CNT and in contact with the cathode, and the dense LLZO layer could be coated with PEO polymeric gel layer conformably to fill the isolated pores for better contact with the lithium metal anode, thus enabling a homogeneous Li ion flux through the interface.

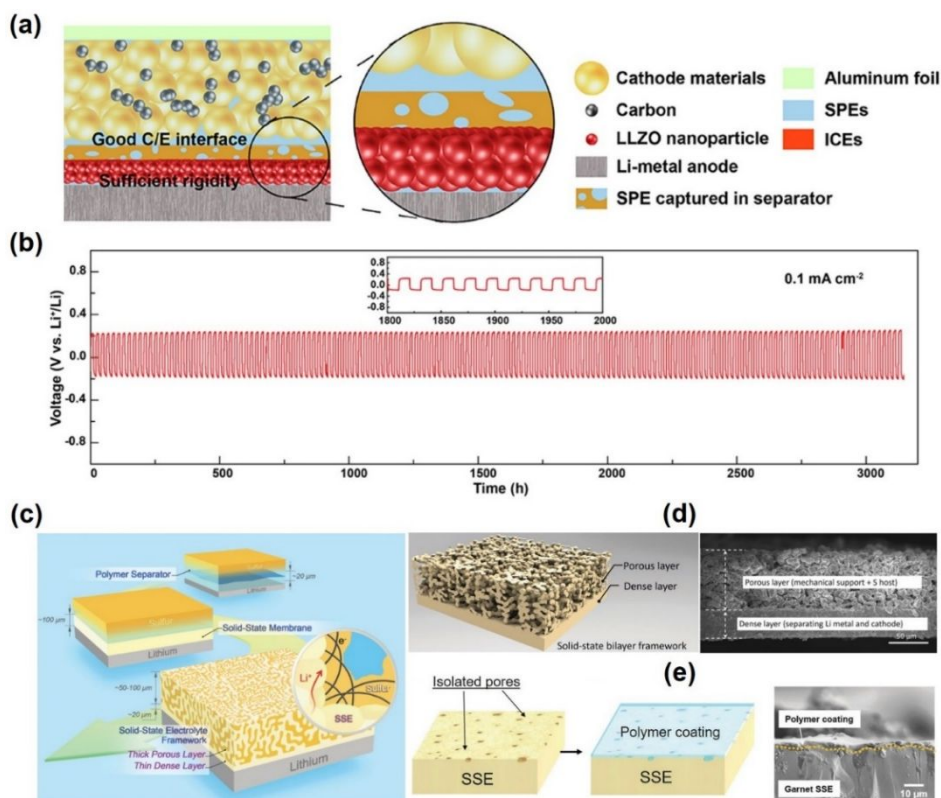


Fig. 8 (a) Schematic diagrams of ASSEB with a thin asymmetric solid electrolyte (ASE) of PAN/LAGP/PEGDA; (b) voltage profile for the Li/ASE/Li symmetrical battery and its magnified curve.³⁰⁵ Reprinted with permission from ref. 305. Copyright 2018, American Chemical Society. (c) Schematics of lithium batteries with the electrolytes from the traditional liquid electrolyte with polymer separator to typical SSE, and the novel bilayer solid-state electrolyte; (d) schematic of garnet bilayer framework after sintering and the SEM image of its cross-section in cathode side; (e) Schematic of the polymer coated dense garnet layer surface and the SEM image of its cross-section in lithium metal anode side.³⁰⁶ Reprinted with permission from ref. 306. Copyright 2017, Royal Society of Chemistry.

In addition to the general combination of pristine ceramic and pure polymer (contain lithium salt) layers, another method is to take the polymer layer as matrix filled with active/inactive inorganic particles, i.e. a composite electrolyte as review above, and then combine with another ceramic pellet to form the layered CSSE. As a consequence, the obtained CSSEs can achieve better performance such as ionic conductivity and mechanical property.

For instance, some researches first mixed the 75% (wt.) Li_2S /24% P_2S_5 /1% P_2O_5 particles as active fillers into PEO polymer matrix to form a polymer based layer (LPOS), and then coated on a LAGP pellet to form a CSSE with double layers as shown in Fig. 9 (a). The all-solid-state LFP/Li cell delivered very long-term electrochemical

stability and high columbic efficiency. To be specific, the reversible discharge capacity is $127.8 \text{ mA h g}^{-1}$ after 1000 cycles running at 1C, with capacity retention of 96.6%³⁰⁷. Additionally, based on the systematical investigations of the CSSE from “ceramic-in-polymer” (CIP, high ceramic, low polymer content) to “polymer-in-ceramic” (PIC, high polymer, lower ceramic content) with various ceramic ratios and particle sizes, a sandwich-type CSSE of CIP/PIC/CIP consisted of a PIC layer with superior mechanical strength and two PIC layers with better flexibility is constructed as shown in Fig. 9 (b) and (c), achieving excellent interfacial contact with Li metal and dendrite suppression simultaneously.³⁰⁸

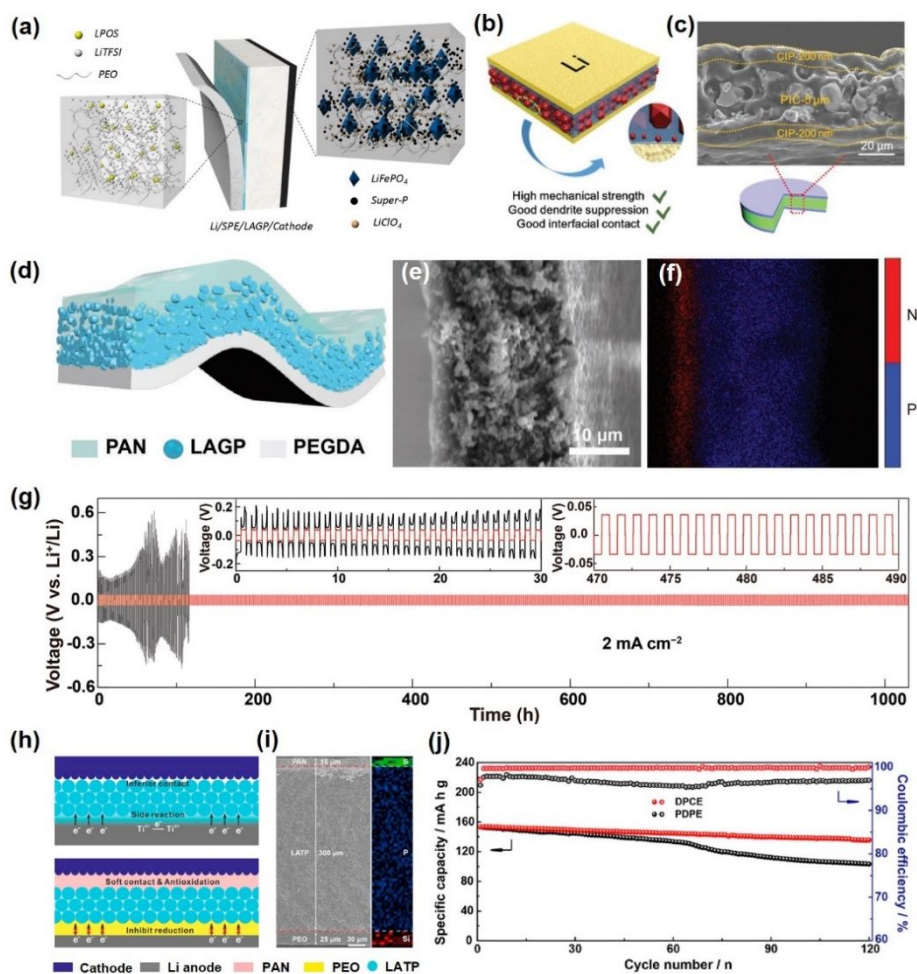


Fig. 9 (a) Schematic of the ASSEB with a CSSE consisted of “Particles in polymer” composite electrolyte and an additional polymer layer³⁰⁷. Reprinted with permission from ref. 307. Copyright 2017, Royal Society of Chemistry. (b) Schematic illustration of the PIC-5 μm , CIP-200 nm, and hierarchical sandwich-type composite electrolyte, and (c) its cross-sectional SEM image (garnet particles with different sizes (200 nm and 5 μm)³⁰⁸. Reprinted with permission from ref. 308. Copyright 2019, Wiley-VCH. Sandwich-type CSSE used in high-voltage ASSEBs. (d) Schematic diagram, (e) SEM image and (f) EDS mapping (N and P) of the Janus PAN/LAGP/PEGDA CSSE, and (f) voltage profile for the Li symmetrical battery with this CSSE and liquid electrolyte at a current density of 2 mA cm⁻².³⁰⁹ Reprinted with permission from ref. 309. Copyright 2019, Wiley-VCH. (g) Schematic diagrams of the solid full battery with LATP (upper) or PAN/LATP/PEO (lower) as electrolyte. (h) SEM image and EDS mapping (N and P) of the Janus PAN/LAGP/PEO CSSE. (i) cycling performances of the full batteries with DPCE (disparate polymers protected ceramic electrolyte) and PDPE (high-voltage resistance PAN/LATP/PEO solid electrolyte) under 0.5C.³¹⁰ Reprinted with permission from ref. 310. Copyright 2019, American Chemical Society.

3.2.4. Structures towards high-voltage lithium batteries

More recently, high-voltage ASSEBs have attracted extensive attention due to possible higher capacity and energy density. However, the requirement of stability for solid electrolyte against electrodes is still not fully satisfied under such high voltage condition, thus some advanced materials or/and structures used in SSE are required to be developed³⁰⁹. In this regard, the CSSE with layered architecture can also be a possible solution to overcome the instability problems in high-voltage ASSEBs. For instance, Hui Duan et al.³⁰⁹ designed a Janus PAN(poly(acrylonitrile))/LAGP ($\text{Li}_{1.4}\text{Al}_{0.4}\text{Ge}_{1.6}(\text{PO}_4)_3$) (80 wt%)/PEGDA (polyethylene glycol diacrylate) composite electrolyte with sandwiched architecture as shown in Fig. 9 (d) to (f), in which the oxidation tolerant PAN and reduction-resistant PEGDA are used in cathode (high-voltage cathode especially) and anode sides respectively to avoid side reactions and enlarge electrochemical

window. Moreover, a similarly sandwiched CSSE PAN/LAGP/PEO is also proposed in the same research group of Lijun Wan’s, as shown in Fig. 9 (h) and (i)³¹⁰. Here the PEGDA layer is changed into a more commonly used polymer, i.e. reduction-reaction inhibited polyethylene oxide (PEO). These two similar CSSEs all show stable polarization for more than 1000 hours at current density of 2 mA cm⁻² (a case as shown in Fig. 9 (g)) and excellent cycling stability in related symmetrical or high-voltage full cells (the other case as shown in Fig. 9 (j)).

Furthermore, another recent research on similar polymer/ceramic/polymer (MEEP/LATP/PVDF-HFP) (Fig. 10 (a)), MEEP, poly[bis(2-(2-methoxyethoxy)ethoxy) phosphazene], PVDF-HFP, poly(vinylidene fluoride-co-hexafluoropropylene)) CSSE was also studied and resulted in a long lifespan ASSEB with high-voltage cathode of $\text{Li}_3\text{V}_2(\text{PO}_4)_3/\text{CNT}$ ³¹¹. Notably, the coating of polymer layers on the

ceramic pellet significantly widened the electrochemical windows to 0-4.7 V (Fig. 10 (b)), and also improve the electrochemical stability (Fig. 10 (c)).

In addition to the CSSEs composed of inorganic and polymer, there still few CSSEs that are consisted of different polymers. A case in point is the double-layer polymer electrolyte with PMA (contain

LiTFSI) and PEO (contain LiTFSI) Fig. 10 (d) to (f), which act as high and low voltage stable polymer electrolyte respectively. As a result, the Li/PEO/PMA/LCO (LCO, LiCoO_2) ASSLIB shows a good stability without lithium dendrite at PEO/anode interface and no oxidation at PMA/cathode interface even under high-voltage operation.³¹²

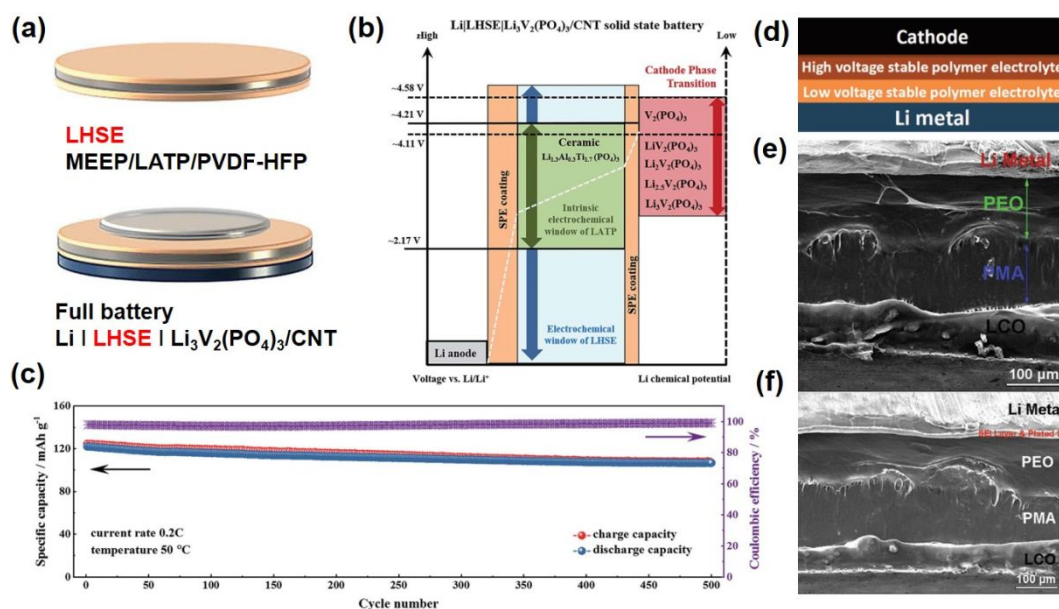


Fig. 10 CSSEs with the architectures of polymer/ceramic/polymer or polymer/polymer. CSSE of MEEP/LATP/PVDF-HFP (LHSE, layered hybrid solid electrolyte): (a) Illustrations (upper) and the corresponding full lithium battery (lower), (b) electrochemical compatibility of the battery components regarding voltage and chemical potential in regards to $\text{Li}/\text{LHSE}/\text{Li}_3\text{V}_2(\text{PO}_4)_3/\text{CNT}$. (c) long-term cycling measurement at a current rate of 0.2C³¹¹. Reprinted with permission from ref. 311. Copyright 2019, Royal Society of Chemistry. CSSE of PEO/PAN: (d) Illustration of the corresponding full lithium battery, SEM image (e) before and (f) after cycling 100 cycles at 65°C.³¹² Reprinted with permission from ref. 312. Copyright 2019, Wiley-VCH.

3.3. 3D inorganic continuous framework with filled polymer

It is commonly recognized that the addition of inactive or active inorganic nanoparticles into polymer matrix can significantly enhance the typical performance and ionic conductivity due to the reduced crystallinity of polymeric chains²²¹⁶. Moreover, many researchers found that the ionic conductivity of CSSEs can be further enhanced after adding some randomly dispersed inorganic nanowires or nanorods, which could offer a more continuous fast conduction pathway for Li ion. Very recently, three-dimensional (3D) nanostructured inorganic frameworks filled with polymer have been developed which provide continuous 3D channels and are free of crossing junctions between inorganic phases, thus facilitating ion transport even further than 1D nanowires or nanorods³¹³. Other than the ionic conductivity, the mechanical strength and long-term stability of the CSSEs can also be improved according to this structural change trend.

Regarding the specific material types used in this kind of 3D CSSEs, the inorganic frameworks are usually made from inactive conductors SiO_2 , palygorskite ($(\text{Mg},\text{Al})_2\text{Si}_4\text{O}_{10}(\text{OH})$), and anodic aluminum oxide (AAO)^{109,314}; or active conductors LLZO, LATP/LAGP, and LLTO. The typical polymeric filler is PEO, and some others are PAN, PVDF. Here we divide those advanced 3D inorganic frameworks used in CSSEs into three main categories,

including 3D interconnecting fiber filled with polymer, 3D continuous network filled with polymer, and vertically aligned 3D framework filled with polymer. More details can be seen as follows.

3.3.1. 3D interconnected fiber network

Based on the researches for the fillers of inorganic 1D nanowire (or nanorod, nanofiber) in polymer matrix as summarized in last section, much more interconnections between those separated 1D nanowires can be constructed into a 3D inorganic continuous framework, then filled with polymers (contained lithium salt) to form the final CSSEs. As shown in Fig. 11A (a), Kun (Kelvin) Fu et al.⁸⁹ first proposed a 3D lithium-ion conducting ceramic network based on $\text{Li}_{6.4}\text{La}_3\text{Zr}_2\text{Al}_{0.2}\text{O}_{12}$ (LLZO) in PEO-based composite to form a novel, flexible, solid-state, ion-conducting CSSE used in lithium battery. The garnet LLZO nanofibers are prepared by electrospinning of the related precursor, and a subsequent calcination at 800°C in air for 2 h to create interconnected fibers. Unlike the traditional mixing of the inorganic particles or dispersing nanofibers into polymer matrix, the obtained 3D interconnected network is directly soaked into polymer based solutions to form the fiber-reinforced polymer composite (FRPC), thus avoiding the agglomeration of fillers. As a consequence, the obtained CSSE exhibits a good flame resistance after flammability tests, high ionic conductivity of 2.5×10^{-4} at RT, wide electrochemical

window up to 6.0 V vs. Li/Li⁺, and a good cycling stability with long cycle life as well. Some results are listed in the Table 5 below.

After that, some CSSEs with very similar structure are investigated, with the materials of 3D inorganic nanowires and polymer being changed into Li_{0.33}La_{0.557}TiO₃ (LLTO) and PVDF with LiTFSI respectively,³¹⁵ or an inactive inorganic conductor palygorskite ((Mg,Al)₂Si₄O₁₀(OH)) and PVDF with LiClO₄ respectively (Fig. 11A (b))³¹⁶. While in the latter one, a Li|CSSE (palygorskite-PVDF)|NMC111 (Li(Ni_{1/3}Mn_{1/3}Co_{1/3})O₂) full battery

was assembled and showed a capacity of 121.4 mAh g⁻¹ at C/3 and cycling over 200 cycles steadily. Deliverable capacity of 118.1 mAh g⁻¹ still remained after this 200 cycles at RT. Another case as shown in Fig. 11A (c) and (d) is a little different, in which the network filler is composed of Li_{1.4}Al_{0.4}Ti_{1.6}(PO₄)₃ (LATP) and (PAN), and then combining with PEO matrix. Therefore, the side reaction between Ti⁴⁺ in LATP and Li metal could be avoided due to the envelop of LATP particles by the polymeric chains of PAN.

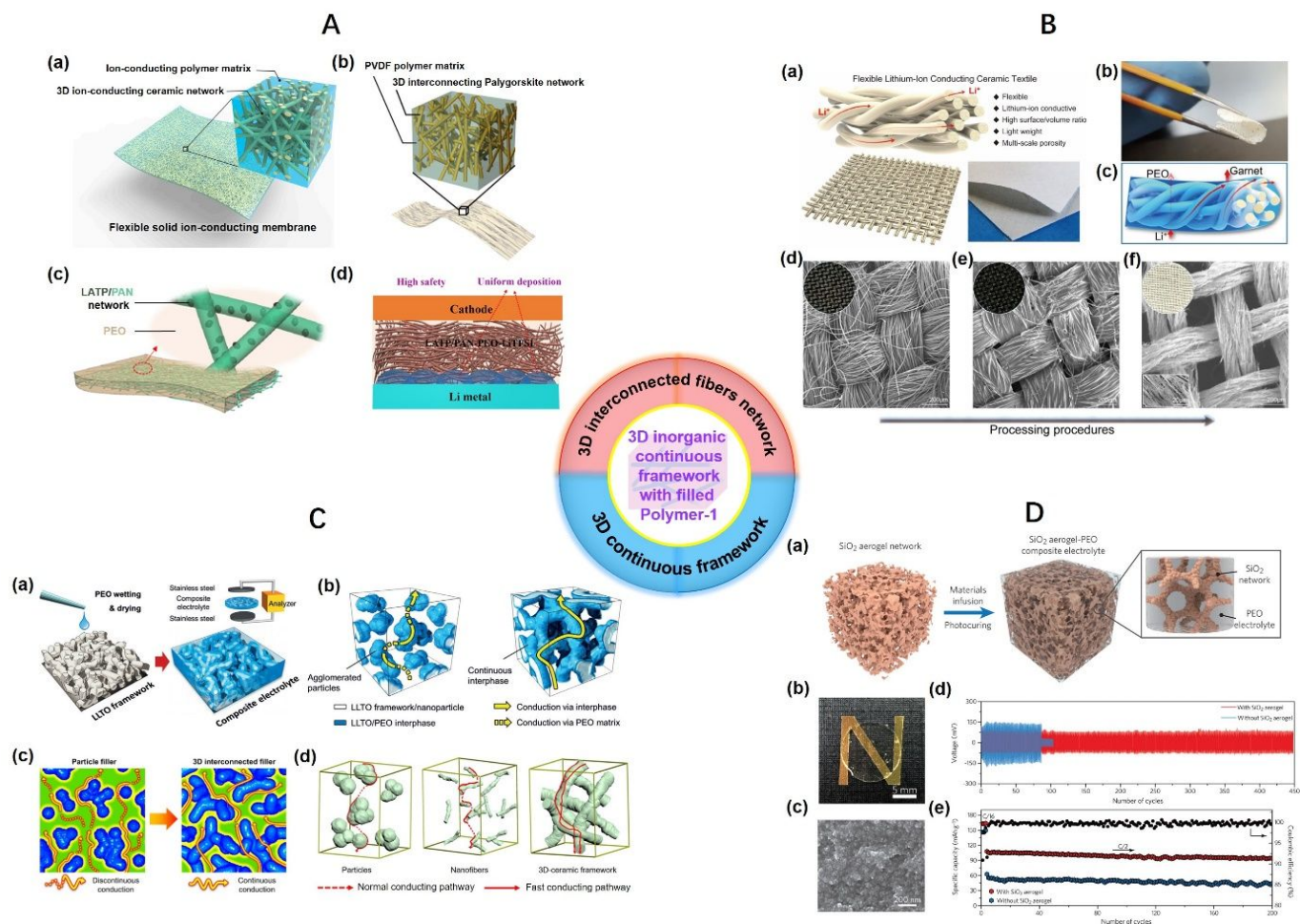


Fig. 11 A. Schematic of the CSSEs of 3D interconnecting fiber filled with polymer. (a) Li_{0.4}La₃Zr₂Al_{0.2}O₁₂ (LLZO) framework in PEO matrix⁸⁹. Reprinted with permission from ref. 89. Copyright 2016, National Academy of Sciences. (b) palygorskite ((Mg,Al)₂Si₄O₁₀(OH)) framework in PVDF matrix³¹⁶. Reprinted with permission from ref. 316. Copyright 2018, American Chemical Society. (c) Li_{1.5}Al_{0.5}Ti_{1.5}(PO₄)₃ (LATP)/PAN fibers network in PAN matrix, (d) proposed lithium plating/stripping processes and lithium surfaces in Li | 2LATP/ PAN-PEO₈/LiTFSI|LiFePO₄.³¹⁷ Reprinted with permission from ref. 317. Copyright 2018, American Chemical Society. **B.** (a) Schematic and optical pictures of the flexible lithium-ion conducting ceramic textile, (b) Dried CSSE with good flexibility and mechanical strength, (c) illustration of the lithium-ion transfer mechanism in CSSE, SEM image of the (d) pretreated textile template, (e) template impregnated with the precursor solution, and (f) the final garnet textile³¹⁸. Reprinted with permission from ref. 318. Copyright 2018, Elsevier Ltd. **C.** Schematics of (a) synthesis process from LLTO 3D framework to CSSE, and its electrochemical analysis, (b) possible ionic transport mechanism in CSSEs with agglomerated nanoparticles (left) and 3D continuous framework (right)³¹³, reprinted with permission from ref. 313. Copyright 2018, Wiley-VCH. (c) Ionic conduction mechanism from discontinuous pathways to 3D continuous pathways (LLZO)³¹⁹, reprinted with permission from ref. 319. Copyright 2018, Elsevier Ltd. (d) ion conducting pathways from nanoparticles to nanowires and 3D interconnected framework (Ga-LLZO)³²⁰. Reprinted with permission from ref. 320. Copyright 2019, American Chemical Society. **D.** Research of 3D SiO₂-aerogel/PEO CSSE. (a) Schematic of the synthesis process for CSSE, (b) optical photograph of the final CSSE film, (c) SEM images showing the surface of the CSSE, (d) symmetric cell cycling with and without 3D SiO₂-aerogel 0.05 mA cm⁻², (e) LFP-Li full cell cycling with and without 3D SiO₂-aerogel at room temperature (≈18°C).³²¹ Reprinted with permission from ref. 321. Copyright 2018, Wiley-VCH.

In addition to the 3D interconnecting nanowires as shown above, there is another more advanced structure, a 3D nano mat (or textile) with regular and better symmetry. To be specific, Chunsheng Wang et al.³²² synthesized the $\text{La}_{0.55}\text{Li}_{0.35}\text{TiO}_3$ (LLTO) electrolyte in the structures from nano fiber into mat (or textile), and then coated an additional very thin PEO layer on their surface to form the CSSEs. In comparison to the dispersed nanofibers or randomly interconnected nanowires, the woven pattern ceramic mat in interdigitated or concentric arrangements with more regular, scalable and better symmetrical structure can provide much better bridging. Thus preferable ionic conductivity (5.0×10^{-4} at RT), better mechanical strength, and even higher transference number (0.7) have been achieved in this regard.

On this basis, Yunhui Gong et al. in Liangbing Hu and/or Eric D. Wachsman's group³¹⁸ recently fabricated a garnet-based ceramic textiles with a chemical composition of $\text{Li}_{6.28}\text{Al}_{0.24}\text{La}_3\text{Zr}_2\text{O}_{11.98}$ (LLZO), which could be used as a solid lithium ion conducting framework and further reinforce polymer electrolyte in the obtained CSSE for stable long time cycling (>500 hours). The structures of the garnet ceramic textiles and its processing procedures are shown in Fig. 11B (a) and (d)-(f), which enables long-range lithium-ion transport pathways via interconnected fibers, high surface area/volume ratio of ceramic ion conductors and multi-level porosity distribution. After combining with PEO as shown in Fig. 11B (b) and (c), more flexibility and higher ionic conductivity can be achieved. Comparing to the ion diffusion through the polymer bulk directly as indicated by the dotted arrow in Fig. 11B (c) or more garnet/polymer interfaces in traditional CSSE with inorganic particles in polymer matrix, there is multi-step process for lithium ions transport in this obtained CSSE. To be specific, the lithium ions first migrate through the PEO at the "bottom" of the "high-speed channel" (LLZO/ ceramic fiber with higher ionic conductivity), then enter and migrate along them until reaching the "top" of the "high-speed channel" as indicated by the solid arrows in Fig. 11B (c). Regarding the electrochemical performance, the ionic conductivity, long-term lithium cycling stability and compatibility have been tested and the results are listed in the Table 5. However, long term full cell tests for this kind of 3D integrated mat/textile reinforced flexible CSSE still need to be further researched to facilitate their actual applications.

3.3.2. 3D continuous framework

Different from the 3D nanofibers normally prepared by electrospinning, the 3D inorganic continuous frameworks in the second main type of the CSSEs are usually synthesized via other chemical methods such as the sol-gel method with subsequent heat-treatment. As shown in Fig. 11C (a), Jiwoong Bae et al.³¹³ prepared a 3D nanostructured hydrogel-derived $\text{Li}_{0.35}\text{La}_{0.55}\text{TiO}_3$ (LLTO) framework through gelation of precursors, decomposition and heat-treatment, and then combining with PEO/LiTFSI to form the final CSSE. The achieved composite electrolyte shows significantly enhanced ionic conductivity (8.8×10^{-5} at RT) and thermal/electrochemical stability. By comparing to the agglomerated nanoparticles as shown in Fig. 11C (b), the authors indicated that these performances enhancement could be attributed to the continuous pathway for lithium ion conduction in the 3D framework. Moreover, Jiwoong Bae et al.³¹⁹ also prepared the same structure with another

type of material, the garnet $\text{Li}_{6.28}\text{La}_3\text{Zr}_2\text{Al}_{0.24}\text{O}_{12}$ (LLZO), similar ion transport mechanism is shown in Fig. 11C (c).

Very recently, another 3D continuous LLZO garnet network was fabricated through a polymeric sponge method, in which a low-cost polyurethane foam was used as the template.³²⁰ The obtained CSSE and the assembled symmetrical/full cells show good performances as listed in the Table 5. The authors also compared the ionic conduction mechanism of CSSE with the inorganic nanoparticles to 3D continuous framework as shown in Fig. 11C (d), and indicated that aside from the continuous fast ionic transport pathways, the high percolation efficiency of 3D garnet network is also an important factor.

In addition to the active garnet or perovskite type 3D inorganic framework which can conduct lithium ions directly, passive materials can also be used as the 3D framework in CSSEs. A recent sample is the 3D SiO_2 -aerogel/PEO CSSE as shown in Fig. 11D (a)-(c), the 3D SiO_2 -aerogel fabricated via sol-gel method is first infused with the mixture of poly(ethylene glycol) diacrylate (PEGDA), succinonitrile (SCN), and LiTFSI, and then photo cured by ultraviolet light for 30 min to form the final CSSE. Although the framework is passive, the cross-linked-PEO electrolyte is about 78 wt.% of the CSSE because of the light weight of SiO_2 -aerogel, thus the good ionic conductivity still can be guaranteed. Moreover, the ionic conductivity can be improved due to the anion (TFSI⁻) adsorption via the uniformly distributed pores of SiO_2 -aerogel with high porosity according to Lewis acid-base interaction, and also due to the dissociation of nitrile- Li^+ interaction in presence of SCN^- . The cycling performances of the corresponding symmetrical/full cells are shown in Fig. 11D (d) and (e), indicating good cycling stability at a wide temperature range.

3.3.3. Vertically aligned 3D framework

Normally, the lithium ion conduction pathways in the first two types of 3D frameworks as summarized above are randomly interconnected. Although the interfacial resistance for ionic transport can be significantly reduced, the random pathways are still long and tortuous. Comparatively speaking, the 3D frameworks with well-aligned pathways can further enhance the ionic migration efficiency. Typically, the researchers in Yi Cui's group^{22,109} compared various ionic conduction mechanisms in various structures from nanoparticles to random nanowires and further the corresponding aligned ones as shown in Fig. 12A, which has been confirmed in their recent works on CSSEs such as PAN/LLTO ($\text{Li}_{0.33}\text{La}_{0.557}\text{TiO}_3$)²² and AAO/PEO¹⁰⁹. The conductivities of the CSSEs with NPs, random NWs, and aligned NWs in various orientations were measured and verified with modelling as shown in Fig. 12A (b)-(d), demonstrating that the fast ion transport on nanowire surfaces without crossing junctions and subsequent enhanced ionic conductivity can be achieved in the CSSE with the aligned NWs along the normal direction of electrode (i.e. 0° orientation). Notably, an astonishing number of $10^{-2} \text{ S cm}^{-1}$ at the interface of aligned ceramic and polymer was given according their research, which is similar to the liquid ionic conductivity.

One method to obtain the aligned 3D framework is to use an anodized aluminum oxide (AAO) template and further fill with polymer as shown in Fig. 12B (a)¹⁰⁹, showing a vertically aligned and continuous ceramic-polymer interfaces. The actual structures of the 3D framework and the final CSSE after filling polymer are shown in Fig. 12B (b) and (c). Furthermore, atomic layer deposition (ALD) of

the strong Lewis acid AlF_3 is also used for modification on the interface of Al_2O_3 and polymer, which can further improve their performance. As a result, the highest ionic conductivity of 5.85×10^{-4}

at RT has been achieved in this composite electrolyte with vertically aligned, and continuous nanoscale ceramic-polymer interfaces, i.e. the fast ionic conduction pathway.

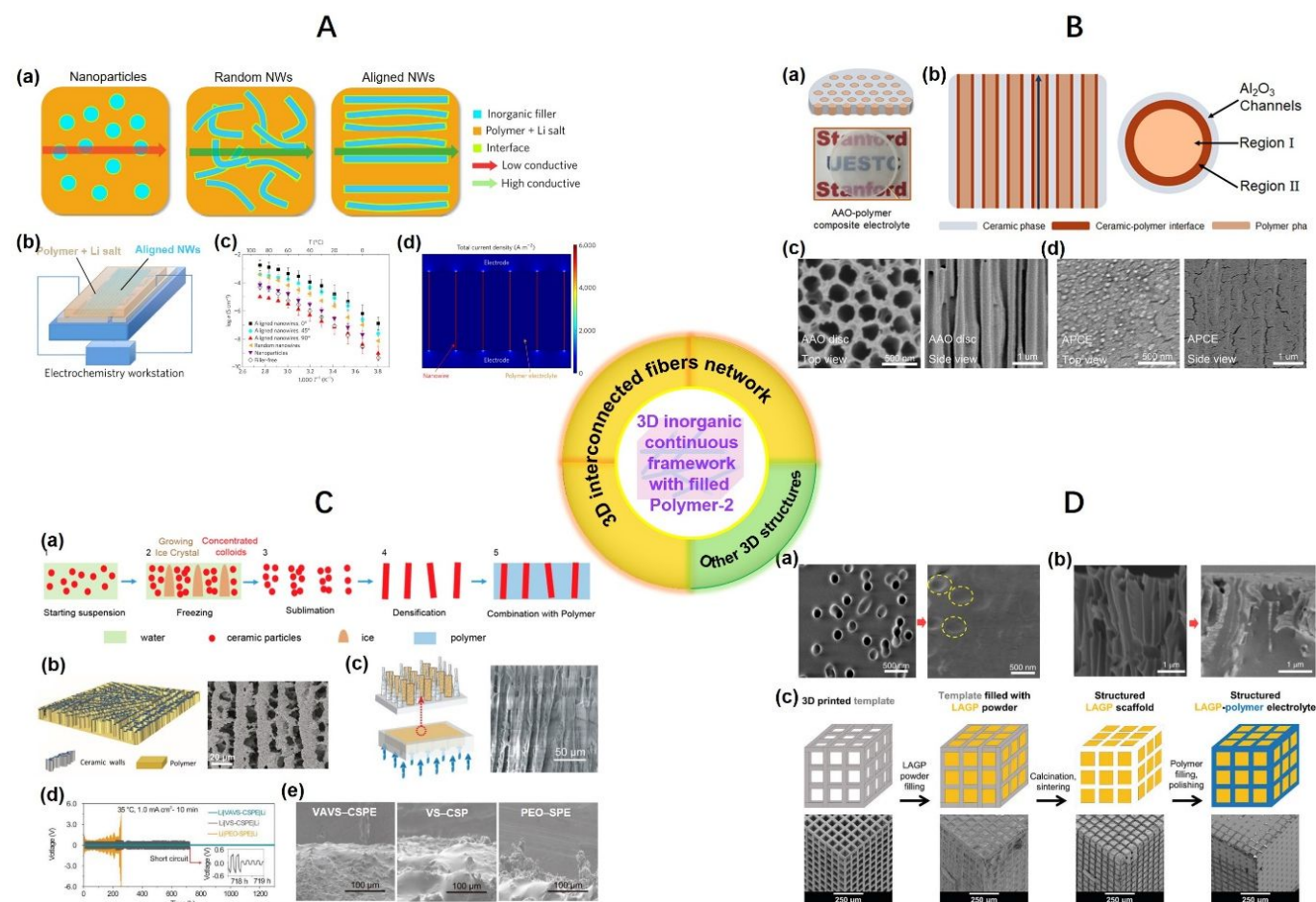


Fig. 12 A (a) Schematics of the CSSEs with nanoparticles (NPs), random nanowires (NWs), and aligned NWs in polymer matrix, (b) electrochemical test for CSSE with aligned NWs, (c) Arrhenius plots of the CSSEs with NPs, random NWs, and aligned NWs in various orientations, (d) Modelling of current densities for the CSSE with aligned NWs in zero-angle orientation.²² Reprinted with permission from ref. 22. Copyright 2017, Nature Publishing Group. B. (a) Schematic and optical image of AAO/PEO CSSE, (b) schematic of the ionic transport pathway and detailed structure in aligned NWs, SEM images of (c) pristine AAO in top (left) and side (right) view,¹⁰⁹ Reprinted with permission from ref. 109. Copyright 2018, American Chemical Society. C. (a) Schematic of the preparation process for the CSSE from ceramic suspensions via freeze-drying method (LAGP/PEO)³⁰, reprinted with permission from ref. 30. Copyright 2017, American Chemical Society. (b) Schematic of the structure of CSSE (LAGP/PEO, left) and the cross-sectional SEM image of 3D LAGP framework²⁶, reprinted with permission from ref. 26. Copyright 2019, Elsevier Ltd. (c) schematic of the structure of 3D vertically aligned 2D sheets, the vermiculite sheets (VS) (left) and the cross-sectional SEM image of the VAVS/PEO CSSE (UV etched, right), (d) cycling performance of Li/CSSE/Li symmetrical cells with VAVS-CSPE (VAVS/PEO-LiTFSI), VS-CSPE (VS/PEO-LiTFSI), and PEO-SPE (PEO-LiTFSI) as solid electrolyte at 35°C, and the corresponding SEM images after half-month test.³²³ Reprinted with permission from ref. 323. Copyright 2019, Wiley-VCH. D. SEM images of porous PI film before (left) and after (right) combining with PEO/LiTFSI from top view (a) and side view (b); Simulation model of Li+ transport in a random system (upper) and z-aligned PEO system (lower)³¹, Reprinted with permission from ref. 31. Copyright 2019, Nature Publishing Group. (c). Schematics and the corresponding SEM images of the synthesis process for cube-LAGP/epoxy CSSE using 3D-print template³²⁴, reprinted with permission from ref. 324. Copyright 2018, Royal Society of Chemistry.

Another effective way to construct the aligned 3D framework is the freeze-drying method (or called as ice-templating-based method). More details can be seen in Fig. 12C (a) from the suspensions with ceramic particles to the final CSSE of LAGP/PEO through freezing, sublimation, densification and combination³⁰. A similar case with the same inorganic materials is shown in Fig. 12C (b), and the interconnected channels, i.e. the ion conduction pathways can be seen clearly²⁶. In addition to the traditional active ceramics or passive metal oxides, the newly developed materials, 2D sheets is also used as

inorganic framework in CSSE. As shown in Fig. 12C (c), one kind of the vertically aligned 2D sheets with continuous channels and large surface area are prepared via freeze-drying method and further combined with PEO to form a novel CSSE (SEM image). Particularly, the Li-Li symmetrical cell with this CSSE is stable over 1300 h with current density of 1.0 mA cm^{-2} at 35°C with a much lower overpotential and no obvious lithium dendrite after comparison (Fig. 12C (d) and (e)). And the corresponding Li-LFP full battery deliver a

very high initial specific capacity of 167 mAh g⁻¹ at 0.1 C at 35°C and 82% capacity retention after 200 cycles at 0.5 C.

In addition to the vertically aligned inorganic/polymer CSSE, a composite polymer/polymer solid electrolyte with similar structure was also proposed by Jiayu Wan et al. in Yi Cui's group³¹. To be specific, an 8.6-μm-thick nanoporous polyimide (PI) film filled with PEO/LiTFSI vertically was reported (Fig. 12D (a) and (b)) and shows very excellent performances including nonflammability, flexibility, mechanically strong, high conductivity, very good long-time cycling, and can also withstand some abuse tests.

3.3.4. Other advanced 3D structures

In short, the CSSEs with vertically aligned inorganic 3D framework and filled polymer (contained lithium salt) provide a good orientation and much shorter pathway for lithium ions transportation. On these bases, some other more advanced structures can provide more orientations with short ionic conduction pathways³²⁴. As shown in Fig. 12 D(c), the 3D bicontinuous ceramic and polymer microchannels can be achieved in this advanced structure, not just the vertically z orientation introduced above, the lithium ions can transport linearly in any of all the x, y and z orientation according to the electric field direction.

3.4. Open-framework related composite electrolytes

3.4.1. Metal-organic frameworks (MOFs)

Metal-organic frameworks, namely MOFs, are one type of crystalline materials composed of metal ions and their linked organic ligands, which is widely investigated in various areas ranging from gas storage, to drug delivery, and to sensing due to their special features such as ultrahigh porosity (reach 90% free volume) and enormous internal surface areas (up to 6000 m²/g) etc.³²⁵⁻³³². Aside from the conventional applications, MOFs have recently emerged as a class of precursors or functional materials for electrochemical energy storages and conversion technologies, including electrode materials for batteries or capacitors, efficient electro catalysts, and even electrolytes for electrochemical devices³³³.

With regards to the CSSEs for lithium batteries, we divided them into two main categories including (1) all solid state electrolytes consisting of MOF fillers and polymer matrix with lithium salts³³⁴⁻³³⁹, and (2) the so-called "solid state electrolyte", "pseudo solid state electrolyte" or "solid-like electrolyte", is composed of MOF or MOF related materials and a small amount of additives such as liquid electrolytes³⁴⁰, lithium salts and/or organic solvents³⁴¹⁻³⁴³, or ionic liquids³⁴⁴⁻³⁴⁷ to deal with the low conductivity nature of MOFs materials, which are also regarded as gel electrolytes or half solid state electrolyte. Strictly speaking, only the former can be regarded as the CSSEs, for better understanding of the overall MOF-related composite electrolytes, researches in the latter situation have also been summarized and introduced here. All those electrolytes are showed in Table 6 below.

A case of the former is the nano MOF-5 fillers in PEO/LiTFSI based polymer matrixs³³⁴, which showed the highest ionic conductivity of 3.16 × 10⁻⁵ s cm⁻¹ at 25°C and four times higher than that without MOF-5 filling. Besides, the LiFePO₄/Li cells with MOF-5/PEO/LiTFSI SSE also has much better cycling performance at 1C rate at 80°C. Further, Hanyu Huo et al.³³⁵ proposed a novel cationic

metal-organic framework (CMOF), cationic D-Uio-66-NH₂ (Uio-66, ([Zr₆O₄(OH)₄(BDC)₆] as shown in Fig. 13, in which BDC²⁻ is 1,4-benzenedicarboxylic acid radical)) to immobilize anions and optimize Li⁺ distribution to unfavour lithium dendriteic growth, in which the MOF materials was grafted with -NH₂ group to protect the -O- (ether oxygen) in the polymer chains via hydrogen bonds. Thus the electrochemical window of CMOF/PEO/LiTFSI based system can be further extended to 4.97 V. Similar studies have also been investigated and the key MOF related materials such as Mg-TPA³⁴⁸ or Al-TPA-MOF³⁴⁹, and the components of CSSE are listed in the Table 6.

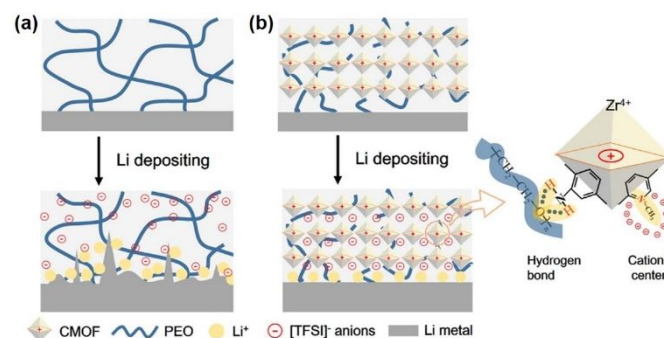


Fig. 13 Schematic of the Li deposition behavior with (a) PEO(LiTFSI) electrolyte and (b) anion-immobilized P@CMOF electrolyte³³⁵. Reprinted with permission from ref. 335. Copyright 2019, Elsevier Ltd.

Moreover, aside from simply physically blending with the polymers, some researchers tried to chemically linked the MOF particles with some typical polymeric matrices to further improve their compatibility and comprehensive electrochemical performances. Z. Wang et al.³³⁶ used one-pot UV photopolymerization to prepare a flexible CSSE, in which the MOF (Uio-66-NH₂) was first decorated with carbon-carbon double bonds (C=C) through postsynthetic modification into M-Uio-66-NH₂ (namely the Uio-66-NH₂ modified by methacryloyl chloride), then covalently linked to polymer (PEGDA, poly(ethylene glycol) diacrylate) chains under UV light. It is confirmed that the obtained CSSE show over 5 times higher ionic conductivity and also exhibits better contact with lithium electrode than that of the SSE without MOF related materials.

When it comes the latter, namely the so-called "solid state electrolyte", "pseudo solid state electrolyte", or "solid-like electrolyte" with addition of liquid electrolytes, or lithium salts and organic solvent, or ionic liquids, there are also some recent researches which have about 10 times higher ionic conductivities than of the former. For instance, B. M. Wiers et al.³⁴¹ proposed a new solid lithium electrolyte, as shown in Fig. 14 (a), Mg₂(dobdc)·0.35LiO·Pr·0.25LiBF₄·EC·DEC (dobdc⁴⁻ is 1,4-dioxido-2,5-benzenedicarboxylate; EC and DEC are ethylene carbonate and diethyl carbonate, respectively), in which the MOFs materials, Mg₂(dobdc) was grafted by LiO·Pr (isopropoxide), thus leading a higher ionic conductivity of 3.1 × 10⁻⁴ s cm⁻¹ at 300 K.

ARTICLE

Journal Name

Table 5 Typical inactive metal oxides as fillers in polymer based CSSEs

	3D structures	Filled polymer	σ (S cm ⁻¹)	Li CSSE Li (stable cycling)	Li CSSE Cathode (performance)	Ref.
3D interconnectin g fiber	Li _{0.4} La _{0.3} Zr _{0.2} Al _{0.2} O ₁₂ (LLZO)	PEO/LiTFSI	2.5 × 10 ⁻⁴ at RT	Block dendrites at 0.2 mA cm ⁻² for 500 h, or 0.5 mA cm ⁻² for 300 h at RT		89
	Li _{0.33} La _{0.557} TiO ₃ (LLTO)	PVDF/LiTFSI	1.8 × 10 ⁻⁴ at RT	0.1 mA cm ⁻² for over 800 h at RT		315
	Li _{1.5} Al _{0.5} Ti _{1.5} (PO ₄) ₃ (LATP)	PVDF/LiClO ₄	1.2 × 10 ⁻⁴ at RT	0.15 mA cm ⁻² for over 60 h at RT	Li CSSE NMC111, 121.4 mAh ⁻¹ at C/3 and steady cycling over 200 cycles at RT	316
Mat/textile	Li _{1.4} Al _{0.4} Ti _{1.6} (PO ₄) ₃ (LATP)/PAN	PEO ₈ /LiTFSI	6.5 × 10 ⁻⁴ at 60°C, 5.0 × 10 ⁻⁵ at 25°C	0.3 mA cm ⁻² for over 400 h at 60°C	Li CSSE LFP, 144 mA h g ⁻¹ at 0.2C initially, 99.5% (CE) over 100 cycles at 60°C	317
	La _{0.55} Li _{0.35} TiO ₃ (LLTO)	PEO/LiN(SO ₂ CF ₃) ₂	5.0 × 10 ⁻⁴ at RT	No interfacial reaction between LLTO and Li metal anode during > 600 h running		322
	Li ₇ La ₃ Zr ₂ O ₁₂ (LLZO)	PEO/LiTFSI	1.8 × 10 ⁻⁴ at 60°C, 2.7 × 10 ⁻⁵ at 25°C	0.05 to 0.2 mA cm ⁻² for over 500 h at 60°C, over potentials from 15 to 47 mV.		318
3D continuous network	Li _{0.35} La _{0.55} TiO ₃ (LLTO)	PEO/LiTFSI	8.8 × 10 ⁻⁵ at RT	0.05 mA cm ⁻² for 100 h at 25°C, 0.1 mA cm ⁻² for 100 h at 50°C.		313
	Li _{0.28} La _{0.4} Zr _{0.24} Al _{0.24} O ₁₂ (LLZO)	PEO/LiTFSI	8.5 × 10 ⁻⁵ at 25°C ~10 ⁻³ at 60°C	0.05 mA cm ⁻² for 150 cycles at 25°C.	Li CSSE LFP, 158, 145, 132, and 101 mAh g ⁻¹ at 0.1C, 0.5C, 1C and 2C at 60°C	319
	Ga-LLZO	PEO/LiTFSI	1.2 × 10 ⁻⁴ at 30°C	0.4 mA cm ⁻² for 360 h at 60°C.	Li CSSE LFP, 138 mA h g ⁻¹ at the first cycle, with 92.4% retention after 50 cycles (128 mA h g ⁻¹) at 0.5 C at 60°C	320
	SiO ₂ aerogel	PEO/LiTFSI	~6 × 10 ⁻⁴ at 30°C	0.05 mA cm ⁻² for 450 cycles at 18°C	Li CSSE LFP, stable cycling for at least 200 cycles at 0.5C at 18°C; At 0.4 C, 105 mAh g ⁻¹ at 15°C and 105 mAh g ⁻¹ at 35°C.	321
Vertically aligned 3D framework	Li _{0.33} La _{0.557} TiO ₃ (LLTO)	PAN/LiClO ₄	6.05 × 10 ⁻⁵ at 30°C 1.26 × 10 ⁻² at 30°C (deduced value)			22
	AAO	PEO/LiTFSI	5.85 × 10 ⁻⁴ at RT	0.75 mA cm ⁻² for more than 400 h at RT with over potential of 40 mV		109
	AAO	PEO/LiSO ₃ CF ₃	~10 ⁻⁴ at RT			314
	Li _{1+x} Al _x Ti _{2-x} (PO ₄) ₃ (LATP)	PEO-PEG/LiClO ₄	5.2 × 10 ⁻⁵ at RT			30
	Li _{1.5} Al _{0.5} Ge _{1.5} (PO ₄) ₃ (LAGP)	PEO/LiTFSI	1.67 × 10 ⁻⁴ at RT and 1.11 × 10 ⁻³ at 60°C	0.1 mA cm ⁻² for 200 h at 60°C with over potential of 0.17 V.	Li CSSE LFP, initial specific capacity is 148.7 mAh g ⁻¹ at 0.3 C at 60°C, a capacity retention of 93.3% (138.8 mAh g ⁻¹) after 300 cycles	26
	Vermiculite sheets (VS)	PEO/LiTFSI	1.89 × 10 ⁻⁴ at 25°C	1.0 mA cm ⁻² for 1300 h running at 35°C without fluctuation of overpotential	Li CSSE LFP, 167 mAh g ⁻¹ at 0.1C at 35°C, 82% capacity retention after 200 cycles at 0.5 C.	323
	polyimide (PI)	PEO/LiTFSI	2.3 × 10 ⁻⁴ at 30°C	0.1 mA cm ⁻² for 1,000 h at 60°C with over potential less than 0.10 V.	Li CSSE LFP, 176 mAh g ⁻¹ at 0.1 C, 176 mAh g ⁻¹ at 0.1 C at 60°C, stable cycling for more than 200 at 0.5C rate at 60°C.	31
	Li _{1.4} Al _{0.4} Ge _{1.6} (PO ₄) ₃ (LAGP)	epoxy	1.6 × 10 ⁻⁴ at RT			324

* EW, electrochemical stability window; NMC111, Li(Ni_{1/3}Mn_{1/3}Co_{1/3})O₂; PAN, polyacrylonitrile; CE, columbic efficiency; AAO, anodic aluminum oxide;

Recently, Sarah S. Park *et al.*³⁴² proposed a novel MOFs material, MIT-20 (MIT, Massachusetts Institute of Technology; $(\text{CH}_3)_2\text{NH}_2$ $[\text{Cu}_2\text{Cl}_3\text{BTDD}] \cdot (\text{DMF})_4(\text{H}_2\text{O})_{4.5}$; BTDD²⁻, bis(1,2,3-triazolo[4,5-*b*],[4',5'-*i*])dibenzo-[1,4]dioxin; DMF, N,N-dimethylformamide), which is composed of alternate pairs of Cu atoms connected with either by a μ_2 -Cl and two BTDD²⁻ ligands, or two BTDD²⁻ ligands. Moreover, the DMACl (dimethylammonium Cl) can be removed in MIT-20 to form neutral MIT-20d ($\text{Cu}_2\text{Cl}_2\text{BTDD}$) as shown in Fig. 14 (b), which could further react with stoichiometric amounts of halide or pseudohalide salts (LiCl, LiBr, NaSCN, MgBr₂, or LiBF₄) in dry tetrahydrofuran (THF), thus the MIT-20-LiCl ($\text{Li}[\text{Cu}_2\text{Cl}_3\text{BTDD}] \cdot 10(\text{PC})$), MIT-20-LiBr ($\text{Li}_{0.8}[\text{Cu}_2\text{Cl}_2\text{Br}_{0.8}\text{BTDD}] \cdot 10(\text{PC})$), MIT-20-Na ($\text{Na}[\text{Cu}_2\text{Cl}_2(\text{SCN})\text{BTDD}] \cdot 9(\text{PC})$), MIT-20-Mg ($\text{Mg}_{0.5}[\text{Cu}_2\text{Cl}_2\text{BrBTDD}] \cdot 8(\text{PC})$), and MIT-20-LiBF₄ ($\text{Li}_{0.9}[\text{Cu}_2\text{Cl}_2\text{Br}_{0.9}\text{BTDD}] \cdot 0.3\text{LiBF}_4 \cdot 9(\text{PC})$) were obtained after exchange of residual THF with propylene carbonate (PC). Those materials show ionic conductivities of 1.3×10^{-5} , 4.4×10^{-5} , 1.8×10^{-5} , 8.8×10^{-7} , and even 4.8×10^{-5} S cm⁻¹, respectively.

Furthermore, Li Shen *et al.*³⁴⁰ prepared a series of LiClO₄-propylene carbonate solution (LPC) soaked MOF materials including MIL-100-M ($(\text{M}_3\text{O}(\text{BTC})_2\text{OH} \cdot (\text{H}_2\text{O})_2$, M = Al, Cr, Fe), BTC is benzene-1,3,5-tricarboxylate, C₉H₃O₆), UiO-66 ($\text{Zr}_6\text{O}_4(\text{OH})_4(\text{BDC})_6$, BDC = 1,4-dicarboxylate), UiO-67 ($\text{Zr}_6\text{O}_4(\text{OH})_4(\text{BPDC})_6$, BPDC = biphenyl-4,4'-dicarboxylate) and HKUST-1 ($\text{Cu}_3(\text{BTC})_2$). After filtration and removal of any excessive solvent, those powders were pressed into electrolyte pellets and their ionic conductivities were measured, which presented ionic conductivities from 0.18 to 1.22

mS·cm⁻¹. On this basis, the authors indicated that the biomimetic ionic channels in MOF related materials were involved in Li⁺ transport by complexing electrolyte anions (e.g. ClO₄⁻) to the OMSs (open metal sites) within the channels filled with solvent molecules, as shown in Fig. 14 (c).

Aside from liquid electrolytes, ionic liquids are also added into MOFs materials as part of the electrolytes. One typical case in the addition of ionic electrolyte is the solid-like electrolyte of Li-IL@MOF (Fig. 14 (d)), in which the interfaces of MOF particles are nanowetted by LiTFSI-[EMIM][TFSI] to favor the Li⁺ transport kinetics, and the obtained battery shows remarkable performance over a very wide temperature range (-20 to 150°C)³⁵⁰. Very recently, Songyan Bai and co-workers³⁵¹ presented a strategy of MOF (HKUST-1) modified electrolyte for achieving selective ion transport via actual experiments, density functional theory (DFT) calculations, and molecular dynamics (MD) simulations as shown in Fig. 15, in which the “caged” electrolyte anions (TFSI) in MOF’s angstrom-scale pores could facilitate a homogeneous Li ion flux. As a result, the obtained MOF-modified electrolyte delivered a stable performance over 2000 cycles at 5C with a much higher current density of about 7 mA cm⁻².

In addition to the above two main categories, some researchers combined all of the polymer (e.g. PEO) with lithium salts, ionic liquid, and MOF materials to form the corresponding electrolytes³⁴⁵, more details about the composition and their ionic performance can be seen in Table 6.

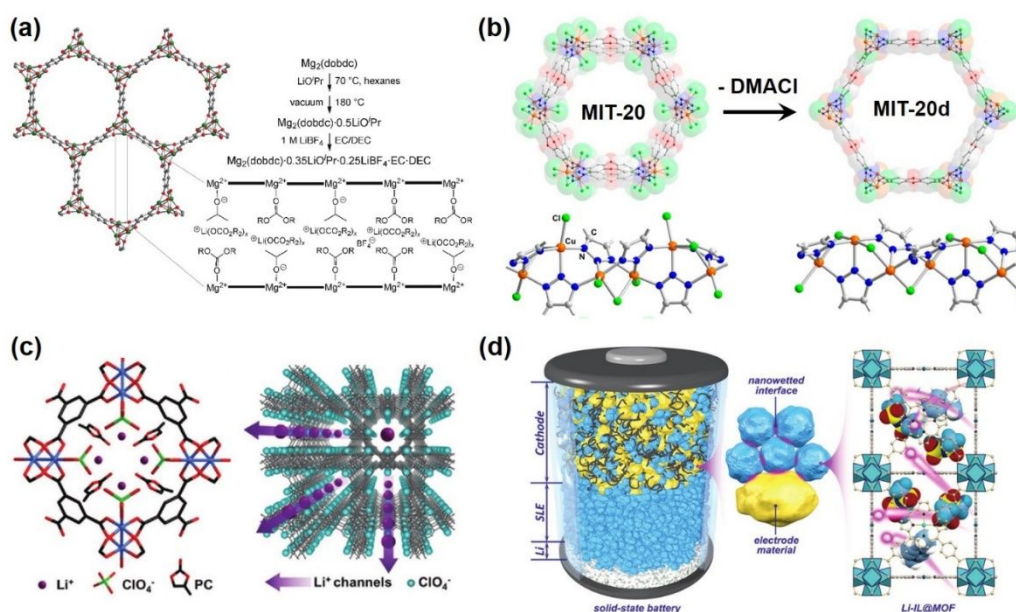


Fig. 14 Examples of some “solid-like electrolytes”. (a) Structure of $\text{Mg}_2(\text{dobdc})$ and the its modification process to form the final solid electrolyte³⁴¹, reprinted with permission from ref. 341. Copyright 2011, American Chemical Society. (b) Structures of MIT-20 to MIT-20d³⁴², reprinted with permission from ref. 342. Copyright 2017, American Chemical Society. (c) formation of biomimetic ionic channels in HKUST-1 (left) and typical 3D-MOF scaffold with ClO_4^- anions and Li^+ ions³⁴⁰, reprinted with permission from ref. 340. Copyright 2018, Wiley-VCH. (d) the architecture of the solid-state battery with the nanowetted MOFs³⁵⁰, reprinted with permission from ref. 350. Copyright 2018, Wiley-VCH.

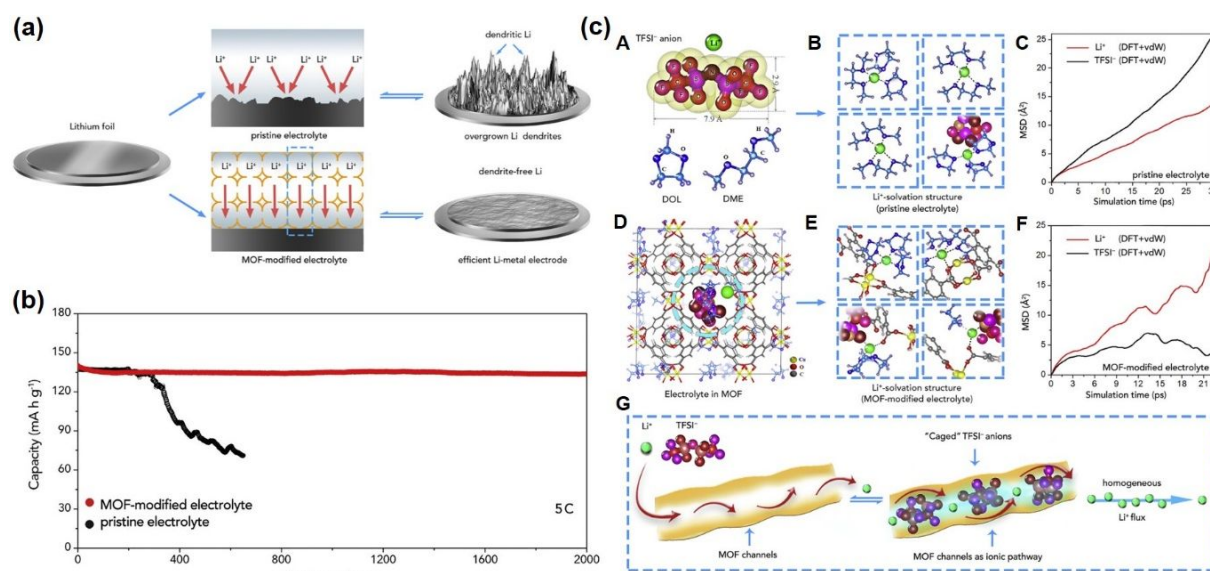


Fig. 15 (a) Schematic illustration of the dendritic Li growth with pristine electrolyte (upper, overgrown Li dendrites) and MOF-modified electrolyte (lower, uniform Li growth); (b) Electrochemical performance of full batteries with pristine electrolyte and MOF-modified electrolyte; (c) MD simulation for the molecular/crystal structures in electrolyte, which includes the structures of LiTFSI and organic solvent (DOL is 1,3-dioxacyclopentane and DME is 1,2-dimethoxyethane) (A), electrolyte in MOF (D), Li⁺-solvation structure in pristine electrolyte (B) and MOF-modified electrolyte (E), Calculated mean square displacement (MSD) of Li⁺ and TFSI⁻ ions with simulation time in pristine electrolyte (C) and MOF-modified electrolyte (F), and the schematic of Li⁺ ionic transport in MOF channels (G) ³⁵¹, reprinted with permission from ref. 351. Copyright 2018, Elsevier Ltd.

Table 6 MOF-derived composite electrolytes

Fillers (NP)/MOFs	Composite electrolytes	σ (S cm ⁻¹)	Enhancement (vs. MOFs-free)	Ref.
10wt.% MOF-5	MOF-5/PEO/LiTFSI	3.16×10^{-5} (25°C)	7.36×10^{-6} (25°C)	334
12.5 vol.% CMOF (D-UiO-66-NH ₂)	CMOF/PEO/LiTFSI	3.1×10^{-5} (25°C), 6.3×10^{-4} (60°C)	3.9×10^{-6} (25°C)	335
M-UiO-66-NH ₂	CMOF/PEGDA/LiTFSI	4.31×10^{-5} (30°C)	$\sim 8.0 \times 10^{-6}$ (30°C)	336
10 wt.% Mg-TPA	Mg-TPA/PEO/LiTFSI	$\sim 2.0 \times 10^{-5}$ (25°C)	$\sim 8.0 \times 10^{-6}$ (25°C)	348
10 wt.% Mg-BTC MOF	Mg-BTC MOF/PEO/LiTFSI	$\sim 1.0 \times 10^{-4}$ (30°C)	$\sim 1.0 \times 10^{-7}$ (30°C)	338
10 wt.% Al-BTC MOF	Al-BTC MOF/PEO/LiTFSI	$\sim 1.0 \times 10^{-5}$ (30°C)	$\sim 1.0 \times 10^{-7}$ (30°C)	337
15 wt.% Al-TPA-MOF	Al-TPA-MOF/PEO/LiTFSI	$\sim 7.0 \times 10^{-5}$ (30°C)	$\sim 4.0 \times 10^{-7}$ (30°C)	349
Mg ₂ (dobdc)	Mg ₂ (dobdc)·0.35LiO ⁺ Pr·0.25LiBF ₄ ·EC·DEC	3.1×10^{-4} (27°C)	--	341
LiOtBu-grafted UiO-66	LiOtBu-grafted UiO-66/PC	1.8×10^{-5} (25°C)	--	343
	LiOtBu-grafted UiO-66/ LiBF ₄ /PC	$\sim 1.8 \times 10^{-3}$ (25°C)	--	343
MIT-20d	MIT-20d/LiBF ₄ /PC	4.8×10^{-4} (25°C)	--	342
HKUST-1	HKUST-1/LiClO ₄ /PC	3.8×10^{-4} (25°C)	--	340
UiO-66	UiO-66/LiTFSI/[EMIM] [TFSI]	3.2×10^{-4} (25°C)	--	344
MOF-525(Cu)	MOF-525(Cu)/LiTFSI/[EMIM] [TFSI]	3.0×10^{-4} (25°C)	--	350
MIL-101(Cr)	MIL-101(Cr)/[Emim][SCN]	1.15×10^{-3} (25°C)	--	346
	MIL-101(Cr)/[Emim][DCA]	4.14×10^{-4} (25°C)	--	346
UiO-66	UiO-66/PEO/LiTFSI/[EMIM] [TFSI]	1.3×10^{-4} (30°C)	3.2×10^{-6} (30°C)	345

*Mg₂(dobdc), (dobdc⁴⁻ is 1,4-dioxido-2,5-benzenedicarboxylate); EC = ethylene carbonate; DEC = diethyl carbonate; ⁱPr, isopropylborate; UiO-66, ([Zr₆O₄(OH)₄(BDC)₆]_n, in which BDC²⁻ is 1,4-benzenedicarboxylic acid radical); MOF-5, Zn₄O(1,4-benzenedicarboxylate)₃; [EMIM] [TFSI], 1-ethyl-3-methylimidazolium bis[(trifluoromethyl)sulfonyl]imide; CMOF, cationic metal-organic framework (CMOF); Mg-TMA, magnesium-1,3,5-benzene tricarboxylic acid; Mg-TPA, Magnesium-1,4-benzenedicarboxylic acid; [Emim][SCN], 1-ethyl-3-methylimidazolium thiocyanate; [Emim][DCA], 1-ethyl-3-methylimidazolium dicyanamide; PEGDA, poly(ethylene glycol) diacrylate; Al-TPA-MOF, aluminium terephthalate metal organic framework; PC, propylene carbonate; MOF-525(Cu), Zr(IV)₅O₄(OH)₄(CuTCPP)₃, here CuTCPP is [5,10,15,20-tetrakis(4-carboxyphenyl)porphyrin]Cu(II); BTC, 1,3,5-benzenetricarboxylate; MIT-20d, M2Cl2BTDD (M = Mn, Co, Ni); LiOtBu, Lithium tert-Butoxide;

3.4.2. Covalent organic frameworks (COFs)

Similar to MOF materials, another novel class of crystalline materials, covalent organic frameworks (COFs), have also been exposed as components to construct CSSEs. Similarly, the COFs-related solid state electrolytes can also be divided into the “real solid-state electrolytes” and the “solid-like electrolytes”. Although this review is mainly focused on the true CSSEs, to help readers to grasp a better understand for COFs used in lithium batteries, those two aspects are included, more details can be seen below.

First, the COFs related electrolytes with organic solvent are regarded as “solid-like electrolytes”, most of the liquids are trapped in the pores of COFs materials, therefore the safety issues from flammable liquids can be alleviated but not fully resolved. The initial studies of COFs-related electrolytes usually immerse the COFs with specific channels into the solution of lithium salt in organic solvents. For instance, Jun Heuk Park and co-workers³⁵² reported a new type of solid lithium-ion conducting electrolytes, which is made by incorporation of Li⁺ ions into a cucurbit[6]uril (CB[6])-based organic molecular porous solid. The honeycomb-like 1D channels along the

c-axis provide an excellent ion transport pathway, which grants a high Li⁺ ion conductivity of 10⁻⁴ S cm⁻¹ and Li⁺ transference number of 0.7-0.8.

Moreover, another case was investigated by Demetrius A. et al.³⁵³, who proposed five 2D COFs with different functionalities (e.g. boronate, boroxine, β-ketoenamine and triazine) and symmetries (hexagonal and tetragonal). Those samples were mechanically pressed into shaped objects with anisotropic ordering in preferred orientation and further impregnated in 1 M LiClO₄/THF, which enable them to display fast Li-ion conductivity and high electrochemical stability, implying their possible applications for CSSEs in rechargeable Li-ion batteries. Based on this COFs-related electrolyte system composed of COF-5 (C₉H₄BO₂), LiClO₄, and THF, a specific study about dynamics and microstructural evolution during Li⁺ ion diffusion is developed using ab initio molecular dynamics simulation³⁵⁴. It is found that, as driven by facile rotation and short-range diffusion of the anions ClO₄⁻ and the organic solvent THF, the diffusion of Li⁺ ion shows a one-dimensional liquid-like behavior.

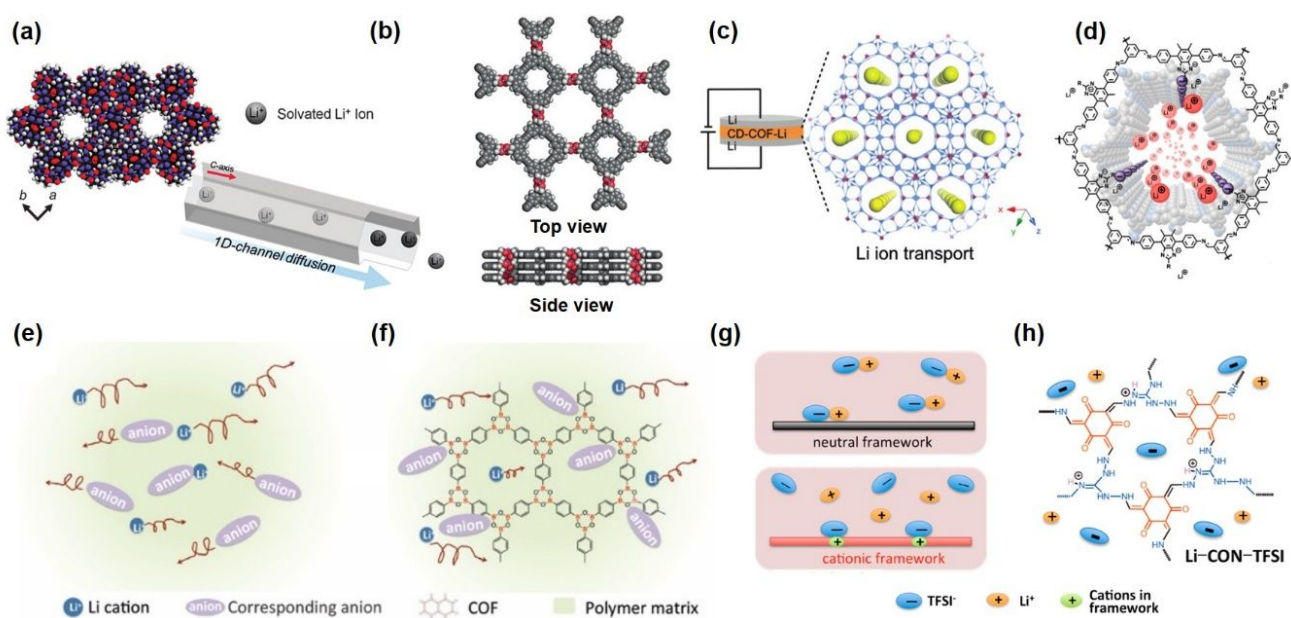


Fig. 16 (a) Porous CB[6]-based solid lithium electrolyte with 1-D channels for Li ion transport³⁵². Reprinted with permission from ref. 352. Copyright 2015, Royal Society of Chemistry. Schematic representations of (b) top and side view of proposed structural of ICOF-2355, reprinted with permission from ref. 355. Copyright 2016, Wiley-VCH. (c) Li ion transport in the channels of CD-COF-Li³⁵⁶, reprinted with permission from ref. 356. Copyright 2016, Wiley-VCH. (d) imidazolite-based ionic COFs with high Li ion conductive channels³⁵⁷. Reprinted with permission from ref. 357. Copyright 2019, American Chemical Society. Schematic diagram of the SPEs without (e) or with (f) COF additives,³⁵⁸ reprinted with permission from ref. 358. Copyright 2019, Royal Society of Chemistry. (g) Schematic illustrations of ion association in COFs with neutral and cationic frameworks, respectively. (h) Synthetic scheme of the CONs with cationic framework for Li⁺ conduction.³⁵⁹ Reprinted with permission from ref. 359. Copyright 2019, American Chemical Society.

Second, aside from immersing the COFs into organic solvent/lithium salt directly, some other researches modified the COFs with ionic linkages first to form the immobilized ion centres, thus the conductivity and stability of obtained electrolytes can be improved. For example, Ya Du *et al.*³⁵⁵ proposed a novel type of ionic covalent organic framework (ICOF) material as shown in Fig. 16 (b), which is constructed by spiroborate linkage and contains sp³ hybridized boron anionic centres and tunable counteranions. Here the

Li⁺ is incorporated into COFs as functional group during material synthetic process, only the binder (PVDF) and organic solvent (PC) are added to form the final electrolyte membrane. Due to the presence of the immobilized ion centers in ICOF, it exhibits a room-temperature conductivity of 3.05 x 10⁻⁵ S cm⁻¹ and an average transference number of around 0.8.

Meanwhile, the basic structure of COFs is also an important factor to influence the performance of electrolyte such as the

comparison between 2D and 3D COFs, in 2D COFs, the building blocks are linked by strong covalent bonds and restrained in 2D polymeric layers, then the non-covalent interactions can make those layers stack to form eclipsed or staggered structures. While in 3D COFs, the structural units are usually extended into three-dimensional space through tetrahedral linkages^{356,360}. By comparison, there are some advantages for 3D COFs including high porosity, low density, and well-defined structures, but the difficult choice between building blocks and synthetic process limit their further development.

In this regard, a 3D CD (cyclodextrin)-COF was designed and synthesized using γ -cyclodextrin (γ -CD) as the aliphatic and flexible building block, and tetrakis(spiroborate) as a covalently tetrahedral linkage through a facile microwave-assisted method (Fig. 16 (c))³⁵⁶. After incorporating Li^+ as the counterion, the obtained 3D anionic COF (CD-COF-Li) with well-defined channels can act as reservoirs for liquid electrolytes and serve as solid-state electrolytes for lithium battery, which delivers an ionic conductivity of $2.7 \times 10^{-3} \text{ S cm}^{-1}$ at 30°C . This good performance can be ascribed to the flexible and dynamic nature of CD, the anionic feature of the network derived from spiroborate, and high capability confined channels.

Similarly, a series of crystalline imidazolate-based ionic COFs including H-ImCOF ($(\text{C}_{27}\text{H}_{20}\text{N}_4)_n$), H-Li-ImCOF ($(\text{C}_{27}\text{H}_{19}\text{N}_4\text{Li})_n$), CH_3 -Li-ImCOF ($(\text{C}_{28}\text{H}_{21}\text{N}_4\text{Li})_n$), CF_3 -Li-Im-COF ($(\text{C}_{28}\text{H}_{18}\text{N}_4\text{F}_3\text{Li})_n$) have been reported as SSEs³⁵⁷. Their typical structure is shown in Fig. 16 (d), where the lithium ions can freely transport through the intrinsic channels in the presence of organic solvent. Due to the weak Li ion and imidazolate binding interactions, and well-defined porous framework, these ionic COFs exhibit outstanding ion conductivity and high transference number as listed in Table 7.

In addition, polymers can also be combined with COFs and then immersed in lithium/organic solvent solution to form the gel

electrolyte membrane. As shown in Fig. 16 (e) and (f), a porous boron-containing COFs, $(\text{C}_3\text{H}_2\text{BO})_6(\text{C}_9\text{H}_{12})_1$, was synthesized and employed as functional additives into the polymer (PVDF) matrix to form a composite electrolyte, which has an enhanced ionic conductivity and higher lithium transference number. However, this prepared polymer composite electrolytes still need to immerse into liquid electrolyte solution to form the gel electrolytes before cell assembly³⁵⁸.

Third, in addition to acting as reservoirs for liquid electrolytes, the anionic COFs can also conduct Li^+ ions in the absence of any solvent, which can be called as a “true solid state electrolyte”. Hongwei Chen and co-workers³⁵⁹ incorporated cationic skeleton into the COF structure to form a 2D COF nanosheet (CON), which is named as Li-CON-TFSI and shown in Fig. 16 (g) and (h). Compared to the COFs with neutral frameworks, the obtained cationic COFs separate the Li salt ion pair (Li^+ and TFSI $^-$) through stronger dielectric screening, leading to significantly improved ionic conductivity of $2.09 \times 10^{-4} \text{ S cm}^{-1}$ at 70°C without any organic solvent.

In addition to the anionic COF, some other similar anionic, neutral, and cationic COFs incorporated with a low-molecular-weight polyethylene glycol (PEG, $M_w=800$) are also proposed as shown in the Fig. 17 below³⁶¹. Here the PEG chains confined in the well-aligned channels act as a transport medium and exhibit high Li^+ solvating ability and flexibility. As an example, the ion conductivity of PEG- $\text{Li}^+@$ EB-COF- ClO_4^- (EB, ethidium bromide) without any solvents reaches $1.78 \times 10^{-3} \text{ S cm}^{-1}$ at 120°C , which is very high in all polymeric crystalline porous materials based CSSE in absence of any solvents. By comparison, the anionic or cationic COFs show much better conductivity than neutral ones, which is on account of the dissociation of ionic pairs which will be promoted by the interactions of Li salt and the charged framework.

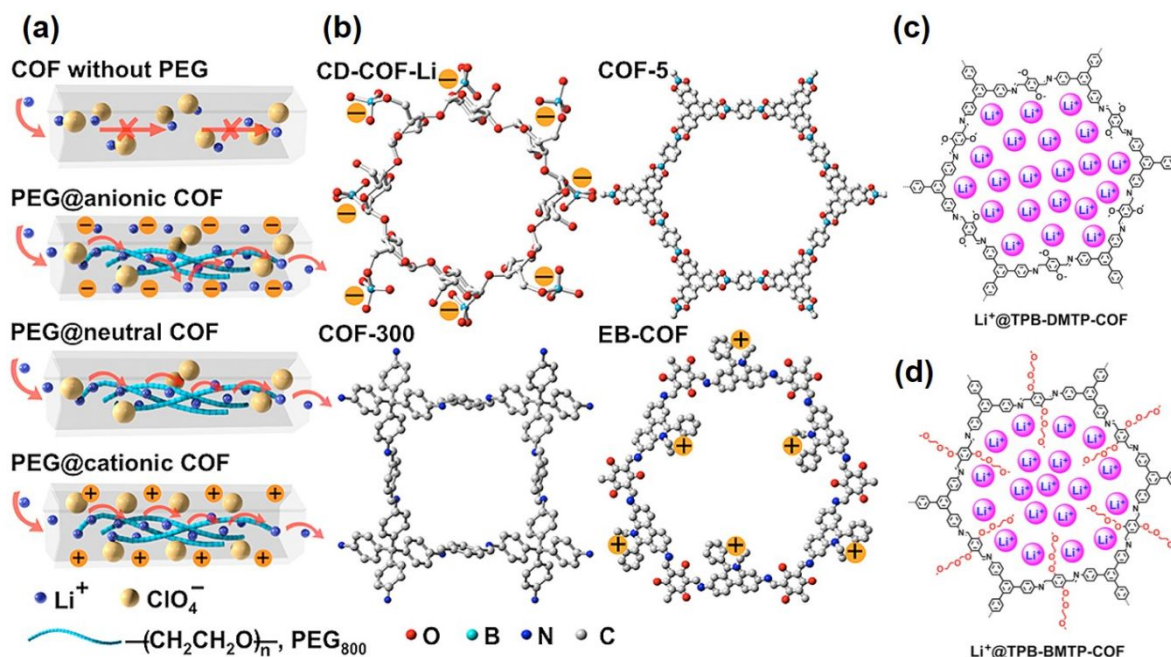


Fig. 17 (a) Schematic of Li^+ transport in COFs/PEG CSSEs, and (b) the structures of some obtained anionic (CD-COF-Li), neutral (COF-5, COF-100), or cationic (EB-COF) COFs³⁶¹, reprinted with permission from ref. 361. Copyright 2019, American Chemical Society. Structures of (c) $\text{Li}^+@$ TPB-DMTP-COF with bare pore walls (lack

polyelectrolyte interface); and (d) Li⁺@TPB-BMTP-COF with oligo(ethylene oxide) chains on pore walls (with a polyelectrolyte interface)³⁶², reprinted with permission from ref. 362. Copyright 2018, American Chemical Society.

A new class of solvent-free, single lithium-ion conductor, lithium sulfonated covalent organic framework (TpPa-SO₃Li), was developed as an SSE³⁶³. Comparing with other porous crystalline ion conductors, this proposed solid state electrolyte can be operated without any solvents and even lithium salts. The anions are covalently tethered into inner of the pores of TpPa-SO₃Li, thus the lithium ions are mobile, exhibiting exceptional ion conductivity ($2.7 \times 10^{-5} \text{ S cm}^{-1}$) and high lithium-ion transference (0.9) number at room temperature.

Four, aside from physically mixing COFs into polymer, or chemically grafting the polymer chains or other functional groups into COFs in a general way, the polymer chains can further orderly arrange on the pores of COFs to form an advanced pathway for lithium ion transport. For instance, some polyelectrolyte COFs with integrated flexible oligo(ethyleneoxide) chains onto the pore walls were reported by Qing Xu, et al.³⁶². Their ionic conductivity shows more than 10³ times than that of the COFs with bare nanochannels, which is due to that a polyelectrolyte interface in the nanochannels which is formed after introducing oligo(ethylene oxide) chains to offer a pathway for lithium ion transport via a vehicle mechanism with lower energy barrier as shown in Fig. 17 (c) and (d).

To overcome the drawbacks of COFs with conventional amorphous polymers such as the insufficient conductivity if without liquid organic solvent, or the limited working temperature below 100°C, Gen Zhang et al.³⁶⁴ incorporated PEO chain into the inner space of 2D MOFs to rationally construct a lithium ionic conduction pathway in their crystalline states. The structures of COF-PEO-x (x is 3, 6, or 9) with various numbers of PEO unites are shown in Fig. 18, which presents different crystalline states. Then, the obtained COF-PEO-x were immersed in LiTFSI/THF solution and further dried at 100°C under vacuum for a long time to form the final CSSE, COF-PEO-x-Li after removing the organic solvent. It is found that the ionic conductivity is depended on the length and dynamics of PEO chains, where the PEO is not just used as polymer matrix but the a bulky and flexible functional group. Moreover, this CSSE is first used in an all-solid-state lithium battery at 100°C with good conductivity, flexibility and stability.

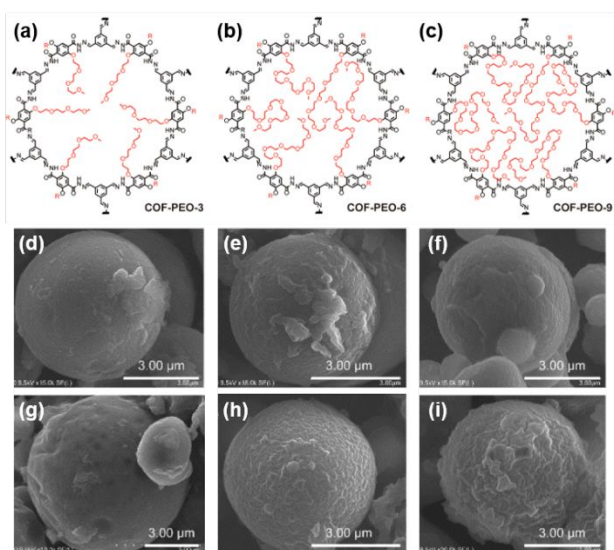


Fig. 18 Chemical structures of COF-PEO-x (x = 3, 6, 9) with various numbers of PEO unites, (a) COF-PEO-3, (b) COF-PEO-6, (c) COF-PEO-9; SEM images of (d) COF-PEO-3, (e) COF-PEO-6, (f) COF-PEO-9, (g) COF-PEO-3-Li, (h) COF-PEO-6-Li and (i) COF-PEO-9-Li.³⁶⁴ Reprinted with permission from ref. 364. Copyright 2019, American Chemical Society.

3.4.3. Porous organic cages (POCs)

Aside from some porous materials such as MOFs and COFs mentioned above, a relatively new class of materials, porous organic cages (POCs), which are without metal ions normally, have generated increasing interest and used as solid state electrolyte in lithium batteries^{365–367}. Here are some crystalline porous organic cages as shown in the Fig. 19 below. A neutral imine cage CC3 (a) with hydrated 3D diamondoid pore network (d) but relatively low proton conductivity can be reduced to form RCC1 (b) and further transformed into crystalline hydrated salt (H₁₂RCC1)¹²⁺·12Cl⁻·4(H₂O) (c, e and f), thus the conductivity can be significantly improved³⁶⁵.

As shown in Fig. 20, a typical case of the electrolyte used in lithium batteries is a solid–liquid electrolyte nanocomposite (SLEN) fabricated from porous molecular cage and LiTFSI/DME (1,2-dimethoxyethane) electrolyte solution proposed by Aaron Petronico and co-workers³⁶⁶, which exhibits exceptional ionic conductivity of $1 \times 10^{-3} \text{ S cm}^{-1}$ at room temperature and a wide electrochemical window of 4.7 V. The organic cage in those POCs imposes a conduction pathway that is necessarily three-dimensional to maximize ionic conduction.

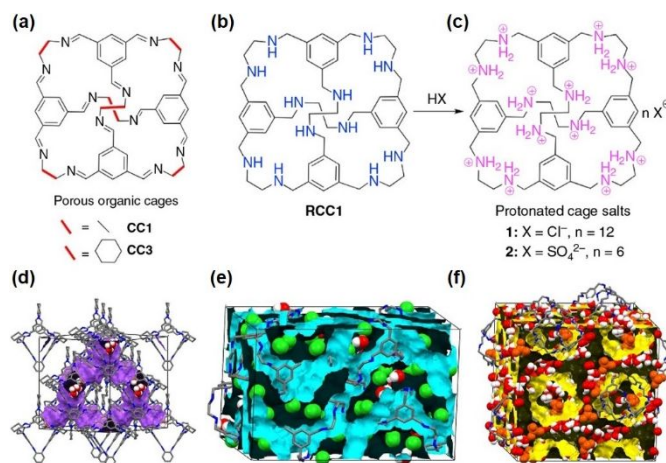


Fig. 19 Molecules of porous organic cages and protonated cage salts. (a) Neutral porous organic cages CC1 and CC3, (b) and (c), from RCC1 (RCC1; the reduced form of CC1) to protonated cage salts; (d) hydrated 3D diamondoid pore network of CC3; 3D interconnected pores in 1 (e) and 2 (f).³⁶⁵ Reprinted with permission from ref. 365. Copyright 2016, Nature Publishing Group.

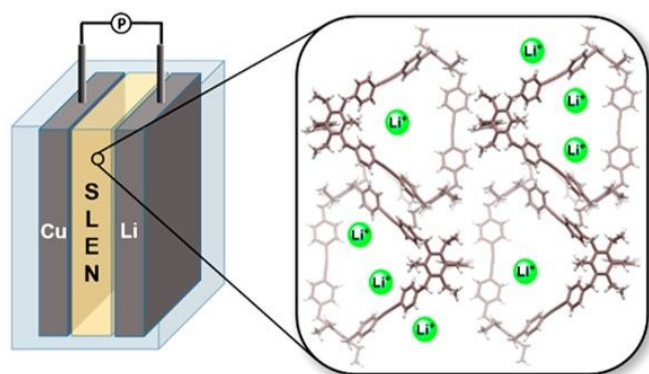


Fig. 20 Schematic illustrations of solid-liquid electrolyte nanocomposite (SLEN) half-cell configuration and the magnified structure of SLEN. ³⁶⁶ Reprinted with permission from ref. 366. Copyright 2018, American Chemical Society.

Table 7 COF-derived solid state electrolytes

	Fillers (NP)	Solid electrolytes	σ (S cm ⁻¹)	Ref.
With organic solvent and lithium salt	Porous CB[6]	CB[6]/0.8LiPF ₆ -3PC	0.9±0.4 × 10 ⁻⁴ (RT)	352
		CB[6]/0.4LiClO ₄ -3.4PC	0.8±0.4 × 10 ⁻⁴ (RT)	352
		CB[6]/1.1LiPF ₆ -2.2DMC	1.0±0.2 × 10 ⁻⁴ (RT)	352
	COF-5	COF-5/LiClO ₄ /THF	2.6 × 10 ⁻⁴ (25°C)	353
	TpPa-1	TpPa-1/LiClO ₄ /THF	1.5 × 10 ⁻⁴ (25°C)	353
	ICOF-2	ICOF-2/PVDF/PC	3.16 × 10 ⁻⁵ (RT)	355
	CD-COF-Li	CD-COF-Li/LiPF ₆ /EC-DMC	2.7 × 10 ⁻³ (30°C)	356
	H-ImCOF	H-ImCOF/LiClO ₄ /PC	4.0 × 10 ⁻⁵ (RT)	357
With organic solvent	H-Li-ImCOF	H-Li-ImCOF/PC	5.3 × 10 ⁻³ (RT)	357
	CH ₃ -Li-ImCOF	CH ₃ -Li-ImCOF/PC	8.0 × 10 ⁻⁵ (RT)	357
	CF ₃ -Li-ImCOF	CF ₃ -Li-ImCOF/PC	7.2 × 10 ⁻³ (RT)	357
	H-COF-1@10	H-COF-1@10/PVDF/LiClO ₄ /EC-DMC	2.5 × 10 ⁻⁴ (RT)	358
Without organic solvent and/or lithium salt	CON	Li-CON-TFSI	2.09 × 10 ⁻⁴ (70°C)	359
	EB-COF	PEG-Li ⁺ @EB-COF-ClO ₄	1.78 × 10 ⁻³ (120°C)	361
	TpPa-SO ₃ Li	TpPa-SO ₃ Li	2.7 × 10 ⁻⁵ (RT)	363
With lithium salt	TPB-BMTP-COF	TPB-BMTP-COF/LiClO ₄	6.04 × 10 ⁻⁶ (40°C), 5.49 × 10 ⁻⁴ (90°C)	362
	TPB-DMTP-COF	TPB-DMTP-COF/LiClO ₄	1.36 × 10 ⁻⁷ (40°C), 5.37 × 10 ⁻⁶ (70°C)	362
With lithium salt in polymer matrix	TPB-DMTP-COF	TPB-DMTP-COF/PEO ₄₀₀ /LiClO ₄	7.93 × 10 ⁻⁵ (40°C), 2.48 × 10 ⁻⁴ (70°C)	362
	COF-PEO-x	COF-PEO-3/LiTFSI	9.52 × 10 ⁻⁵ (200°C)	364
		COF-PEO-6/LiTFSI	3.71 × 10 ⁻⁴ (200°C)	364
		COF-PEO-9/LiTFSI	1.33 × 10 ⁻³ (200°C)	364

*COF-5, C₉H₄BO₂; ICOF-2, a spiroborate-linked ionic covalent organic framework with lithium counterion; PC, propylene carbonate; DMC, dimethylcarbonate; THF, tetrahydrofuran; CD, cyclodextrins; LiTFSI, lithium bis (trifluoromethane)sulfonimide; CON, COF nanosheet; TPB, 1,3,5-Tri(4-aminophenyl) benzene; BMTP, 2,5-bis((2-methoxyethoxy)methoxy)terephthalaldehyde; DMTP, 2,5-Dimethoxyterephthalaldehyde; H-COF-1@10, COF-1 ((C₃H₂BO)₆(C₉H₁₂)₁) with different porosity; COF-PEO-9, here PEO-9 is 2,5-bis((2,5,8,11,14,17,20,23,26-nonaooxaoctacosan-28-yl)oxy)terephthalohydrazide; ImCOFs, imidazolate-based COFs; H-ImCOF, (C₂₇H₂₀N₄)_n; H-Li-ImCOF, (C₂₇H₁₉N₄Li)_n; CH₃-Li-ImCOF (C₂₈H₂₁N₄Li)_n; CF₃-Li-Im-COF (C₂₈H₁₈N₄F₃Li)_n; EB, ethidium bromide; TpPa-SO₃Li, which is prepared from TpPa-SO₃H (Tp is 1,3,5-triformylphloroglucinol, Pa-SO₃H is 1,4-phenylenediamine-2-sulfonic acid) and LiOAc.

4. Emerging advanced characterization and computational simulation technologies

In order to overcome challenges such as higher ionic conductivity, long term stability and economic feasibility to meet the requirements of further practical implementation and commercialization, deep and fundamental understandings are necessary. Specifically, the investigations on ASSLBs involve complicated material analysis such as crystal structure and morphology, deeper chemical analysis

including elemental and valence state, real-time electrochemical processes, etc.⁸⁷ Although composite electrolytes can overcome the shortcomings of each consisting component and even leverage their advantages, the characterization and clarification for those above investigations in such a composite system are much more challenging⁸⁷. In the last few years, some advanced computational methods and novel techniques have been designed and established to facilitate these investigations specifically, which will be focused on in this section.

4.1 In situ or operando techniques

Normally, four main categories of prevailing techniques are chosen to investigate the SSEs. First, the basic crystal structures from XRD and neutron diffraction patterns (NDP) with precise refinements. Second, electrochemical measurement to evaluate their electrochemical performance using current–voltage (I–V) tests, electrochemical impedance spectroscopy (EIS), linear sweep voltammetry (LSV), etc. Third, microstructure characterization through scanning electron microscopy (SEM), transmission electron microscopy (TEM), scanning transmission electron microscopy (STEM), scanning tunneling microscopy (STM)/scanning tunneling spectroscopy (STS) and atomic force microscopy (AFM). Four, some typical surface analysis by XPS (X-ray photoelectron spectroscopy, or ESCA, electron spectroscopy for chemical analysis), SIMS (secondary ion mass spectroscopy), AES (auger electron spectrometry), and LEIS (low-energy ion scattering spectroscopy) with the inspect surface depths from interfaces of 1–10 nm, several to hundreds of nm, 1–3 nm, as well as to inspect the outer atomic monolayer.²

Unlike the conventional *ex situ* techniques, which are static and difficult to capture the materials structures or the electrochemical processes in metastable or unstable conditions, some emerging *in situ* or even operando characterization techniques can directly identify the dynamic information for material structures or reaction processes in real time⁵⁹. Here *in operando* means the measurement is performed when the battery is in operation, which is one specific case of *in situ*³⁶⁸. Some of these techniques have been widely used in the researches on SSEs of lithium batteries.

The first basic one is the *in situ* XRD measurement for overall crystal structure at various conditions. Such as the materials formation at increasing temperatures from room temperature to 800 °C for $\text{LiMn}_{1.5}\text{Ni}_{0.5}\text{O}_4$ (LMNO) and $\text{Li}_{1.4}\text{Al}_{0.4}\text{Ge}_{1.6}(\text{PO}_4)_3$ (LAGP) powders, thus the interfacial products between electrode and electrolyte can be determined at elevated temperature.³⁶⁹ Or the crystal behavior of $\text{Li}_7\text{La}_3\text{Zr}_2\text{O}_{12}$ (LLZO) in the absence of pressure mediums during compression and decompression.³⁷⁰ Moreover, XPS can detect the chemical constitution and valence state of a certain system, while the *in situ* XPS can dynamically study the chemical reaction during electrochemical processes^{371–373}. A typical use for lithium battery is to understand the formation and evolution process for the solid-electrolyte interphase (SEI) between metal electrode and SSE^{374,375}. For instance, the chemical state information provided by *in situ* XPS indicated that the SSE $\text{Li}_7\text{P}_3\text{S}_{11}$ was likely to react with lithium metal electrode to form the decomposition phases of Li_2S and Li_3P ³⁷⁴. On this basis, another research further demonstrated how the SEI layer evolves chemically during actual battery charge-discharge cycles via operando XPS (opXPS)³⁷⁵, the schematics of opXPS and related Li 1s core level evolution during charging and discharging from 0 to 45 hours are presented in Fig. 21 (a) and (b), in which the SEI layer's formation and further evolution can be clearly reflected. Obviously, the *in situ* and even operando XPS is crucial to further understand the mechanisms of chemical processes in ASSLBs.

In addition to crystal structure or the chemical states of SSEs via X-rays, the lithium ion transport during battery operation can also be detected by *in situ* characterization techniques. A typical candidate is the *in situ* NDP as shown in Fig. 21(c), which is highly sensitive

towards light elements (e.g. H, Li or O) and thus can detect much deeper range than that of ordinary X-rays.^{376,377} Especially, this technique is very suitable for lithium ion battery studies because spatial distribution and density of lithium element during plating and stripping can be accurately observed through this nondestructive method.^{59,378,379} In order to clarify the origin of lithium dendrite formation, Han et al.¹⁷ used operando NDP to determine the dynamic evolution of lithium concentration profiles in three typical SSEs including LiPON, LLZO, and Li_3PS_4 , the results indicate that lowering the electronic conductivity is vital to deal with lithium dendrite issues. Researches on SSEs such as the degradation issues in thin-film system³⁸⁰, or the material behavior at interface of SSE/Li metal^{377,378} are also vital and complimentary towards the goal of understanding SSEs.

Solid-state nuclear magnetic resonance (NMR) is a powerful tool to study local structural environments and dynamics of lithium ion in ASSLBs, in which the NMR active isotopes ^6Li and ^7Li can be detected to reflect the pathways of lithium ions^{268,381}. Particularly, NMR is sensitive enough to distinguish various lithium ions in different structural environments in ceramic phase, polymer phase, or their interfacial region.³⁸² Thus the CSSEs with more complicated components than single phase solid electrolyte can be better investigated through this technique.³⁷⁷ Compared with the *ex situ* NMR, which is difficult to capture the signal in metastable process, the lithium ion transport in real time can be directly identified via *in situ* NMR during battery cycling.³⁸³ For instance, Xu et al.³⁸³ used *in situ* ^7Li NMR to study underlying solid-state (de)lithiation mechanism of the improved electrochemical performance. And Nakayama et al.³⁸⁴ revealed the key factors affecting capacity fading of ASSLBs with PEO as electrolyte using *in situ* ^{19}F -NMR.

Imaging technique is one of the most widely used characterization methods to observe the morphology of energy materials in different scales. Those techniques include *in situ* TEM, *in situ* SEM³⁷⁹ (STEM-EELS), cryo-electron microscopy (CE), *in situ* AFM, operando X-ray tomography microscopy (XTM), and *in situ* electron holography are performed to study the SSEs. One typical research objective using these advanced techniques is to study the interfaces between electrode and solid state electrolyte, in which the interfacial region is a transition layer between different phases with inhomogeneous spatial distribution.⁸⁷ For instance, Li et al.³⁷⁹ observed the morphology evolution of LLZTO near Li/LLZTO interface by employing an *in situ* SEM to study the lithium plating/stripping behavior at the intimately contacted interface.

Other than materials' 2-dimensional surface pictures offered by SEM based on scattered electrons, *in situ* TEM based on transmitted electrons can provided more details about internal crystal or morphology of solid electrolytes with high spatial resolution.² Moreover, using STEM combined with EELS can obtain some conclusive evidences such as atomic distribution³⁸⁵, local crystal orientation³⁸⁶, or valence states³⁸⁷ to further facilitate the research of materials.³⁸⁸ Gong et al.³⁸⁹ used *in situ* STEM to directly observe nanopolycrystallization in a working ASSLBs with LLZO as electrolyte, and found that the single crystal LiCoO_2 became connected through nanopolycrystallization during charging/discharging. As shown in Fig. 21(d) and (e), Wang et al.³⁹⁰ presented *in situ* STEM combined with EELS to observe the phenomena at $\text{LiCoO}_2/\text{LiPON}$ interface in real time and indicated that the interfacial

impedance was caused by chemical changes rather than space charge effects.

Another advanced TEM is cryo-electron microscopy (CE), which measures the samples at a very low temperature of about -185 °C. The first application of this technique on ASSEs was published by Cui's group as presented in Fig. 21(f)³⁹¹, which shows the possibility of single-particle studies of pristine lithium metal and SEI. Moreover, even some organic electrolytes in liquid lithium batteries can also be conveniently investigated as SSEs due to their freezing in the low temperature environment^{392,393}. Representatively, Zachman et al.³⁹³ used cryo-STEM and EELS to obtain the structure, elemental composition, and chemical bonding environment of lithium dendrites and SEI layer, in which cryo-FIB coupled with cryo-SEM is used to present 3D morphologies for better understanding. Considering the destructive operation of FIB-SEM, an alternative method, operando X-ray computed tomography (XCT) has been developed as a non-

destructive 3D radiographic visualization technique, which can directly visualize the morphological and compositional evolution of materials during battery cycling.³⁹⁴

In situ imaging technique can also be combined with some other characterization techniques. Very recently, a novel experimental set-up of *in situ* atomic force microscope-environmental transmission electron microscope (in situ AFM-ETEM) has been proposed to further understand lithium dendrite growth in ASSEs, as shown in Fig. 21(g).³⁹⁵ The individual Li whiskers, i.e. the primary Li dendrite morphologies, can be *in situ* observed at room temperature as shown in Fig. 21(h), it can be seen that the a nano-sized Li ball nucleated from CNT and further growth with a whisker. The growth stress under an increased applied potential was tested and the results provide quantitative benchmarks for the design of SSEs for ASSEs with suppressed Li dendrite formation.

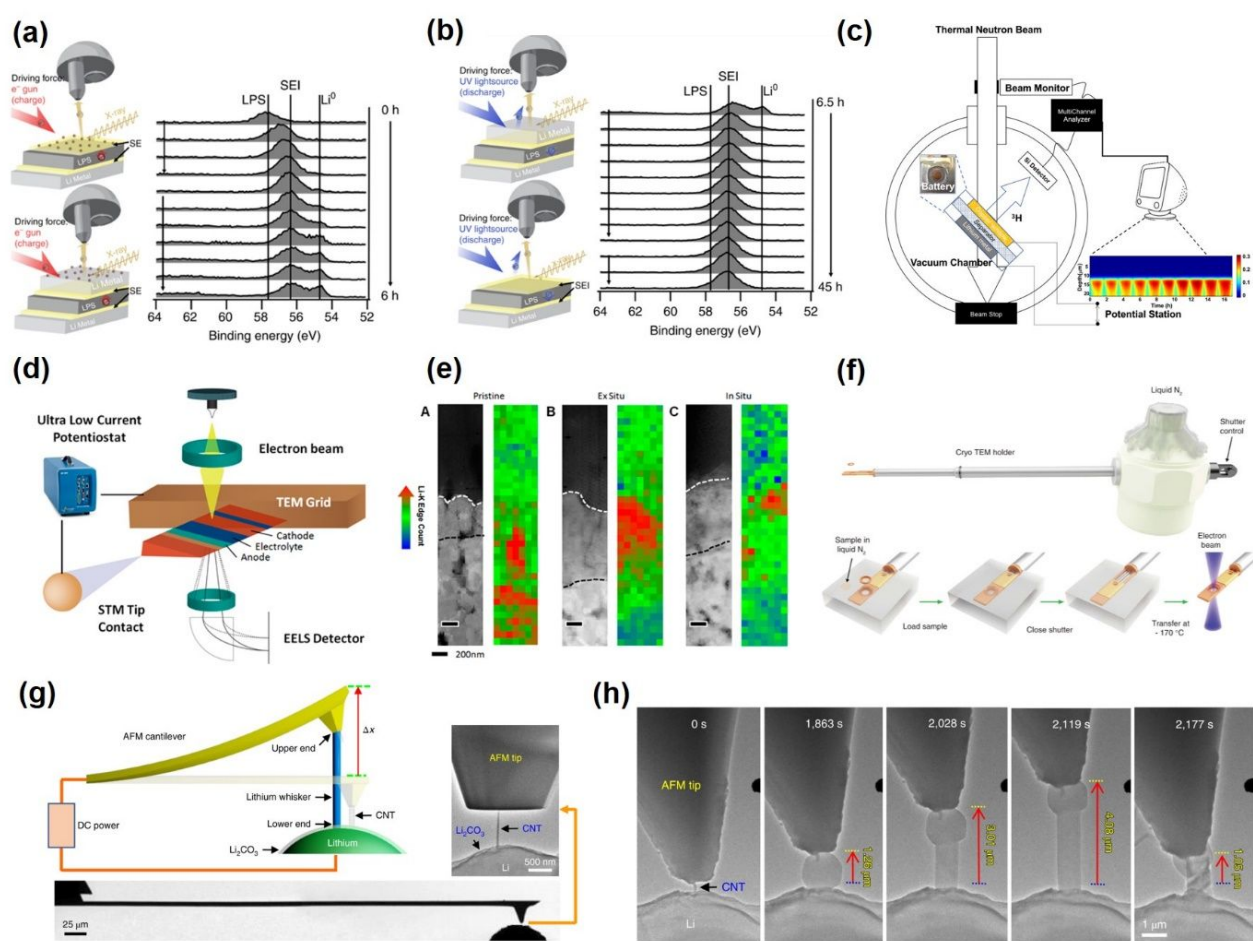


Fig. 21 Some cases for *in situ* or operando techniques. Operando XPS schematic and Li 1s core level evolution during (a) charging from 0 to 6 hours, and (b) discharging from 6.5 to 45 hours;³⁷⁵ reprinted with permission from ref. 375. Copyright 2018, Nature Publishing Group. (c) Operando NDP schematic and the measured Li distribution during 10 plating and stripping cycles at a current density of 1 mA cm⁻²;³⁷⁸ reprinted with permission from ref. 378. Copyright 2019, American Chemical Society. (d) Schematic of *in situ* TEM biasing of nanobattery, (e) STEM image and related EELS mapping, HAADF images of LiCoO₂/LiPON interfacial region along with Li K-edge concentration mappings with pristine, ex situ, and in situ samples.³⁹⁰ reprinted with permission from ref. 390. Copyright 2016, American Chemical Society. (f) schematic diagram of the *in situ* AFM-ETEM set-up, the TEM image of an AFM cantilever approaching the counter electrode of Li metal, and the TEM image of carbon nanotube (CNT) attached to a flattened AFM tip; (h) TEM images of Li whisker growth with time³⁹⁵, reprinted with permission from ref. 395. Copyright 2020, Nature Publishing Group.

Other than these prevailing *in situ*/operando techniques for the studies of SSEs, some other advanced methods such as *in situ* AES³⁷⁵, *in situ* XAS³⁹⁶, high-resolution TOF-SIMS^{397,398} and so on are also being rapidly developed and have widely attracted research attention. While current characterization studies for ASSLBs are mainly focused on the single phase SSEs, very few researches have applied them to CSSEs. Due to the composite system consisting of more components, and the material structures or chemical processes are more complicated to be identified, there are both urgent need and many research opportunities in this regard. In the near future, more and more *in situ*/operando techniques will be further developed and they will play more and more crucial roles in the research of energy materials.⁸⁷

4.2 Advanced computational simulations

Many advanced characterization methods have been developed for further detecting the materials and processes in recent years as summarized above. However, some detailed atomistic information is still very difficult to directly characterize in specific experiments. As a complement to experiments, computational simulation methods play a useful role in analyzing and predicting the structures and properties of materials in an atomic or molecular scale.^{11,399}

Over the past few years, the modelling methods based on first-principles density functional theory (DFT) have been developed and widely used in better understanding of material structures and electrochemical processes, including the energies of atomic structures and the ionic transport mechanisms in SSEs.^{400,401} For instance, Kihun Jeong et al. proposed a novel SSE, lithium sulfonated covalent organic framework (TpPa-SO₃Li) as shown in Fig. 22 (a) and (b). The theoretical elucidation of lithium ions conduction behavior in TpPa-SO₃Li is presented through DFT calculation as shown in Fig. 22 (c).

To be specific, the migration barriers (E_m) of lithium ions in both axial and planar pathways are calculated at various states, including initial (IS), intermediate (IM), transition (TS), and final (FS) states as compared in the energy diagrams. Compared to the energy barriers of lithium ion migration in the planar pathway ($E_m = 31.6 \text{ kcal mol}^{-1}$, Fig. 22(c), bottom), the axial lithium ion migration is preferred and shows lower energy barrier ($E_m = 7.6 \text{ kcal mol}^{-1}$) because of the shorter hopping distances, which is promoted by the O atoms of keto groups (green circles) (Fig. 22 (c), top). Obviously, the DFT simulation plays a useful role to explain the material behaviours and direct the material design for SSE.

In addition to the energies related to lithium ions transfer, the thermodynamics of the chemical and electrochemical stability at the interfaces of electrode and some typical SSEs, including LGPS (Li₁₀GeP₂S₁₂), LLZO (Li₇La₃Zr₂O₁₂), LLTO (Li_{0.33}La_{0.56}TiO₃), LATP (Li_{1.3}Al_{0.3}Ti_{1.7}(PO₄)₃), and LiPON (Li_xPO_yN_z), have been investigated systematically through DFT simulation, in which the calculated decomposition energies (ΔE_D) are regarded as an important indicator to evaluate the stabilities.⁹⁰ Regarding CSSEs, Pazhaniswamy Sivaraj et al.⁴⁰² prepared a PVDF-LiClO₄/LLTO (Li_{0.5}La_{0.5}TiO₃) nano composite solid state electrolyte. The interaction between the inorganic LLTO particles and polymer matrix has been inferred by DFT-IR (infrared spectroscopy) analysis, in which two clusters of C₂H₂LiClO₄ and C₂H₂Li₂LaTiClO₇ are modelled to virtually construct the polymer/lithium salt system (PVDF/LiClO₄) and the inorganic/polymeric composite system (PVDF-LiClO₄/LLTO), respectively. The calculated DFT results of ionization potential, intermolecular distance, and the energy of structural rearrangement reveal that the incorporation of LLTO into the polymer salt cluster reduces the coordination bonding between Li⁺ and ClO₄⁻ in the obtained CSSE, which are in line with the experimental IR analysis.

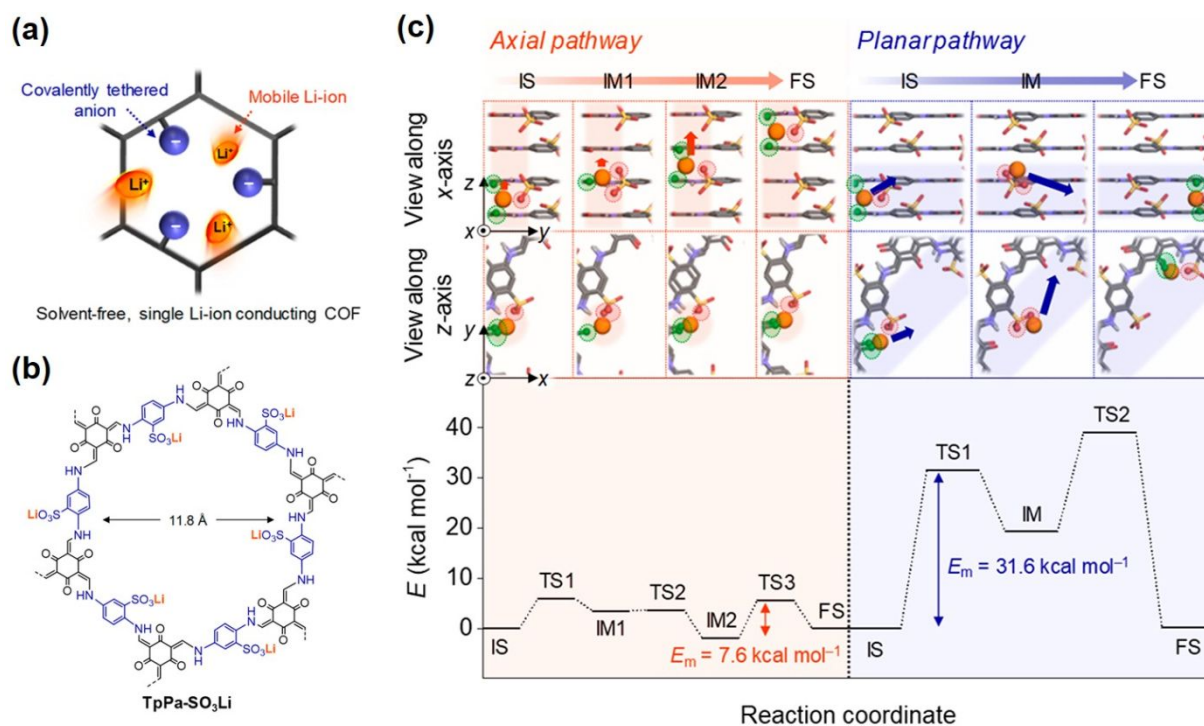


Fig. 22 (a) Conceptual illustrations of ion transport phenomena and (b) chemical structure of TpPa-SO₃Li, and (c) Simulation of Li-ion migration behaviors inside the pore (top) and corresponding energy diagrams (bottom) at the initial (IS), intermediate (IM), transition (TS), and final (FS) states.³⁶³ Reprinted with permission from ref. 363. Copyright 2019, American Chemical Society.

Compared to DFT, which can be used to study the thermodynamics related to material structures and electrochemical processes, molecular dynamics (MD) is an advanced computational simulation method used to learn the physical movements of atoms and molecules, namely focusing on the dynamic evolution process of atoms and molecules within a certain period of time. In MD

simulations, it is recognized that the trajectories of atoms and molecules are controlled by interatomic potentials or molecular mechanics forces, and the motions of interacting particles are numerically solved using Newton's equations.² With respect to SSE for lithium batteries, one typical use of MD simulations is to investigate the Li⁺ transport mechanisms.

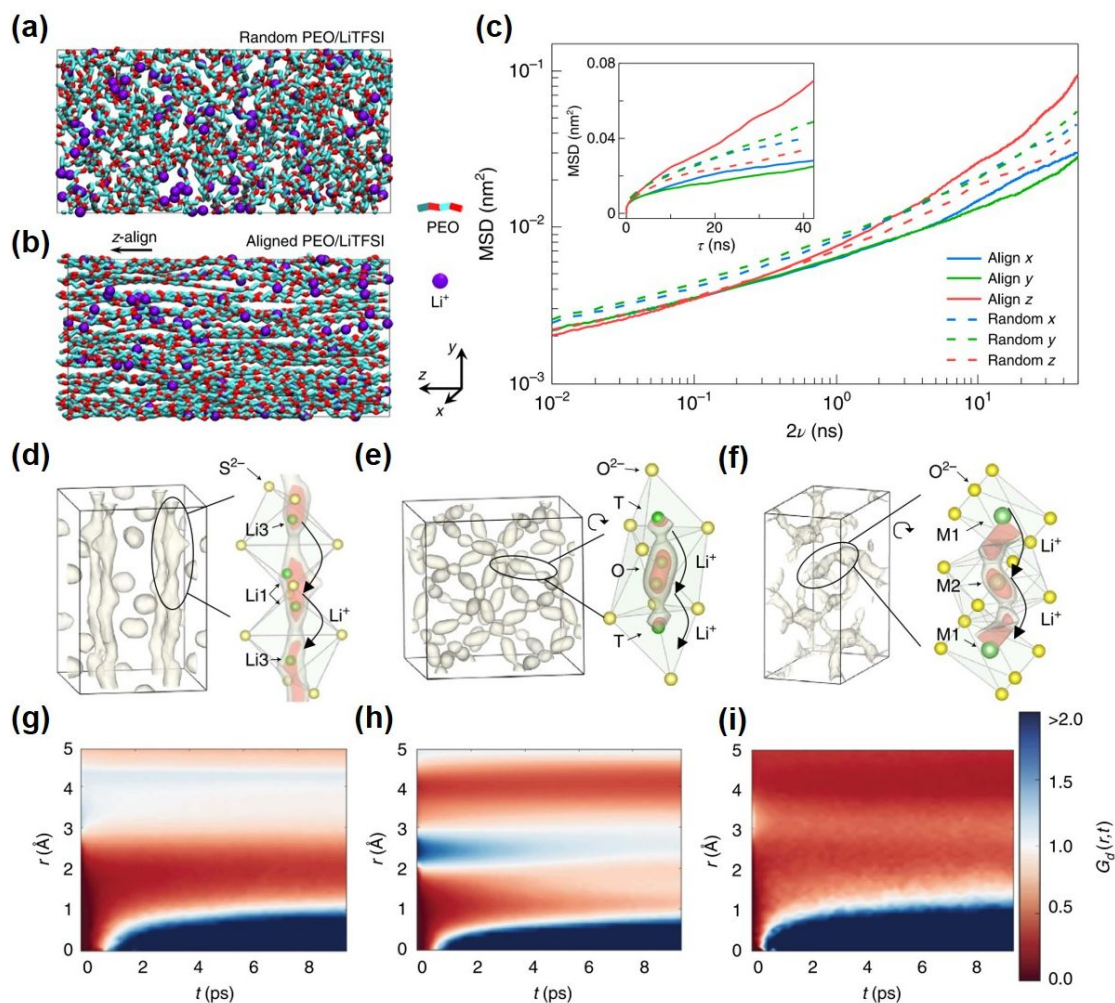


Fig. 23 Simulation model of Li⁺ transport in (a) a random system and (b) z-aligned PEO system, and (c) the corresponding results of MSD vs. time.³¹ Reprinted with permission from ref. 31. Copyright 2019, Nature Publishing Group. The density of Li⁺ spatial occupancy (d-f) and Van Hove correlation functions of Li⁺ dynamics (g-i) of three typical ceramic SSEs during AIMD simulations, including LGPS (Li₁₀GeP₂S₁₂), cubic-phase LLZO (Li₇La₃Zr₂O₁₂) and LATP (Li_{1.3}Al_{0.3}Ti_{1.7}(PO₄)₃), respectively.⁴⁰⁵ Reprinted with permission from ref. 405. Copyright 2017, Nature Publishing Group.

Very recently, a CSSE with vertically aligned structure was proposed by Jiayu Wan et al. in Yi Cui's group³¹. To be specific, an 8.6- μ m-thick nanoporous polyimide (PI) film filled with PEO/LiTFSI vertically was reported (Fig. 23 (a) and (b)) and shows very excellent performances including nonflammable, flexibility, mechanically strong, high conductivity, very good long-term cycling, and also can withstand some abuse tests. The authors use MD simulation to explore

the origin of enhanced ionic conductivity in the CSSE with aligned structure. PEO/LiTFSI with random and aligned polymer chains are simulated and their simulation snapshots are compared in Fig. 23 (c), indicating their difference in Li ionic conduction. Their mean squared displacements (MSDs) of lithium ions at 350 K are also calculated using MD simulation and presented in Fig. 12D (d). Compared to the Li⁺ diffusion with time in all directions in the random system, an

obvious increase of Li^+ diffusion along the aligned z-direction can be observed in the aligned system. In this regard, the best diffusion pathway of Li^+ can be obtained using MD simulations. Some other similar researches of SSE using MD simulations were also carried out, such as the systematic study of Li^+ transport process in polyester-based polymer electrolytes⁴⁰³, the Li^+ transport in the lamellar phase of polystyrene–polyethylene oxide (PS–PEO) block copolymer electrolyte,⁴⁰⁴ or the Li^+ migration in the pores of MOF-modified electrolyte.³⁵¹

Another recently emerging MD method, the *ab initio* molecular dynamics (AIMD) simulations, is proposed for the research of SSEs.^{405,406} It has played the main role in recent advancements such as simulating the density of Li^+ spatial occupancy and Van Hove correlation functions of Li^+ dynamics of three typical ceramic SSEs, including LGPS ($\text{Li}_{10}\text{GeP}_2\text{S}_{12}$), cubic-phase LLZO ($\text{Li}_7\text{La}_3\text{Zr}_2\text{O}_{12}$) and LATP ($\text{Li}_{1.3}\text{Al}_{0.3}\text{Ti}_{1.7}(\text{PO}_4)_3$), as shown in Fig. 23 (d–i).⁴⁰⁵ Compared to the classical MD simulation, which requires force fields that may not be suitable for new materials, AIMD simulations are chemically agnostic and better for predicting SSE candidates.⁴⁰⁷ Moreover, the real-time dynamics of ions in the material modelled over time in AIMD simulations can lead to the direct observation of diffusion mechanisms without the need of related prior assumptions.³⁹⁹ Therefore, AIMD is very suitable to directly reveal the Li^+ transfer pathway and further design new candidates of CSSEs, related researches should be strengthened in future studies.

4.3 Artificial intelligence and machine learning

In recent years, artificial intelligence (AI), which is the broad science of mimicking human abilities, has become the fastest-growing branch of the high-tech industry and gained significant attention in a wide variety of sectors.^{408–410} As a specific subset of AI, machine learning (ML), that trains a machine how to learn, is very prominent and recently used in the area of energy storage and conversion devices,⁴¹¹ especially for the lithium batteries.⁴¹² Some aspects such as critical materials selection,⁴¹³ cell design, state estimation,^{414,415} charging optimization,⁴¹² and life prediction^{416,417} can be promoted using ML, from which many time-consuming experiments will be significantly reduced. Relating to the researches on those topics, there are many studies focused on the improvement of SSEs for lithium batteries. Current researches can be divided into several categories, including materials screening,^{418,419} structural properties,⁴²⁰ ion diffusion mechanism,⁴²¹ and composition optimization.⁴²²

One of the typical uses of ML is to select the suitable SSE candidate materials. The conventional DFT-MD simulations guided by ML-based model are performed to discover new solid lithium ion conductors for ASSLBs, in which over 12000 candidates with very diverse structures and compositions are screened.⁴¹⁸ Compared to the conventional DFT approach or the random search of materials space, the ML-based model is much more efficient for identification of Li^+ conductor.

Aside from the screenings based on lithium superionic conductivity, stability at the interface of SSE and Li metal anode is also regarded as the criteria.⁴¹⁹ Mechanical properties of inorganic SSEs including shear moduli, bulk moduli, and elastic constants, are fed into the theoretical framework as the feature parameters to evaluate the stabilities related to lithium dendrite. Crystal graph

convolutional neural network (CGCNN) is performed to predict the shear and bulk moduli, and the gradient boosting regression and kernel ridge regression (KRR) are employed to train the elastic constants. As a result, 12950 solids and over 15000 interfaces have been screened and over 20 interfaces with six solid electrolytes are selected as candidates.

Another typical case focused on improving the stability at SSE/Li interface was proposed by Bo Liu *et al.*⁴²³, who used ML and automated reaction screening to select the appropriate dopants in LLZOM (M doped $\text{Li}_7\text{La}_3\text{Zr}_2\text{O}_{12}$, here M is dopant, Fig. 24(a) and (b)) to improve the interfacial stability between SSE and lithium metal anode. ML methods including support vector machine (SVM) and kernel ridge regression (KRR) are performed to evaluate the thermodynamic stability and reaction energy at the interface, respectively. The formation energy per atom ($\Delta H_{f,x+y}$ in M_xO_y , which is defined as $\Delta H_{f,x+y} = \Delta H_f/(x+y)$) and product of coordination number CN with the formation energy of oxide M_xO_y per M atom ($\text{CN} \times \Delta H_{f,x}$) are regarded as indicators of the M–O chemical bond strength which determine the interfacial thermodynamic stability. The results are presented in Fig. 24(c), in which 100 LLZOM compounds considered and the stable and unstable compounds at electrolyte/Li anode interface are clearly divided by the black solid line. Additionally, the reaction energy (ΔG) between LLZOM and Li is further predicted by ML and confirmed by DFT calculations as shown in Fig. 24(d), indicating a good agreement between those two methods. All in all, this research shown a good potential for material screening and improving by ML approach.

In addition to the material selection, further researches into the ionic transfer mechanism of SSEs using ML have also been performed. Specifically, the structural properties of lithium ionic conductors are investigated using ML and high-throughput bond-valence calculations.⁴²⁰ 1025 Li compounds of ICSD (Inorganic Crystal Structure Database) have been scanned and their crystal structures are characterized by some descriptors such as the cation site energy (E_{site}), cation bond-valence sum (BVS), migration energy (E_m), computed percolation radius (r_p), the cation–cation and cation–anion coordination numbers (N), etc., which are derived from bond-valence (BV) theory, graph percolation and geometric analysis. Then the ML technique known as random forests is used to build a regression model to connect the set of descriptors with the target property of ion migration energy. As shown in Fig. 24(e), the correlation of each two descriptors can be obtained, for example, the E_m and r_p are negatively correlated, because the increased r_p will reduce the repulsive forces and further lead to reduced E_m . Furthermore, the results of scanned ICSD of the SSEs are summarized and the correlations between E_m and r_p are shown in Fig. 24(f), indicating a negative correlation between these two descriptors. As a result, some lithium ionic conductors with a r_p of ca 0.5 Å and lower E_m are selected as shown in this figure, including $\text{Li}_{10}\text{GeP}_2\text{S}_{12}$, $\text{LiTi}_2(\text{PO}_4)_3$, $\text{Li}_7\text{La}_3\text{Zr}_2\text{O}_{12}$, $\text{Li}_{0.3}\text{La}_{0.567}\text{TiO}_3$, and $\text{Li}_{6.72}\text{PS}_5\text{Cl}$.

Most of the current researches on SSEs using ML are mainly focused on pure inorganic ceramics, with very few studies relating to CSSEs. One similar case in point is about composite lithium ionic conductors, an optimum composition ratio of ternary Li_3PO_4 – Li_3BO_3 – Li_2SO_4 (LPO–LBO–LSO) system was predicted by ML and DFT-MD simulations.⁴²² The model unit cells for the ternary mixed system is presented in Fig. 24(g). Here the composition ratio (A, B, C) indicates

the percentiles of LPO, LBO, and LSO, respectively. For the three phases, 15 different composition ratios are simulated through ML techniques using Gaussian process regression to predict the Li-ion conductivity and phonon free energy, and the results are presented in Fig. 24 (h) and (i), from which the composition ratio with highest conductivity can be seen clearly. The correlation between ionic conductivity and phonon free energy can also be found, although it is not as strong as that in a binary system⁴²⁴. Moreover, another parameter used for prediction of proper ratio is z-score, which is

defined as $z(x) = [\sigma(x) - \sigma_{\max}] / \delta(x)$ ($x = (A, B, C)$); $\sigma(x)$ is the predicted value of Li-ion conductivity as a function of the composition ratio; $\delta(x)$ is the standard deviation at x ; σ_{\max} is the maximum value among the 15 models, 193.0 S cm⁻¹). In this way the ranking of the z-score and its composition ratio have been summarized and the best predicted ratio is (55, 26, 19) as shown in Fig. 24(j). Compared to DFT-MD screening which is difficult to cover the entire combinatorial space, ML strategy can explore the vast number of combinations available.

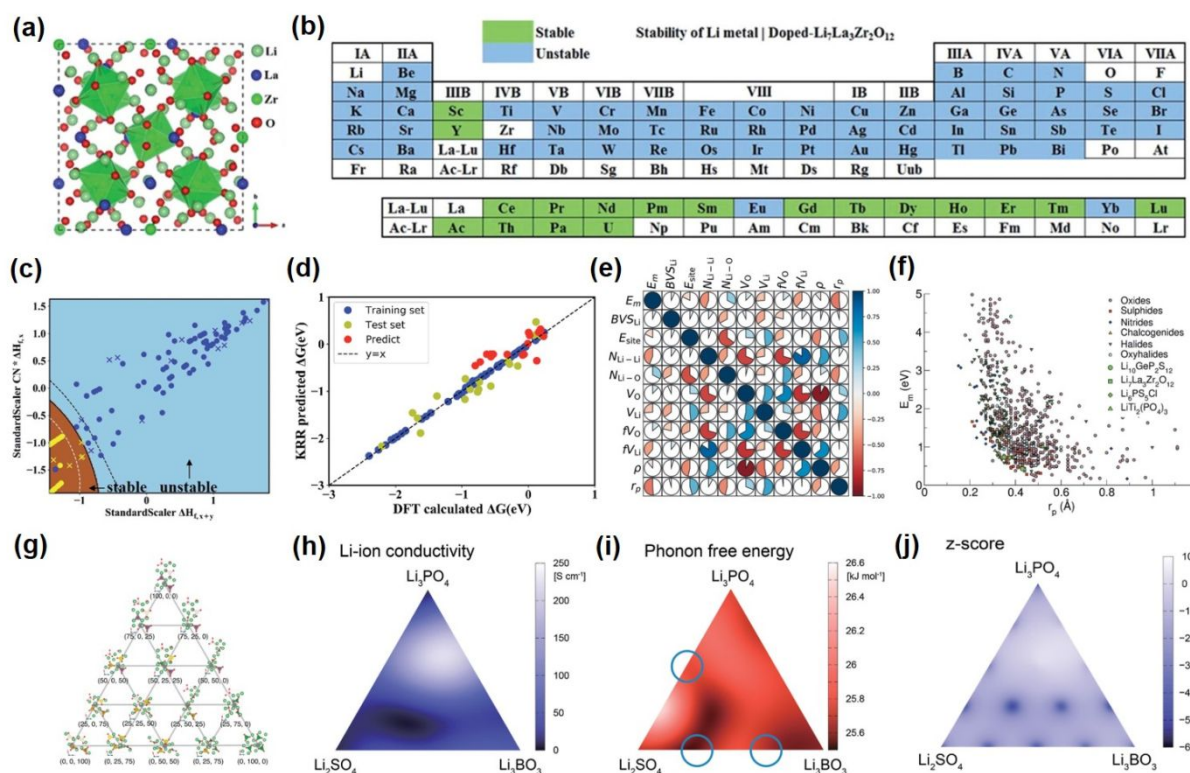


Fig. 24 Some cases for SSEs using ML. (a) The crystal structure of $\text{Li}_7\text{La}_3\text{Zr}_2\text{O}_{12}$ and its possible doped elements in periodic table; (b) The workflow of computational screening of SSEs using ML to improve the interfacial stability; (c) Map of $\Delta H_{f,x+y}$ vs. $(\text{CN} \times \Delta H_{f,x})$, blue circles and yellow circles are the 100 training data points, and blue crosses and yellow crosses are the 18 predicted data points. Stable and unstable regions are presented by brown and sky-blue areas; (d) DFT calculated reaction energies (ΔG) vs. ML predicted reaction energies using a kernel ridge regression model.⁴²³ Reprinted with permission from ref. 423. Copyright 2019, Royal Society of Chemistry. (e) Correlograms between the descriptors for lithium compounds, the descriptors include percolation radius (r_p), ion migration energy (E_m), the cation bond-valence sum (BVS), the anion and cation volume fractions (fV_{O} and fV_{cation}), the cation site energy (E_{site}), the Voronoi polyhedra of the anion and cation (V_{O} and V_{cation}), the cation-cation and cation-anion coordination numbers ($N_{\text{cation-cation}}$ and $N_{\text{cation-O}}$) and density (ρ). (f) Ionic migration energy (E_m) vs. the percolation radius (r_p) for lithium compounds; (g) Model unit cells for the ternary LPO-LBO-LSO mixed system; Contour maps of (h) Li-ion conductivity and (i) normalized phonon free energy of 15 simulated data points, the open blue circles indicate the presents of valleys; (j) Contour map of the z-score.⁴²⁰ Reprinted with permission from ref. 420. Copyright 2019, International Union of Crystallography.

5. Summary, challenges and perspectives

5.1 Summary for this review paper

To facilitate the research and development of composite solid state electrolytes (CSSEs) of inorganics and polymers used for all solid state lithium batteries (ASSLBs), a comprehensive overview of developments in recent years in advanced materials and structures are presented in this paper. Aside from a brief history from solid-state ionic conductors to composite solid-state electrolytes being reviewed first, the fundamentals including basic structure of ASSLBs with

CSSEs, key evaluation parameters, mechanisms of Li ionic transport and performance requirements for CSSEs, are then summarized. Particularly, the main contents of key materials and advanced structures of CSSEs are classified and summarized in this paper, which are divided into the inorganic fillers in polymer matrix, heterogeneous layered structures, 3D inorganic continuous framework with filled polymer, and open-framework related composite electrolytes. In addition, to further accelerate the developments of CSSEs and their practical uses, advanced characterization and simulation techniques are also presented for better understanding.

5.2 Challenges and perspectives

Despite the rapid advances and increasing research efforts summarized in this review, current researches for CSSEs are in still in their infancy. It seems that the technical maturity of CSSEs used in ASSLBs for energy conversion and utilization is still not sufficient to reach the requirements for practical implementation or commercialization. This is due to several major challenges, such as the not yet fully understood mechanisms for ionic transport in CSSEs, the sluggish ionic conductivities, chemical/electrochemical/mechanical/thermal stability issues of ASSLBs with CSSEs, insufficient economic and technological feasibilities. More details for the challenges and perspectives are presented below.

(1) Further fundamental understanding of ion conduction mechanisms and material behaviors in CSSEs. The physical models of intrinsic ionic transportation in each type of pure SSEs have been built up since the first proposed solid ionic conductors, however, most of the models are focused on the intrinsic ion conduction mechanisms within pure SSEs, and some controversial theories still need to be clarified. As for various CSSE systems, the ionic conduction mechanisms between different material compositions and phases play a critical role in lithium ion conduction, especially for the complicated interfacial regions between inorganic fillers/polymers, polymers/polymers, inorganic ceramics/inorganic ceramics, and CSSEs/electrodes. Therefore, it's more necessary to further our understanding on the complex ion conduction mechanisms. To achieve this goal, both experimental and theoretical approaches should be performed to investigate the Li ions' behaviors in CSSEs, which includes the thermodynamic and kinetic behavior in migration process. As we summarized, only very few researches employ the advanced characterizations and computational simulation technologies in the research of CSSEs. Obviously, those advanced methods such as *in situ/operando* NDP, XTM, solid-state NMR, etc. or the simulation methods such as DFT and AIMD, can meet the complex needs well for those composite material systems.

(2) Further enhancing the ionic conductivities of CSSEs via developing novel materials or/and optimizing structures. Although there are some recent advances in improving the conductivities of CSSEs, the current conductivities in most reports are still in the range of 10^{-4} to 10^{-5} S cm^{-1} at room temperature. Very few works can reach up to 10^{-3} S cm^{-1} or even higher. To maximize the performance of solid-state batteries and further accelerate their practical implementation, requirement of 10^{-3} to 10^{-2} S cm^{-1} at ambient temperature comparing to that of liquid electrolyte should be met. In addition to current structural system reviewed in this paper, basing on deeper understanding of the fundamentals, some other advanced novel structures or electrolyte materials could be further developed in interdisciplinary fields. Aside from that, the interactions between different components in CSSEs should be strengthened to facilitate continuous ionic migration. On the other hand, AI and ML are useful tools to precisely and efficiently develop novel materials and also optimize their structures and compositions, which is very suitable for the discovery and screening of fast lithium ion candidates, and further design of the complicated composite material systems. Those computational technologies have seldom been used in current studies of CSSEs, but are critical and expected in thriving development of solid state batteries in the near future.

(3) Optimizing the stabilities between CSSEs and electrode even at higher current density, high-voltage and wider temperature range. Multifaceted stabilities including chemical, electrochemical, thermal, and mechanical stabilities between SSEs and electrode are significant for the long-term operation of ASSLBs. The perform of CSSEs, especially the inorganic fillers in polymer matrix, the double or sandwiched layered structure, or the 3D inorganic continuous frameworks with polymer infiltration, can largely mitigate the stability issues, including decreasing the interfacial resistance of ceramic/electrode, or enhancing the mechanical strength of polymer-based systems. However, most of current researches are still in the preliminary stage and incomplete. Operating the batteries at more extreme conditions such as higher current density, high-voltage and wider temperature range should be considered in the future research to further improve their performance (e.g. higher energy density) and broaden application scenarios. Therefore, further in-depth studies on the stabilities in ASSLBs with CSSEs is still indispensable and urgent. Some researches could be highlighted in the future endeavors, such as interfacial characterization for greater understanding of the interfacial chemical reactions kinetics, interfacial protection layers with antioxidation and/or inhibit reduction to extend the stability window (e.g. 0-5 V) for high-voltage ASSLBs, the degradation mechanism under higher current density, the material behaviors, e.g. lithium dendrite growth, at interfacial region at severe temperature condition (below 0 °C and above 40 °C), or the mechanical properties in a proper range, such as a thickness less than 100 μm to further reduce interfacial resistance, or a value of Young's modulus higher than 5 MPa to suppress dendrite and accommodate the stress from battery assembly and the cycling process.

(4) Improvement of economic and technological feasibilities for practical implementation of ASSLBs with CSSEs. Compared to current conventional liquid electrolyte used for lithium batteries, obviously higher production cost is required for most available SSEs, especially for the CSSEs contained complex structures or components. To improve the economic feasibility, the design and manufacturing of CSSEs should be considered in advance, such as the selection of components without or with less rare earth or expensive elements, simplifying the synthesis routes with regards to raw materials-saving and energy-saving, and designing the CSSEs with reasonable composite structures. Moreover, the scale-up of production is still remain challenges for processing, the compatibilities of CSSEs and electrodes or various components inside CSSEs should be ensured during synthesis and even running. The balance between mechanical flexibilities (strength, thickness, and elasticity) and enough practical energy densities is also indispensable. Beyond CSSEs, the risk in storage and transport of lithium metal should also be addressed with protection systems. Finally, one more consideration to facilitate the practical implementation is the unified and well-established evaluation criteria for the performance, safety and recycling of CSSEs and even solid-state batteries in both researches and actual applications.

Acknowledgements

The authors would like to acknowledge the financial support from the Natural Sciences and Engineering Research Council of Canada (NSERC), the University of Waterloo, and the Waterloo Institute for Nanotechnology.

References:

- H. Zhang, C. Li, M. Piszcz, E. Coya, T. Rojo, L. M. Rodriguez-Martinez, M. Armand and Z. Zhou, *Chem. Soc. Rev.*, 2017, **46**, 797–815.
- Y. Zheng, J. Wang, B. Yu, W. Zhang, J. Chen, J. Qiao and J. Zhang, *Chem. Soc. Rev.*, 2017, **46**, 1427–1463.
- Y. Zheng, W. Zhang, Y. Li, J. Chen, B. Yu, J. Wang, L. Zhang and J. Zhang, *Nano Energy*, 2017, **40**, 512–539.
- Q. Zhao, S. Stalin, C. Z. Zhao and L. A. Archer, *Nat. Rev. Mater.*, 2020, **5**, 229–252.
- Q. Zheng, Y. Yamada, R. Shang, S. Ko, Y. Y. Lee, K. Kim, E. Nakamura and A. Yamada, *Nat. Energy*, 2020, **5**, 291–298.
- E. Pomerantseva, F. Bonaccorso, X. Feng, Y. Cui and Y. Gogotsi, *Science*, 2020, **366**, 8285.
- Y. Zheng, C. Zhao, Y. Li, W. Zhang, T. Wu, Z. Wang, Z. Li, J. Chen, J. Wang, B. Yu and J. Zhang, *Nano Energy*, 2020, **78**, 105236.
- B. M. Li and J. Lu, *Science*, **367**, 979–980.
- G. Harper, R. Sommerville, E. Kendrick, L. Driscoll, P. Slater, R. Stolkin, A. Walton, P. Christensen, O. Heidrich, S. Lambert, A. Abbott, K. Ryder, L. Gaines and P. Anderson, *Nature*, 2019, **575**, 75–86.
- Y. Chen, Z. Wang, X. Li, X. Yao, C. Wang, Y. Li, W. Xue, D. Yu, S. Y. Kim, F. Yang, A. Kushima, G. Zhang, H. Huang, N. Wu, Y. W. Mai, J. B. Goodenough and J. Li, *Nature*, 2020, **578**, 251–255.
- X. Yang, J. Luo and X. Sun, *Chem. Soc. Rev.*, 2020, **49**, 2140–2195.
- C. Sun, J. Liu, Y. Gong, D. P. Wilkinson and J. Zhang, *Nano Energy*, 2017, **33**, 363–386.
- S. Li, S. Q. Zhang, L. Shen, Q. Liu, J. Bin Ma, W. Lv, Y. B. He and Q. H. Yang, *Adv. Sci.*, 2020, **7**, 1903088.
- Z. P. Cano, D. Banham, S. Ye, A. Hintennach, J. Lu, M. Fowler and Z. Chen, *Nat. Energy*, 2018, **3**, 279–289.
- M. Forsyth, L. Porcarelli, X. Wang, N. Goujon and D. Mecerreyes, *Acc. Chem. Res.*, 2019, **52**, 686–694.
- A. Manthiram, X. Yu and S. Wang, *Nat. Rev. Mater.*, 2017, **2**, 1–16.
- F. Han, A. S. Westover, J. Yue, X. Fan, F. Wang, M. Chi, D. N. Leonard, N. J. Dudney, H. Wang and C. Wang, *Nat. Energy*, 2019, **4**, 187–196.
- T. K. Schwietert, V. A. Arszewska, C. Wang, C. Yu, A. Vasileiadis, N. J. J. de Klerk, J. Hageman, T. Hupfer, I. Kerkamm, Y. Xu, E. van der Maas, E. M. Kelder, S. Ganapathy and M. Wagemaker, *Nat. Mater.*, 2020, **19**, 428–435.
- H. Liu, X. B. Cheng, J. Q. Huang, H. Yuan, Y. Lu, C. Yan, G. L. Zhu, R. Xu, C. Z. Zhao, L. P. Hou, C. He, S. Kaskel and Q. Zhang, *ACS Energy Lett.*, 2020, **5**, 833–843.
- S. Randau, D. A. Weber, O. Kötz, R. Koerver, P. Braun, A. Weber, E. Ivers-Tiffée, T. Adermann, J. Kulisch, W. G. Zeier, F. H. Richter and J. Janek, *Nat. Energy*, 2020, **5**, 259–270.
- A. Miura, N. C. Rosero-navarro, A. Sakuda, K. Tadanaga, N. H. Phuc, A. Matsuda, N. Machida, A. Hayashi and M. Tatsumisago, *Nat. Rev. Chem.*, 2019, **3**, 189–198.
- W. Liu, S. W. Lee, D. Lin, F. Shi, S. Wang, A. D. Sendek and Y. Cui, *Nat. Energy*, 2017, **2**, 1–7.
- T. Famprikis, P. Canepa, J. A. Dawson, M. S. Islam and C. Masquelier, *Nat. Mater.*, 2019, **18**, 1278–1291.
- J. C. Bachman, S. Muy, A. Grimaud, H. H. Chang, N. Pour, S. F. Lux, O. Paschos, F. Maglia, S. Lupart, P. Lamp, L. Giordano and Y. Shao-Horn, *Chem. Rev.*, 2016, **116**, 140–162.
- S. Yu, R. D. Schmidt, R. Garcia-Mendez, E. Herbert, N. J. Dudney, J. B. Wolfenstine, J. Sakamoto and D. J. Siegel, *Chem. Mater.*, 2016, **28**, 197–206.
- X. Wang, H. Zhai, B. Qie, Q. Cheng, A. Li, J. Borovilas, B. Xu, C. Shi, T. Jin, X. Liao, Y. Li, X. He, S. Du, Y. Fu, M. Dontigny, K. Zaghib and Y. Yang, *Nano Energy*, 2019, **60**, 205–212.
- S. Xia, X. Wu, Z. Zhang, Y. Cui and W. Liu, *Chem*, 2019, **5**, 753–785.
- Y. Jiang, X. Yan, Z. Ma, P. Mei, W. Xiao, Q. You and Y. Zhang, *Polymers (Basel)*, 2018, **10**, 1237.
- L. Liu, J. Lyu, J. Mo, P. Peng, J. Li, B. Jiang, L. Chu and M. Li, *Sci. China Mater.*, 2020, **63**, 703–718.
- H. Zhai, P. Xu, M. Ning, Q. Cheng, J. Mandal and Y. Yang, *Nano Lett.*, 2017, **17**, 3182–3187.
- J. Wan, J. Xie, X. Kong, Z. Liu, K. Liu, F. Shi, A. Pei, H. Chen, W. Chen, J. Chen, X. Zhang, L. Zong, J. Wang, L.-Q. Chen, J. Qin and Y. Cui, *Nat. Nanotechnol.*, 2019, **14**, 705–711.
- M. Dirican, C. Yan, P. Zhu and X. Zhang, *Mater. Sci. Eng. R Reports*, 2019, **136**, 27–46.
- M. B. Dixit, W. Zaman, N. Hortance, S. Vujic, B. Harkey, F. Shen, W. Y. Tsai, V. De Andrade, X. C. Chen, N. Balke and K. B. Hatzell, *Joule*, 2020, **4**, 207–221.
- A. Li, X. Liao, H. Zhang, L. Shi, P. Wang, Q. Cheng, J. Borovilas, Z. Li, W. Huang, Z. Fu, M. Dontigny, K. Zaghib, K. Myers, X. Chuan, X. Chen and Y. Yang, *Adv. Mater.*, 2020, **32**, 1–9.
- N. Wu, P. Chien, Y. Qian, Y. Li, H. Xu, N. S. Grundish, B. Xu, H. Jin, Y. Hu, G. Yu and J. B. Goodenough, *Angew. Chemie*, 2020, **132**, 4160–4166.
- M. Faraday, *Phil. Trans. R. Soc. Lond.*, 1833, **132**, 675.
- S. S. C. K. Kendall, *High Temperature Solid Oxide Fuel Cells (SOFCs): Fundamentals, Design and Applications*, 2003, Variozum Publishing Ltd, Lancaster and Rugby.
- G. Wiedemann; Die Lehre von der Elektrizität. F. Vieweg; Braunschweig, *The Science of Electricity*, 2nd edn., 1893.
- W. Nernst, *Zeitschrift für Elektrochemie*, 1899, **6**, 41–43.
- W. Nernst, 1899, US Patent 685 730.
- T. Takahashi and O. Yamamoto, *Electrochim. Acta*, 1966, **11**, 779–789.
- T. Takahashi, *MRS Proc.*, 1988, 135, 3.
- Y. Y. Yao and J. T. Kummer, *J. Inorg. Nucl. Chem.*, 1967, **29**, 2453–2475.
- J. T. Kummer and N. Weber, *Proc. SAE Cong.*, 1967, **670179**, 1003–1028.

- 45 Joseph T. Kummer, Amm Arbor, N. W. Thermo-Electric Generator, 1969.
- 46 Bradley J N and Greene P D, *React. Wkly.*, 1966, **62**, 2069–2975.
- 47 J. N. Bradley and P. D. Greene, *Trans. Faraday Soc.*, 1967, **63**, 424–430.
- 48 S. H. B. L. K. S. Chandra, *J. Phys. D. Appl. Phys.*, 1974, **7**, 194–198.
- 49 B. Reuter and K. Hardel, *Angew. Chemie*, 2007, **72**, 138–139.
- 50 Fenton D. E.; Parker d. M. and Wright P. V., *Polymer (Guildf.)*, 1973, **14**, 589.
- 51 J. Coetzer, *J. Power Sources*, 1986, **18**, 377–380.
- 52 J. Bones R. J., Coetzer and R. C. Galloway, *J. Electrochem. so*, 1987, **134**, 2379–2382.
- 53 M. D. M. Armand, J. Chabagno, in *Fast ion transport in solids electrodes and electrolytes*, ed. G. K. S. P. Vashishta, J.N. Mundy, Lake Geneva, 1979, p. 131.
- 54 F. M. Gray, J. R. MacCallum and C. A. Vincent, *Solid State Ionics*, 1986, **18–19**, 282–286.
- 55 W. Gorecki, R. Andreani, C. Berthier, M. Armand, M. Mali, J. Roos and D. Brinkmann, *Solid State Ionics*, 1986, **18–19**, 295–299.
- 56 N. J. Dudney, J. B. Bates, R. A. Zuhr, C. F. Luck and J. D. Robertson, *Solid State Ionics*, 1992, **53–56**, 655–661.
- 57 C. F. L. J.B. Bates, N.J. Dudney, G.R. Gruzalski, R.A. Zuhr, A. Choudhury, *Solid State Ionics*, 1992, **53–56**, 647–654.
- 58 M. Armand and J. Tarascon, *Nature*, 2008, **451**, 652–657.
- 59 F. Lv, Z. Wang, L. Shi, J. Zhu, K. Edström, J. Mindemark and S. Yuan, *J. Power Sources*, 2019, **441**, 227175.
- 60 L. Liu and C. Sun, *ChemElectroChem*, 2020, **7**, 707–715.
- 61 G. Qiu and C. Sun, *New J. Chem.*, 2020, **44**, 1817–1824.
- 62 T. Ohtomo, K. A. T. O. Yuki, and M. Kawakami, 2017, U.S. Patent No. 9,577,286. Washington, DC.
- 63 Q. Hu, A. Caputo, D. R. Sadoway, 2015, U.S. Patent No. 9,203,109. Washington, DC.
- 64 S. J. Visco, Y. S. Nimon, B. D. Katz, 2014, U.S. Patent No. 8,778,522. Washington, DC.
- 65 W. Hittorf, *Ann. Phys. Chem.*, 1851, **84**, 1–28.
- 66 B. Zhang, R. Tan, L. Yang, J. Zheng, K. Zhang, S. Mo, Z. Lin and F. Pan, *Energy Storage Mater.*, 2018, **10**, 139–159.
- 67 E. Quartarone and P. Mustarelli, *Chem. Soc. Rev.*, 2011, **40**, 2525–2540.
- 68 R. C. Agrawal and G. P. Pandey, *J. Phys. D. Appl. Phys.*, 2008, **41**, 223001.
- 69 M. A. Ratner, P. Johansson and D. F. Shriver, *MRS Bull.*, 2000, **25**, 31–37.
- 70 J. B. Goodenough, *Annu. Rev. Mater. Res.*, 2003, **33**, 91–128.
- 71 X. Chen and P. M. Vereecken, *Adv. Mater. Interfaces*, 2019, **6**, 1–31.
- 72 K. M. Diederichsen, E. J. McShane and B. D. McCloskey, *ACS Energy Lett.*, 2017, **2**, 2563–2575.
- 73 Y. Kato, S. Hori, T. Saito, K. Suzuki, M. Hirayama, A. Mitsui, M. Yonemura, H. Iba and R. Kanno, *Nat. Energy*, 2016, **1**, 1–7.
- 74 P. Barai, K. Higa and V. Srinivasan, *J. Electrochem. Soc.*, 2018, **165**, A2654–A2666.
- 75 Y. G. Lee, S. Fujiki, C. Jung, N. Suzuki, N. Yashiro, R. Omoda, D. S. Ko, T. Shiratsuchi, T. Sugimoto, S. Ryu, J. H. Ku, T. Watanabe, Y. Park, Y. Aihara, D. Im and I. T. Han, *Nat. Energy*, 2020, **5**, DOI: 10.1038/s41560-020-0604-y.
- 76 K. Shigenobu, K. Dokko, M. Watanabe and K. Ueno, *Phys. Chem. Chem. Phys.*, 2020, **22**, 15214–15221.
- 77 P. G. Bruce, M. T. Hardgrave and C. A. Vincent, *Solid State Ionics*, 1992, **53–56**, 1087–1094.
- 78 L. G. Longworth, *J. Am. Chem. Soc.*, 1943, **65**, 1755–1765.
- 79 M. Kerker and W. F. Espenscheid, *J. Am. Chem. Soc.*, 1958, **80**, 776–779.
- 80 Peter G. Bruce, *Solid State Ionics*, 1988, **28–30**, 918–922.
- 81 A. Nag, M. A. Ali, A. Singh, R. Vedarajan, N. Matsumi and T. Kaneko, *J. Mater. Chem. A*, 2019, **7**, 4459–4468.
- 82 A. Ghosh, C. Wang and P. Kofinas, *J. Electrochem. Soc.*, 2010, **157**, A846.
- 83 J. Mindemark, M. J. Lacey, T. Bowden and D. Brandell, *Prog. Polym. Sci.*, 2018, **81**, 114–143.
- 84 J. Ou, G. Li and Z. Chen, *J. Electrochem. Soc.*, 2019, **166**, A1785–A1792.
- 85 D. G. Mackanic, X. Yan, Q. Zhang, N. Matsuhisa, Z. Yu, Y. Jiang, T. Manika, J. Lopez, H. Yan, K. Liu, X. Chen, Y. Cui and Z. Bao, *Nat. Commun.*, 2019, **10**, 1–11.
- 86 A. Masias, N. Felten, R. Garcia-Mendez, J. Wolfenstine and J. Sakamoto, *J. Mater. Sci.*, 2019, **54**, 2585–2600.
- 87 R. Chen, Q. Li, X. Yu, L. Chen and H. Li, *Chem. Rev.*, 2020, **120**, **14**, 6820–6877.
- 88 Z. Li, H. X. Xie, X. Y. Zhang and X. Guo, *J. Mater. Chem. A*, 2020, **8**, 3892–3900.
- 89 K. (Kelvin) Fu, Y. Gong, J. Dai, A. Gong, X. Han, Y. Yao, C. Wang, Y. Wang, Y. Chen, C. Yan, Y. Li, E. D. Wachsman and L. Hu, *Proc. Natl. Acad. Sci.*, 2016, **113**, 7094–7099.
- 90 Y. Zhu, X. He and Y. Mo, *J. Mater. Chem. A*, 2016, **4**, 3253–3266.
- 91 F. Han, Y. Zhu, X. He, Y. Mo and C. Wang, *Adv. Energy Mater.*, 2016, **6**, 1–9.
- 92 A. M. S. Myounggu Park, Xiangchun Zhang, Myoungdo Chung, Gregory B. Less, *J. Power Sources*, 2010, **195**, 7904–7929.
- 93 M. S. Islam, D. J. Driscoll, C. A. J. Fisher and P. R. Slater, *Chem. Mater.*, 2005, **17**, 5085–5092.
- 94 A. Van Der Ven and G. Ceder, *Electrochem. Solid-State Lett.*, 2000, **3**, 301–304.
- 95 A. Chroneos, B. Yildiz, A. Tarancón, D. Parfitt and J. A. Kilner, *Energy Environ. Sci.*, 2011, **4**, 2774–2789.
- 96 C. Angell, *Annu. Rev. Phys. Chem.*, 1992, **43**, 693–717.
- 97 M. Wu, B. Xu and C. Ouyang, *Chinese Phys. B*, 2015, **25**, 1–10.
- 98 L. Long, S. Wang, M. Xiao and Y. Meng, *J. Mater. Chem. A*, 2016, **4**, 10038–10039.
- 99 S. K. Fullerton-Shirey and J. K. Maranas, *Macromolecules*, 2009, **42**, 2142–2156.
- 100 D. P. T. & P. G. B. Zlatka Gadjourova, Yuri G. Andreev, *Nature*, 2001, **412**, 1–4.
- 101 C. Berthier, W. Gorecki, M. Minier, M. B. Armand, J. M. Chabagno and P. Rigaud, *Solid*, 1983, **11**, 91–95.
- 102 W. A. Henderson, N. R. Brooks and V. G. Young, *J. Am. Chem. Soc.*, 2003, **125**, 12098–12099.

- 103 W. A. Henderson and S. Passerini, *Electrochem. commun.*, 2003, **5**, 575–578.
- 104 Z. Stoeva, I. Martin-Litas, E. Staunton, Y. G. Andreev and P. G. Bruce, *J. Am. Chem. Soc.*, 2003, **125**, 4619–4626.
- 105 A. M. Christie, S. J. Lilley, E. Staunton, Y. G. Andreev and P. G. Bruce, *Nature*, 2005, **433**, 50–53.
- 106 C. Zhang, E. Staunton, Y. G. Andreev and P. G. Bruce, *J. Am. Chem. Soc.*, 2005, **127**, 18305–18308.
- 107 S. J. Lilley, Y. G. Andreev and P. G. Bruce, *J. Am. Chem. Soc.*, 2006, **128**, 12036–12037.
- 108 G. S. MacGlashan and Y. G. Andreev, *Nature*, 1999, **398**, 792–794.
- 109 K. Liu, Y. Xiang, W. Liu, F. Shi, H. Wang, Y. Cui, J. Xie, Y. Liu, A. Pei, D. Lin, Y. Gong and X. Zhang, *Nano Lett.*, 2018, **18**, 3829–3838.
- 110 B. Scrosati, F. Croce and S. Panero, *J. Power Sources*, 2001, **100**, 93–100.
- 111 R. Meziane, J. Bonnet, M. Courty, K. Djellab and M. Armand, *Electrochim. Acta*, 2011, **57**, 14–19.
- 112 J. M. G. Cowie and G. H. Spence, 1999, **123**, 233–242.
- 113 H. S. Lee, Z. F. Ma, X. Q. Yang, X. Sun and J. Mcbreen, *J. Electrochem. Soc.*, 2004, **151**, A1429–A1435.
- 114 Z. Xue, D. He and X. Xie, *J. Mater. Chem. A*, 2015, **3**, 19218–19253.
- 115 D. Golodnitsky, E. Strauss, E. Peled and S. Greenbaum, *J. Electrochem. Soc.*, 2015, **162**, A2551–A2566.
- 116 P. K. Singh, B. Bhattacharya and R. K. Nagarale, *J. Appl. Polym. Sci.*, 2010, **118**, 2976–2980.
- 117 G. X. Wang, L. Yang, J. Z. Wang, H. K. Liu and S. X. Dou, *J. Nanosci. Nanotechnol.*, 2005, **5**, 1135–1140.
- 118 C. C. Tambelli, A. C. Bloise, A. V. Rosário, E. C. Pereira, C. J. Magon and J. P. Donoso, *Electrochim. Acta*, 2002, **47**, 1677–1682.
- 119 G. B. Appetecchi, S. Scaccia and S. Passerini, *J. Electrochem. Soc.*, 2002, **147**, 4448.
- 120 E. Strauss, D. Golodnitsky, G. Ardel and E. Peled, *Electrochim. Acta*, 1998, **43**, 1315–1320.
- 121 G. M. Hou, M. Q. Zhang, Y. F. Huang and W. H. Ruan, *RSC Adv.*, 2016, **6**, 83406–83411.
- 122 L. Fan, C. W. Nan and S. Zhao, *Solid State Ionics*, 2003, **164**, 81–86.
- 123 R. J. Sengwa and S. Choudhary, *J. Alloys Compd.*, 2017, **701**, 652–659.
- 124 N. Lago, O. Garcia-Calvo, J. M. Lopezdelamo, T. Rojo and M. Armand, *ChemSusChem*, 2015, **8**, 3039–3043.
- 125 A. Sarnowska, I. Polska, L. Niedzicki, M. Marcinek and A. Zalewska, *Electrochim. Acta*, 2011, **57**, 180–186.
- 126 H. M. J. C. Pitawala, M. A. K. L. Dissanayake, V. A. Seneviratne, B. E. Mellander and I. Albinson, *J. Solid State Electrochem.*, 2008, **12**, 783–789.
- 127 J. K. Lee, Y. J. Lee, W. S. Chae and Y. M. Sung, *J. Electroceramics*, 2006, **17**, 941–944.
- 128 H. Kasemägi, M. Klintenber, A. Aabloo and J. O. Thomas, *Electrochim. Acta*, 2003, **48**, 2273–2278.
- 129 X. L. Wang, A. Mei, M. Li, Y. H. Lin and C. W. Nan, *J. Appl. Phys.*, 2007, **102**, 054907.
- 130 J. Syzdek, M. Armand, M. Marcinek, A. Zalewska, G. Zukowska and W. Wiczcerek, *Electrochim. Acta*, 2010, **55**, 1314–1322.
- 131 A. Unemoto, S. Yasaku, G. Nogami, M. Tazawa, M. Taniguchi, M. Matsuo, T. Ikeshoji and S. I. Orimo, *Appl. Phys. Lett.*, 2014, **105**, 083901.
- 132 A. Unemoto, T. Ikeshoji, S. Yasaku, M. Matsuo, V. Stavila, T. J. Udovic and S. I. Orimo, *Chem. Mater.*, 2015, **27**, 5407–5416.
- 133 S. Kim, N. Toyama, H. Oguchi, T. Sato, S. Takagi, T. Ikeshoji and S. I. Orimo, *Chem. Mater.*, 2018, **30**, 386–391.
- 134 M. Matsuo and S. I. Orimo, *Adv. Energy Mater.*, 2011, **1**, 161–172.
- 135 M. Latroche, D. Blanchard, F. Cuevas, A. El Kharbachi, B. C. Hauback, T. R. Jensen, P. E. de Jongh, S. Kim, N. S. Nazer, P. Ngene, S. ichi Orimo, D. B. Ravnsbæk and V. A. Yartys, *Int. J. Hydrogen Energy*, 2019, **44**, 7875–7887.
- 136 P. Hartwig, W. Weppner and W. Wichelhaus, *Mater. Res. Bull.*, 1979, **14**, 493–498.
- 137 T. Asano, A. Sakai, S. Ouchi, M. Sakaida, A. Miyazaki and S. Hasegawa, *Adv. Mater.*, 2018, **30**, 1–7.
- 138 Y. Tomita, H. Matsushita, K. Kobayashi, Y. Maeda and K. Yamada, *Solid State Ionics*, 2008, **179**, 867–870.
- 139 S. Stramare, V. Thangadurai and W. Weppner, *Chem. Mater.*, 2003, **15**, 3974–3990.
- 140 F. Aguesse, V. Roddatis, J. Roqueta, P. García, D. Pergolesi, J. Santiso and J. A. Kilner, *Solid State Ionics*, 2015, **272**, 1–8.
- 141 H. T. T. Le, R. S. Kalubarme, D. T. Ngo, S. Y. Jang, K. N. Jung, K. H. Shin and C. J. Park, *J. Power Sources*, 2015, **274**, 1188–1199.
- 142 O. Bohnke, C. Bohnke and J. L. J. Fourquet, *Solid State Ionics*, 1996, **91**, 21–31.
- 143 J. B. Goodenough, H. Y. Hong and J. A. Kafalas, *Mater. Res. Bull.*, 1976, **11**, 203–220.
- 144 H. Aono, E. Sugimoto, Y. Sadaoka, N. Imanaka and G. Adachi, *J. Electrochem. Soc.*, 1989, **136**, 590–591.
- 145 X. Xu, Z. Wen, X. Wu, X. Yang and Z. Gu, *J. Am. Ceram. Soc.*, 2007, **90**, 2802–2806.
- 146 C. J. Leo, B. V. R. Chowdari, G. V. S. Rao and J. L. Souquet, *Mater. Res. Bull.*, 2002, **37**, 1419–1430.
- 147 K. Hayamizu and S. Seki, *Phys. Chem. Chem. Phys.*, 2017, **19**, 23483–23491.
- 148 J. K. Feng, B. G. Yan, J. C. Liu, M. O. Lai and L. Li, *Mater. Technol.*, 2013, **28**, 276–279.
- 149 H. Y. P. Hong, *Mater. Res. Bull.*, 1978, **13**, 117–124.
- 150 J. Awaka, N. Kijima, H. Hayakawa and J. Akimoto, *J. Solid State Chem.*, 2009, **182**, 2046–2052.
- 151 V. Thangadurai, S. Narayanan and D. Pinzaru, *Chem. Soc. Rev.*, 2014, **43**, 4714–4727.
- 152 C. Cao, Z.-B. Li, X.-L. Wang, X.-B. Zhao and W.-Q. Han, *Front. Energy Res.*, 2014, **2**, 1–10.
- 153 Y. Li, J. T. Han, C. A. Wang, H. Xie and J. B. Goodenough, *J. Mater. Chem.*, 2012, **22**, 15357–15361.
- 154 R. Murugan, V. Thangadurai and W. Weppner, *Angew. Chemie - Int. Ed.*, 2007, **46**, 7778–7781.
- 155 Y. Lu, X. Meng, J. A. Alonso, M. T. Fernández-Díaz and C. Sun, *ACS Appl. Mater. Interfaces*, 2019, **11**, 2042–2049.
- 156 S. Siculo and K. Albe, *J. Power Sources*, 2016, **331**, 382–390.

- 157 N. J. Dudney, *Mater. Sci. Eng. B Solid-State Mater. Adv. Technol.*, 2005, **116**, 245–249.
- 158 H. Tak, T. Mun, C. Park, S. Wan and H. Young, *J. Power Sources*, 2013, **244**, 641–645.
- 159 L. Le Van-jodin, F. Ducroquet, F. Sabary and I. Chevalier, *Solid State Ionics*, 2013, **253**, 151–156.
- 160 R. Koerver, I. Aygün, T. Leichtweiß, C. Dietrich, W. Zhang, J. O. Binder, P. Hartmann, W. G. Zeier and J. Janek, *Chem. Mater.*, 2017, **29**, 5574–5582.
- 161 Y. Inaguma, C. Liquan, M. Itoh, T. Nakamura, T. Uchida, H. Ikuta and M. Wakihara, *Solid State Commun.*, 1993, **86**, 689–693.
- 162 R. J. Chen, W. Liang, H. Q. Zhang, F. Wu and L. Li, *Chinese Sci. Bull.*, 2012, **57**, 4199–4204.
- 163 Y. Yoon, J. Kim, C. Park and D. Shin, *J. Ceram. Process. Res.*, 2013, **14**, 563–566.
- 164 J. S. Thokchom and B. Kumar, *J. Power Sources*, 2010, **195**, 2870–2876.
- 165 C. Bernuy-Lopez, W. Manalastas, J. M. Lopez Del Amo, A. Aguadero, F. Aguesse and J. A. Kilner, *Chem. Mater.*, 2014, **26**, 3610–3617.
- 166 Y. Deng, C. Eames, J. N. Chotard, F. Laleire, V. Seznec, S. Emge, O. Pecher, C. P. Grey, C. Masquelier and M. S. Islam, *J. Am. Chem. Soc.*, 2015, **137**, 9136–9145.
- 167 P. G. Bruce and A. R. West, *J. Solid State Chem.*, 1982, **44**, 354–365.
- 168 S. Taminato, T. Okumura, T. Takeuchi and H. Kobayashi, *Solid State Ionics*, 2018, **326**, 52–57.
- 169 M. A. K. L. Dissanayake, R. P. Gunawardane, A. R. West, G. K. R. Senadeera, P. W. S. K. Bandaranayake and M. A. Careem, *Solid State Ionics*, 1993, **62**, 217–223.
- 170 X. Yu, *J. Electrochem. Soc.*, 1997, **144**, 524.
- 171 T. Fujibayashi, Y. Kubota, K. Iwabuchi and N. Yoshii, *AIP Adv.*, 2017, **7**, 085110.
- 172 L. I. Hong and X. U. Xiaoxiong, *Energy Stor. Sci. Technol.*, 2016, **5**, 607–614.
- 173 S. Chua, R. Fang, Z. Sun, M. Wu, Z. Gu, Y. Wang, J. N. Hart, N. Sharma, F. Li and D. W. Wang, *Chem. - A Eur. J.*, 2018, **24**, 18180–18203.
- 174 Z. He, L. Chen, B. Zhang, Y. Liu and L. Z. Fan, *J. Power Sources*, 2018, **392**, 232–238.
- 175 K. Vignarooban, M. A. K. L. Dissanayake, I. Albinsson and B. E. Mellander, *Solid State Ionics*, 2014, **266**, 25–28.
- 176 Z. Yi, L. P. Zhu, Y. Y. Xu, X. N. Gong and B. K. Zhu, *J. Memb. Sci.*, 2011, **385–386**, 57–66.
- 177 F. Croce, G. B. Appetecchi, L. Persi and B. Scrosati, *Nature*, 1998, **394**, 456–458.
- 178 A. C. Balazs, T. Emrick and T. P. Russell, *Science*, 2006, **314**, 1107–1110.
- 179 S. Jung, D. W. Kim, S. D. Lee, M. Cheong, D. Q. Nguyen, B. W. Cho and H. S. Kim, *Bull. Korean Chem. Soc.*, 2009, **30**, 2355–2361.
- 180 S. Rajendran and T. Uma, *Ionics (Kiel)*, 2000, **6**, 288–293.
- 181 A. D. Epifanio, F. S. Fiory, S. Licoccia, E. Traversa and B. Scrosati, *J. Appl. Electrochem.*, 2004, **43**, 403–408.
- 182 H. M. Xiong, Z. D. Wang, D. P. Xie, L. Cheng and Y. Y. Xia, *J. Mater. Chem.*, 2006, **16**, 1345–1349.
- 183 J. E. Weston and B. C. H. Steele, *Solid State Ionics*, 1982, **7**, 75–79.
- 184 V Aravindan and P. Vickraman, *J. Phys. D. Appl. Phys.*, 2007, **40**, 6754–6759.
- 185 D. Lin, W. Liu, Y. Liu, H. R. Lee, P. C. Hsu, K. Liu and Y. Cui, *Nano Lett.*, 2016, **16**, 459–465.
- 186 X. Fu, D. Yu, J. Zhou, S. Li, X. Gao, Y. Han, P. Qi, X. Feng and B. Wang, *CrystEngComm*, 2016, **18**, 4236–4258.
- 187 U. H. Choi, *Chem. Mater.*, 2017, **29**, 4401–4410.
- 188 M. Moreno, R. Quijada, M. A. Santa Ana, E. Benavente, P. Gomez-Romero and G. González, *Electrochim. Acta*, 2011, **58**, 112–118.
- 189 J. K. Yasuhide Matsuo, *Solid State Ionics*, 1995, **79**, 295–299.
- 190 C. Capiglia, P. Mustarelli, E. Quartarone, C. Tomasi and A. Magistris, *Solid State Ionics*, 1999, **118**, 73–79.
- 191 Y. Liu, J. Y. Lee and L. Hong, *J. Power Sources*, 2002, **109**, 507–514.
- 192 S. T. Guoxin Jiang, Seiji Maeda, Yoichiro Saito and T. Sakai, *J. Electrochem. Soc.*, 2005, **152**, A767–A773.
- 193 D. Shanmukaraj and R. Murugan, *J. Power Sources*, 2005, **149**, 90–95.
- 194 D. Shanmukaraj, G. X. Wang, H. K. Liu and R. Murugan, *Polym. Bull.*, 2008, **60**, 351–361.
- 195 Y. Zhang, X. Wang, W. Feng, Y. Zhen, P. Zhao, Z. Cai and L. Li, *Ionics (Kiel)*, 2019, **25**, 1471–1480.
- 196 M. Sasikumar, M. Raja, R. H. Krishna, A. Jagadeesan, P. Sivakumar and S. Rajendran, *J. Phys. Chem. C*, 2018, **122**, 25741–25752.
- 197 L. Lee, S. J. Park and S. Kim, *Solid State Ionics*, 2013, **234**, 19–24.
- 198 T. Itoh, S. Horii, T. Uno, M. Kubo and O. Yamamoto, *Electrochim. Acta*, 2004, **50**, 271–274.
- 199 H. Y. Sun, Y. Takeda, N. Imanishi, O. Yamamoto and H. J. Sohn, *J. Electrochem. Soc.*, 2000, **147**, 2462–2467.
- 200 R. Jayaraman, P. Vickraman, N. M. V Subramanian and A. S. Justin, *AIP Conference Proceedings*, 2016, **1731**, 140028.
- 201 J. Xi and X. Tang, *Chem. Phys. Lett.*, 2004, **393**, 271–276.
- 202 J. Xi, X. Qiu, S. Zheng and X. Tang, *Polymer (Guildf.)*, 2005, **46**, 5702–5706.
- 203 F. Croce, L. Settini and B. Scrosati, *Electrochem. commun.*, 2006, **8**, 364–368.
- 204 F. Croce, S. Sacchetti and B. Scrosati, *J. Power Sources*, 2006, **162**, 685–689.
- 205 A. Wang, H. Xu, X. Liu, S. Wang, Q. Zhou, J. Chen and L. Zhang, *Compos. Sci. Technol.*, 2017, **152**, 68–75.
- 206 G. B. Appetecchi and S. Passerini, *Electrochim. Acta*, 2000, **45**, 2139–2145.
- 207 B. Mi, *Science*, 2014, **343**, 740–742.
- 208 W. J. Yuan Peng, Yanshuo Li, Yujie Ban, Hua Jin and W. Y. Xinlei Liu, *Science*, 2014, **346**, 6215.
- 209 S. M. Kuznicki, V. A. Bell, S. Nair, H. W. Hillhouse, R. M. Jacubinas, C. M. Braunbarth, B. H. Toby and M. Tsapatsis, *Nature*, 2001, **412**, 720–724.
- 210 A. Corma, M. J. Díaz-Cabãas, J. L. Jordá, C. Martínez and M. Moliner, *Nature*, 2006, **443**, 842–845.
- 211 J. Xi and X. Tang, *Electrochim. Acta*, 2006, **51**, 4765–4770.

- 212 J. Xi, X. Qiu, J. Wang, Y. Bai, W. Zhu and L. Chen, *J. Power Sources*, 2006, **158**, 627–634.
- 213 J. Xi, X. Qiu, W. Zhu and X. Tang, *Microporous Mesoporous Mater.*, 2006, **88**, 1–7.
- 214 A. Corma, *Chem. Rev.*, 1997, **97**, 2373–2419.
- 215 C. S. Cundy and P. A. Cox, *Chem. Rev.*, 2003, **103**, 663–701.
- 216 M. J. Reddy, P. P. Chu and U. V. S. Rao, *J. Power Sources*, 2006, **158**, 614–619.
- 217 J. Mohanta, U. P. Singh, S. K. Panda and S. Si, *Adv. Nat. Sci. Nanosci. Nanotechnol.*, 2016, **7**, 1–8.
- 218 X. Wang, A. Mei, M. Li, Y. Lin and C. Nan, *Solid State Ionics* **177**, 2006, **177**, 1287–1291.
- 219 H. K. T. Y. Tsai and S. Chao, *Solid State Ionics* **176**, 2005, **176**, 1261–1270.
- 220 S. Wang, Q. Xuan, Y. Sheng, Y. Wang, H. Yan, Z. Gang, X. Lin and Y. Wing, *Electrochim. Acta*, 2017, **245**, 1010–1022.
- 221 Y. Li, K. Wong and K. Ng, *Chem. Commun.*, 2016, **52**, 4369–4372.
- 222 S. S. Moganty, N. Jayaprakash, J. L. Nugent, J. Shen and L. A. Archer, *Angew. Chemie Int. Ed.*, 2010, **49**, 9158–9161.
- 223 Y. Tominaga, S. Asai, M. Sumita, S. Panero and B. Scrosati, *J. of Power Sources*, 2005, **146**, 402–406.
- 224 Y. Zhang, Y. Zhao, D. Gosselink and P. Chen, *Ionics (Kiel)*, 2015, **21**, 381–385.
- 225 N. Zhang, A. ling Zhang, Q. fang Liu, M. Zhang, Q. Li and F. fang Li, *Ionics (Kiel)*, 2018, **24**, 3805–3813.
- 226 R. J. Sengwa, S. Choudhary and P. Dhatarwal, *Ionics (Kiel)*, 2015, **21**, 95–109.
- 227 T. Dam, N. K. Karan, R. Thomas, D. K. Pradhan and R. S. Katiyar, *Ionics (Kiel)*, 2015, **21**, 401–410.
- 228 S. R. Mohapatra, A. K. Thakur and R. N. P. Choudhary, *J. Power Sources*, 2009, **191**, 601–613.
- 229 S. Choudhary, A. Bald, R. J. Sengwa, D. Chęcińska-Majak and K. Klimaszewski, *J. Appl. Polym. Sci.*, 2015, **132**, 18–27.
- 230 Y. Ma, L. B. Li, G. X. Gao, X. Y. Yang and Y. You, *Electrochim. Acta*, 2016, **187**, 535–542.
- 231 M. Xie, L. Li, K. Yuan, Y. Ma and B. Liu, *J. Mater. Sci. Mater. Electron.*, 2019, **30**, 2030–2036.
- 232 E. M. Masoud, *Ionics (Kiel)*, 2019, **25**, 2645–2656.
- 233 P. Dhatarwal, R. J. Sengwa and S. Choudhary, *SN Appl. Sci.*, 2019, **1**, 112.
- 234 S. Kim, E. J. Hwang, Y. Jung, M. Han and S. J. Park, *Colloids Surfaces A Physicochem. Eng. Asp.*, 2008, **313–314**, 216–219.
- 235 S. Kim and S. J. Park, *Solid State Ionics*, 2007, **178**, 973–979.
- 236 L. Chen, W. Li, L. Z. Fan, C. W. Nan and Q. Zhang, *Adv. Funct. Mater.*, 2019, **1901047**, 1–11.
- 237 M. Moreno, M. A. S. Ana, G. Gonzalez and E. Benavente, *Electrochim. Acta*, 2010, **55**, 1323–1327.
- 238 Y. Tominaga and M. Endo, *Electrochim. Acta*, 2013, **113**, 361–365.
- 239 S. Hua, M. Jing, C. Han, H. Yang, H. Chen, F. Chen, L. Chen, B. Ju, F. Tu and X. Shen, *Int. J. Energy Res.*, 2019, **43**, 7296–7305.
- 240 W. Liu, D. Lin, J. Sun, G. Zhou and Y. Cui, *ACS Nano*, 2016, **10**, 11407–11413.
- 241 F. Pignatelli, M. Romero, R. Faccio, L. Fernández-Werner and A. W. Mombrú, *J. Phys. Chem. C*, 2018, **122**, 1492–1499.
- 242 O. Sheng, C. Jin, J. Luo, H. Yuan, H. Huang, Y. Gan, J. Zhang, Y. Xia, C. Liang and W. Zhang, *Nano Lett.*, 2018, **18**, 3104–3112.
- 243 Q. Zhu, X. Wang and J. D. Miller, *ACS Appl. Mater. Interfaces*, 2019, **11**, 8954–8960.
- 244 P. Pongsuk and J. Pumchusak, *Mater. Today Proc.*, 2019, **17**, 1956–1963.
- 245 J. Zhang, X. Huang, H. Wei, J. Fu, Y. Huang and X. Tang, *J. Solid State Electrochem.*, 2012, **16**, 101–107.
- 246 Z. Gadjourova, D. Martin y Marero, K. H. Andersen, Y. G. Andreev and P. G. Bruce, *Chem. Mater.*, 2001, **13**, 1282–1285.
- 247 D. M. Schaeztl, P. Li, N. Chaudhari, G. H. Bernstein and S. K. Fullerton-Shirey, *J. Phys. Chem. C*, 2014, **118**, 18836–18845.
- 248 W. Jia, Z. Li, Z. Wu, L. Wang, B. Wu, Y. Wang, Y. Cao and J. Li, *Solid State Ionics*, 2018, **315**, 7–13.
- 249 J. Shim, D. G. Kim, H. J. Kim, J. H. Lee, J. H. Baik and J. C. Lee, *J. Mater. Chem. A*, 2014, **2**, 13873–13883.
- 250 S. Gao, J. Zhong, G. Xue and B. Wang, *J. Memb. Sci.*, 2014, **470**, 316–322.
- 251 S. N. Banitaba, D. Semnani, E. Heydari-Soureshjani, B. Rezaei and A. A. Ensafi, *Polym. Int.*, 2019, **68**, 1787–1794.
- 252 B. Wu, L. Wang, Z. Li, M. Zhao, K. Chen, S. Liu, Y. Pu and J. Li, *J. Electrochem. Soc.*, 2016, **163**, A2248–A2252.
- 253 C.-S. Liao and W.-B. Ye, *J. Polym. Res.*, 2003, **10**, 241–246.
- 254 C.-S. Liao and W.-B. Ye, *Mater. Chem. Phys.*, 2004, **88**, 84–89.
- 255 Z. Huang, S. Wang, S. Kota, Q. Pan, M. W. Barsoum and C. Y. Li, *Polymer (Guildf)*, 2016, **102**, 119–126.
- 256 Q. Pan, Y. Zheng, S. Kota, W. Huang, S. Wang, H. Qi, S. Kim, Y. Tu, M. W. Barsoum and C. Y. Li, *Nanoscale Adv.*, 2019, **1**, 395–402.
- 257 W. Tang, S. Tang, C. Zhang, Q. Ma, Q. Xiang, Y. Yang and J. Luo, *Adv. Energy Mater.*, 2018, **8**, 1800866.
- 258 B. Wang, M. Tang, Y. Wu, Y. Chen, C. Jiang, S. Zhuo, S. Zhu and C. Wang, *ACS Appl. Energy Mater.*, 2019, **2**, 5909–5916.
- 259 W. Zhang, Q. Yi, S. Li and C. Sun, *J. Power Sources*, 2020, **450**, 227710.
- 260 Z. Li, H. M. Huang, J. K. Zhu, J. F. Wu, H. Yang, L. Wei and X. Guo, *ACS Appl. Mater. Interfaces*, 2019, **11**, 784–791.
- 261 W. Wang, E. Yi, A. J. Fici, R. M. Laine and J. Kieffer, *J. Phys. Chem. C*, 2017, **121**, 2563–2573.
- 262 J. Zhang, N. Zhao, M. Zhang, Y. Li, P. K. Chu, X. Guo, Z. Di, X. Wang and H. Li, *Nano Energy*, 2016, **28**, 447–454.
- 263 X. Zhang, T. Liu, S. Zhang, X. Huang, B. Xu, Y. Lin, B. Xu, L. Li, C. W. Nan and Y. Shen, *J. Am. Chem. Soc.*, 2017, **139**, 13779–13785.
- 264 J. Zheng, P. Wang, H. Liu and Y.-Y. Hu, *ACS Appl. Energy Mater.*, 2019, **2**, 1452–1459.
- 265 Z. Huang, W. Pang, P. Liang, Z. Jin, N. Grundish, Y. Li and C. A. Wang, *J. Mater. Chem. A*, 2019, **7**, 16425–16436.
- 266 W. Li, C. Sun, J. Jin, Y. Li, C. Chen and Z. Wen, *J. Mater. Chem. A*, 2019, **7**, 27304–27312.
- 267 J. Zheng, M. Tang and Y. Y. Hu, *Angew. Chemie - Int. Ed.*, 2016, **55**, 12538–12542.
- 268 J. Zheng and Y. Y. Hu, *ACS Appl. Mater. Interfaces*, 2018, **10**, 4113–4120.
- 269 L. Chen, Y. Li, S. P. Li, L. Z. Fan, C. W. Nan and J. B. Goodenough, *Nano Energy*, 2018, **46**, 176–184.

- 270 J. Zhang, X. Zang, H. Wen, T. Dong, J. Chai, Y. Li, B. Chen, J. Zhao, S. Dong and J. Ma, *J. Mater. Chem. A*, 2017, **5**, 4940–4948.
- 271 X. Zhang, T. Liu, S. Zhang, X. Huang, B. Xu, Y. Lin, B. Xu, L. Li, C.-W. Nan and Y. Shen, *J. Am. Chem. Soc.*, 2017, **139**, 13779–13785.
- 272 L. Liu, L. Chu, B. Jiang and M. Li, *Solid State Ionics*, 2019, **331**, 89–95.
- 273 B. Chen, Z. Huang, X. Chen, Y. Zhao, Q. Xu, P. Long, S. Chen and X. Xu, *Electrochim. Acta*, 2016, **210**, 905–914.
- 274 Y. Zhao, C. Wu, G. Peng, X. Chen, X. Yao, Y. Bai, F. Wu, S. Chen and X. Xu, *J. Power Sources*, 2016, **301**, 47–53.
- 275 H. Huo, J. Sun, C. chen, X. Meng, M. He, N. Zhao and X. Guo, *J. Power Sources*, 2018, **383**, 150–156.
- 276 Y. C. Jung, S. M. Lee, J. H. Choi, S. S. Jang and D. W. Kima, *J. Electrochem. Soc.*, 2015, **162**, A704–A710.
- 277 Y. J. Wang, Y. Pan and D. Kim, *J. Power Sources*, 2006, **159**, 690–701.
- 278 W. Zhang, J. Nie, F. Li, Z. L. Wang and C. Sun, *Nano Energy*, 2018, **45**, 413–419.
- 279 J. Zhang, C. Zheng, J. Lou, Y. Xia, C. Liang, H. Huang, Y. Gan, X. Tao and W. Zhang, *J. Power Sources*, 2019, **412**, 78–85.
- 280 X. Ban, W. Zhang, N. Chen and C. Sun, *J. Phys. Chem. C*, 2018, **122**, 9852–9858.
- 281 J. Zheng, M. Tang and Y. Hu, *Angew. Chemie Int. Ed.*, 2016, **55**, 12538–12542.
- 282 J. Hye, P. N. Didwal, J. Min, D. Rye and C. Park, *J. Memb. Sci.*, 2020, **595**, 117538.
- 283 W. Zha, F. Chen, D. Yang, Q. Shen and L. Zhang, *J. Power Sources*, 2018, **397**, 87–94.
- 284 Q. Guo, Y. Han, H. Wang, S. Xiong, Y. Li, S. Liu and K. Xie, *ACS Appl. Mater. Interfaces*, 2017, **9**, 41837–41844.
- 285 L. Yang, Z. Wang, Y. Feng, R. Tan, Y. Zuo, R. Gao, Y. Zhao, L. Han, Z. Wang and F. Pan, *Adv. Energy Mater.*, 2017, **7**, 1–9.
- 286 S. Song, Y. Wu, W. Tang, F. Deng, J. Yao, Z. Liu, R. Hu, Alamusi, Z. Wen, L. Lu and N. Hu, *ACS Sustain. Chem. Eng.*, 2019, **7**, 7163–7170.
- 287 B. Li, Q. Su, L. Yu, D. Wang, S. Ding, M. Zhang, G. Du and B. Xu, *ACS Appl. Mater. Interfaces*, 2019, **11**, 42206–42213.
- 288 L. Zhu, P. Zhu, S. Yao, X. Shen and F. Tu, *Int. J. Energy Res.*, 2019, **43**, 4854–4866.
- 289 P. Zhu, C. Yan, M. Dirican, J. Zhu, J. Zang, R. K. Selvan, C.-C. Chung, H. Jia, Y. Li, Y. Kiyak, N. Wu and X. Zhang, *J. Mater. Chem. A*, 2018, **6**, 4279–4285.
- 290 Y. Liang, L. Ji, B. Guo, Z. Lin, Y. Yao, Y. Li, M. Alcoutlabi, Y. Qiu and X. Zhang, *J. Power Sources*, 2011, **196**, 436–441.
- 291 L. Zhu, P. Zhu, Q. Fang, M. Jing, X. Shen and L. Yang, *Electrochim. Acta*, 2018, **292**, 718–726.
- 292 Y. Li, W. Zhang, Q. Dou, K. W. Wong and K. M. Ng, *J. Mater. Chem. A*, 2019, **7**, 3391–3398.
- 293 T. Yang, J. Zheng, Q. Cheng, Y.-Y. Hu and C. K. Chan, *ACS Appl. Mater. Interfaces*, 2017, **9**, 21773–21780.
- 294 W. Liu, N. Liu, J. Sun, P.-C. Hsu, Y. Li, H.-W. Lee and Y. Cui, *Nano Lett.*, 2015, **15**, 2740–2745.
- 295 Z. Wan, D. Lei, W. Yang, C. Liu, K. Shi, X. Hao, L. Shen, W. Lv, B. Li, Q.-H. Yang, F. Kang and Y.-B. He, *Adv. Funct. Mater.*, 2019, **29**, 1805301.
- 296 Y. Li, H. Xu, P. H. Chien, N. Wu, S. Xin, L. Xue, K. Park, Y. Y. Hu and J. B. Goodenough, *Angew. Chemie Int. Ed.*, 2018, **57**, 8587–8591.
- 297 Y. Li, B. Xu, H. Xu, H. Duan, X. Lü, S. Xin, W. Zhou, L. Xue, G. Fu, A. Manthiram and J. B. Goodenough, *Angew. Chemie - Int. Ed.*, 2017, **56**, 753–756.
- 298 W. Zhou, Y. Zhu, N. Grundish, Sen Xin, S. Wang, Y. You, N. Wu, J. Gao, Z. Cui, Y. Li and J. B. Goodenough, *Nano Energy*, 2018, **53**, 926–931.
- 299 W. Zhou, S. Wang, Y. Li, S. Xin, A. Manthiram and J. B. Goodenough, *J. Am. Chem. Soc.*, 2016, **138**, 9385–9388.
- 300 S. Sen Chi, Y. Liu, N. Zhao, X. Guo, C. W. Nan and L. Z. Fan, *Energy Storage Mater.*, 2019, **17**, 309–316.
- 301 J. Liang, Q. Sun, Y. Zhao, Y. Sun, C. Wang, W. Li, M. Li, D. Wang, X. Li, Y. Liu, K. Adair, R. Li, L. Zhang, R. Yang, S. Lu, H. Huang and X. Sun, *J. Mater. Chem. A*, 2018, **6**, 23712–23719.
- 302 B. Shen, T. W. Zhang, Y. C. Yin, Z. X. Zhu, L. L. Lu, C. Ma, F. Zhou and H. Bin Yao, *Chem. Commun.*, 2019, **55**, 7703–7706.
- 303 B. Liu, Y. Gong, K. Fu, X. Han, Y. Yao, G. Pastel, C. Yang, H. Xie, E. D. Wachsman and L. Hu, *ACS Appl. Mater. Interfaces*, 2017, **9**, 18809–18815.
- 304 W. Luo, Y. Gong, Y. Zhu, Y. Li, Y. Yao, Y. Zhang, K. K. Fu, G. Pastel, C. F. Lin, Y. Mo, E. D. Wachsman and L. Hu, *Adv. Mater.*, 2017, **29**, 1–7.
- 305 H. Duan, Y. X. Yin, Y. Shi, P. F. Wang, X. D. Zhang, C. P. Yang, J. L. Shi, R. Wen, Y. G. Guo and L. J. Wan, *J. Am. Chem. Soc.*, 2018, **140**, 82–85.
- 306 K. Fu, Y. Gong, G. T. Hitz, D. W. McOwen, Y. Li, S. Xu, Y. Wen, L. Zhang, C. Wang, G. Pastel, J. Dai, B. Liu, H. Xie, Y. Yao, E. D. Wachsman and L. Hu, *Energy Environ. Sci.*, 2017, **10**, 1568–1575.
- 307 Z. Zhang, Y. Zhao, S. Chen, D. Xie, X. Yao, P. Cui and X. Xu, *J. Mater. Chem. A*, 2017, **5**, 16984–16993.
- 308 H. Huo, Y. Chen, J. Luo, X. Yang, X. Guo and X. Sun, *Adv. Energy Mater.*, 2019, **9**, 1–8.
- 309 H. Duan, M. Fan, W. P. Chen, J. Y. Li, P. F. Wang, W. P. Wang, J. L. Shi, Y. X. Yin, L. J. Wan and Y. G. Guo, *Adv. Mater.*, 2019, **31**, 1–7.
- 310 J. Y. Liang, X. X. Zeng, X. D. Zhang, T. T. Zuo, M. Yan, Y. X. Yin, J. L. Shi, X. W. Wu, Y. G. Guo and L. J. Wan, *J. Am. Chem. Soc.*, 2019, **141**, 9165–9169.
- 311 S. Yu, S. Schmohl, Z. Liu, M. Hoffmeyer, N. Schön, F. Hausen, H. Tempel, H. Kungl, H. D. Wiemhöfer and R. A. Eichel, *J. Mater. Chem. A*, 2019, **7**, 3882–3894.
- 312 W. Zhou, Z. Wang, Y. Pu, Y. Li, S. Xin, X. Li, J. Chen and J. B. Goodenough, *Adv. Mater.*, 2019, **31**, 1–7.
- 313 J. Bae, Y. Li, J. Zhang, X. Zhou, F. Zhao, Y. Shi, J. B. Goodenough and G. Yu, *Angew. Chemie Int. Ed.*, 2018, **57**, 2096–2100.
- 314 I. Jayasekara, M. Poyner and D. Teeters, *Electrochim. Acta*, 2017, **247**, 1147–1154.
- 315 X. Wang, Y. Zhang, X. Zhang, T. Liu, Y. H. Lin, L. Li, Y. Shen and C. W. Nan, *ACS Appl. Mater. Interfaces*, 2018, **10**, 24791–24798.

- 316 P. Yao, B. Zhu, H. Zhai, X. Liao, Y. Zhu, W. Xu, Q. Cheng, C. Jayyosi, Z. Li, J. Zhu, K. M. Myers, X. Chen and Y. Yang, *Nano Lett.*, 2018, **18**, 6113–6120.
- 317 D. Li, L. Chen, T. Wang and L. Z. Fan, *ACS Appl. Mater. Interfaces*, 2018, **10**, 7069–7078.
- 318 Y. Gong, K. Fu, S. Xu, J. Dai, T. R. Hamann, L. Zhang, G. T. Hitz, Z. Fu, Z. Ma, D. W. McOwen, X. Han, L. Hu and E. D. Wachsman, *Mater. Today*, 2018, **21**, 594–601.
- 319 J. Bae, Y. Li, F. Zhao, X. Zhou, Y. Ding and G. Yu, *Energy Storage Mater.*, 2018, **15**, 46–52.
- 320 Z. Li, W. X. Sha and X. Guo, *ACS Appl. Mater. Interfaces*, 2019, **11**, 26920–26927.
- 321 D. Lin, P. Y. Yuen, Y. Liu, W. Liu, N. Liu, R. H. Dauskardt and Y. Cui, *Adv. Mater.*, 2018, **30**, 1–8.
- 322 C. Wang, U. S. Kasavajjula, X. Zhang and A. J. Appleby, *J. Electrochem. Soc.*, 2005, **152**, A205–A209.
- 323 W. Tang, S. Tang, X. Guan, X. Zhang, Q. Xiang and J. Luo, *Adv. Funct. Mater.*, 2019, **29**, 1–7.
- 324 P. G. B. Stefanie Zekoll, Cassian Marriner-Edwards, A. K. Ola Hekselman, Jitti Kasemchainan, Christian Kuss, David E. J. Armstrong, Dongyu Cai, Robert J. Wallace, Felix H. Richter, Job H. J. Thijssen, *Energy Environ. Sci.*, 2018, **11**, 185–201.
- 325 A. P. Katsoulidis, D. Antypov, G. F. S. Whitehead, E. J. Carrington, D. J. Adams, N. G. Berry, G. R. Darling, M. S. Dyer and M. J. Rosseinsky, *Nature*, 2019, **565**, 213–217.
- 326 H. Furukawa, N. Ko, Y. B. Go, N. Aratani, S. B. Choi, E. Choi, A. Ö. Yazaydin, R. Q. Snurr, M. O’Keeffe, J. Kim and O. M. Yaghi, *Science*, 2010, **329**, 424–428.
- 327 H. Furukawa, K. E. Cordova, M. O’Keeffe and O. M. Yaghi, *Science*, 2013, **341**, 1230444.
- 328 M. Zhao, K. Yuan, Y. Wang, G. Li, J. Guo, L. Gu, W. Hu, H. Zhao and Z. Tang, *Nature*, 2016, **539**, 76–80.
- 329 K. Shen, L. Zhang, X. Chen, L. Liu, D. Zhang, Y. Han, J. Chen, J. Long, R. Luque, Y. Li and B. Chen, *Science*, 2018, **359**, 206–210.
- 330 J. A. R. Xueqian Kong, Hexiang Deng, Fangyong Yan, Jihan Kim, Joseph A. Swisher, Berend smit, Omar M. Yaghi, *Science*, 2013, **341**, 882–885.
- 331 H. C. Zhou, J. R. Long and O. M. Yaghi, *Chem. Rev.*, 2012, **112**, 673–674.
- 332 J. P. Zhang, Y. B. Zhang, J. Bin Lin and X. M. Chen, *Chem. Rev.*, 2012, **112**, 1001–1033.
- 333 H. Bin Wu and X. W. Lou, *Sci. Adv.*, 2017, **3**, 1–17.
- 334 C. Yuan, J. Li, P. Han, Y. Lai, Z. Zhang and J. Liu, *J. Power Sources*, 2013, **240**, 653–658.
- 335 H. Huo, B. Wu, T. Zhang, X. Zheng, L. Ge, T. Xu, X. Guo and X. Sun, *Energy Stor. Mater.*, 2019, **18**, 59–67.
- 336 Z. Wang, S. Wang, A. Wang, X. Liu, J. Chen, Q. Zeng, L. Zhang, W. Liu and L. Zhang, *J. Mater. Chem. A*, 2018, **6**, 17227–17234.
- 337 C. Gerbaldi, J. R. Nair, M. A. Kulandainathan, R. S. Kumar, C. Ferrara, P. Mustarelli and A. M. Stephan, *J. Mater. Chem. A*, 2014, **2**, 9948–9954.
- 338 N. Angulakshmi, R. S. Kumar, M. A. Kulandainathan and A. M. Stephan, *J. Phys. Chem. C*, 2014, **118**, 24240–24247.
- 339 R. Senthil Kumar, M. Raja, M. Anbu Kulandainathan and A. Manuel Stephan, *RSC Adv.*, 2014, **4**, 26171–26175.
- 340 L. Shen, H. Bin Wu, F. Liu, J. L. Brosmer, G. Shen, X. Wang, J. I. Zink, Q. Xiao, M. Cai, G. Wang, Y. Lu and B. Dunn, *Adv. Mater.*, 2018, **30**, 1–8.
- 341 B. M. Wiers, M. L. Foo, N. P. Balsara and J. R. Long, *J. Am. Chem. Soc.*, 2011, **133**, 14522–14525.
- 342 S. S. Park, Y. Tulchinsky and M. Dinca, *J. Am. Chem. Soc.*, 2017, **139**, 13260–13263.
- 343 R. Ameloot, M. Aubrey, B. M. Wiers, A. P. Gómora-Figueroa, S. N. Patel, N. P. Balsara and J. R. Long, *Chem. - A Eur. J.*, 2013, **19**, 5533–5536.
- 344 J. F. Wu and X. Guo, *Small*, 2019, **15**, 1–7.
- 345 J. F. Wu and X. Guo, *J. Mater. Chem. A*, 2019, **7**, 2653–2659.
- 346 Q. Xu, X. Zhang, S. Zeng, L. Bai and S. Zhang, *ACS Sustain. Chem. Eng.*, 2019, **7**, 7892–7899.
- 347 K. Fujie, R. Ikeda, K. Otsubo, T. Yamada and H. Kitagawa, *Chem. Mater.*, 2015, **27**, 7355–7361.
- 348 D. E. Mathew, S. Gopi, M. Kathiresan, A. M. Stephan and S. Thomas, *Electrochim. Acta*, 2019, **319**, 189–200.
- 349 S. Suriyakumar, S. Gopi, M. Kathiresan, S. Bose, E. B. Gowd, J. R. Nair, N. Angulakshmi, G. Meligrana, F. Bella, C. Gerbaldi and A. M. Stephan, *Electrochim. Acta*, 2018, **285**, 355–364.
- 350 Z. Wang, R. Tan, H. Wang, L. Yang, J. Hu, H. Chen and F. Pan, *Adv. Mater.*, 2018, **30**, 1–7.
- 351 S. Bai, Y. Sun, J. Yi, Y. He, Y. Qiao and H. Zhou, *Joule*, 2018, **2**, 2117–2132.
- 352 J. H. Park, K. Suh, M. R. Rohman, W. Hwang, M. Yoon and K. Kim, *Chem. Commun.*, 2015, **51**, 9313–9316.
- 353 D. A. Vazquez-Molina, G. S. Mohammad-Pour, C. Lee, M. W. Logan, X. Duan, J. K. Harper and F. J. Uribe-Romo, *J. Am. Chem. Soc.*, 2016, **138**, 9767–9770.
- 354 K. Zhang, B. Zhang, M. Weng, J. Zheng, S. Li and F. Pan, *Phys. Chem. Chem. Phys.*, 2019, **21**, 9883–9888.
- 355 Y. Du, H. Yang, J. M. Whiteley, S. Wan, Y. Jin, S. H. Lee and W. Zhang, *Angew. Chemie Int. Ed.*, 2016, **55**, 1737–1741.
- 356 Y. Zhang, J. Duan, D. Ma, P. Li, S. Li, H. Li, J. Zhou, X. Ma, X. Feng and B. Wang, *Angew. Chemie Int. Ed.*, 2017, **56**, 16313–16317.
- 357 Y. Hu, N. Dunlap, S. Wan, S. Lu, S. Huang, I. Sellinger, M. Ortiz, Y. Jin, S. H. Lee and W. Zhang, *J. Am. Chem. Soc.*, 2019, **141**, 7518–7525.
- 358 D. Dong, H. Zhang, B. Zhou, Y. Sun, H. Zhang, M. Cao, J. Li, H. Zhou, H. Qian, Z. Lin and H. Chen, *Chem. Commun.*, 2019, **55**, 1458–1461.
- 359 H. Chen, H. Tu, C. Hu, Y. Liu, D. Dong, Y. Sun, Y. Dai, S. Wang, H. Qian, Z. Lin and L. Chen, *J. Am. Chem. Soc.*, 2018, **140**, 896–899.
- 360 E. Jin, M. Asada, Q. Xu, S. Dalapati, M. A. Addicoat, M. A. Brady, H. Xu, T. Nakamura, T. Heine, Q. Chen and D. Jiang, *Science*, 2017, **676**, 673–676.
- 361 Z. Guo, Y. Zhang, Y. Dong, J. Li, S. Li, P. Shao, X. Feng and B. Wang, *J. Am. Chem. Soc.*, 2019, **141**, 1923–1927.
- 362 Q. Xu, S. Tao, Q. Jiang and D. Jiang, *J. Am. Chem. Soc.*, 2018, **140**, 7429–7432.
- 363 K. Jeong, S. Park, G. Y. Jung, S. H. Kim, Y. H. Lee, S. K. Kwak and S. Y. Lee, *J. Am. Chem. Soc.*, 2019, **141**, 5880–5885.
- 364 G. Zhang, Y. L. Hong, Y. Nishiyama, S. Bai, S. Kitagawa and S. Horike, *J. Am. Chem. Soc.*, 2019, **141**, 1227–1234.

- 365 M. Liu, L. Chen, S. Lewis, S. Y. Chong, M. A. Little, T. Hasell, I. M. Aldous, C. M. Brown, M. W. Smith, C. A. Morrison, L. J. Hardwick and A. I. Cooper, *Nat. Commun.*, 2016, **7**, 1–9.
- 366 A. Petronico, T. P. Money Penny, B. G. Nicolau, J. S. Moore, R. G. Nuzzo and A. A. Gewirth, *J. Am. Chem. Soc.*, 2018, **140**, 7504–7509.
- 367 T. Tozawa, J. T. A. Jones, S. I. Swamy, S. Jiang, D. J. Adams, S. Shakespeare, R. Clowes, D. Bradshaw, T. Hasell, S. Y. Chong, C. Tang, S. Thompson, J. Parker, A. Trewin, J. Bacsá, A. M. Z. Slawin, A. Steiner and A. I. Cooper, *Nat. Mater.*, 2009, **8**, 973–978.
- 368 E. Zhao, K. Nie, X. Yu, Y. S. Hu, F. Wang, J. Xiao, H. Li and X. Huang, *Adv. Funct. Mater.*, 2018, **28**, 1–21.
- 369 J. P. Robinson, P. D. Kichambare, J. L. Deiner, R. Miller, M. A. Rottmayer and G. M. Koenig, *J. Am. Ceram. Soc.*, 2018, **101**, 1087–1094.
- 370 E. Hirose, K. Niwa, K. Kataoka, J. Akimoto and M. Hasegawa, *Mater. Res. Bull.*, 2018, **107**, 361–365.
- 371 S. Wenzel, S. Randau, T. Leichtweiß, D. A. Weber, J. Sann, W. G. Zeier and J. Janek, *Chem. Mater.*, 2016, **28**, 2400–2407.
- 372 S. Wenzel, T. Leichtweiss, D. Krüger, J. Sann and J. Janek, *Solid State Ionics*, 2015, **278**, 98–105.
- 373 A. Schwöbel, R. Hausbrand and W. Jaegermann, *Solid State Ionics*, 2015, **273**, 51–54.
- 374 S. Wenzel, D. A. Weber, T. Leichtweiss, M. R. Busche, J. Sann and J. Janek, *Solid State Ionics*, 2016, **286**, 24–33.
- 375 K. N. Wood, K. X. Steirer, S. E. Hafner, C. Ban, S. Santhanagopalan, S. H. Lee and G. Teeter, *Nat. Commun.*, 2018, **9**, 1–10.
- 376 D. Liu, Z. Shadike, R. Lin, K. Qian, H. Li, K. Li, S. Wang, Q. Yu, M. Liu, S. Ganapathy, X. Qin, Q. H. Yang, M. Wagemaker, F. Kang, X. Q. Yang and B. Li, *Adv. Mater.*, 2019, **31**, 1–57.
- 377 C. Wang, Y. Gong, J. Dai, L. Zhang, H. Xie, G. Pastel, B. Liu, E. Wachsmann, H. Wang and L. Hu, *J. Am. Chem. Soc.*, 2017, **139**, 14257–14264.
- 378 M. Liu, Z. Cheng, K. Qian, T. Verhallen, C. Wang and M. Wagemaker, *Chem. Mater.*, 2019, **31**, 4564–4574.
- 379 Q. Li, T. Yi, X. Wang, H. Pan, B. Quan, T. Liang, X. Guo, X. Yu, H. Wang, X. Huang, L. Chen and H. Li, *Nano Energy*, 2019, **63**, 103895.
- 380 C. Chen, J. F. M. Oudenhoven, D. L. Danilov, E. Vezhlev, L. Gao, N. Li, F. M. Mulder, R. A. Eichel and P. H. L. Notten, *Adv. Energy Mater.*, 2018, **8**, 1–11.
- 381 I. Hanghofer, B. Gadermaier and H. M. R. Wilkening, *Chem. Mater.*, 2019, **31**, 4591–4597.
- 382 J. Zheng, M. Tang and Y. Y. Hu, *Angew. Chemie - Int. Ed.*, 2016, **55**, 12538–12542.
- 383 G. L. Xu, H. Sun, C. Luo, L. Estevez, M. Zhuang, H. Gao, R. Amine, H. Wang, X. Zhang, C. J. Sun, Y. Liu, Y. Ren, S. M. Heald, C. Wang, Z. Chen and K. Amine, *Adv. Energy Mater.*, 2019, **9**, 1–14.
- 384 M. Nakayama, S. Wada, S. Kuroki and M. Nogami, *Energy Environ. Sci.*, 2010, **3**, 1995–2002.
- 385 F. Li, J. Li, F. Zhu, T. Liu, B. Xu, T. H. Kim, M. J. Kramer, C. Ma, L. Zhou and C. W. Nan, *Matter*, 2019, **1**, 1001–1016.
- 386 Y. Zheng, Y. Li, T. Wu, C. Zhao, W. Zhang, J. Zhu, Z. Li, J. Chen, J. Wang, B. Yu and J. Zhang, *Nano Energy*, 2019, **62**, 521–529.
- 387 Y. Zheng, Y. Li, T. Wu, W. Zhang, J. Zhu, Z. Li, J. Chen, B. Yu, J. Wang and J. Zhang, *Nano Energy*, 2018, **51**, 711–720.
- 388 X. Liu and L. Gu, *Small Methods*, 2018, **2**, 1800006.
- 389 Y. Gong, J. Zhang, L. Jiang, J. A. Shi, Q. Zhang, Z. Yang, D. Zou, J. Wang, X. Yu, R. Xiao, Y. S. Hu, L. Gu, H. Li and L. Chen, *J. Am. Chem. Soc.*, 2017, **139**, 4274–4277.
- 390 Z. Wang, D. Santhanagopalan, W. Zhang, F. Wang, H. L. Xin, K. He, J. Li, N. Dudney and Y. S. Meng, *Nano Lett.*, 2016, **16**, 3760–3767.
- 391 Y. Li, Y. Li, A. Pei, K. Yan, Y. Sun, C. L. Wu, L. M. Joubert, R. Chin, A. L. Koh, Y. Yu, J. Perrino, B. Butz, S. Chu and Y. Cui, *Science (80-.)*, 2017, **358**, 506–510.
- 392 Y. Li, W. Huang, Y. Li, A. Pei, D. T. Boyle and Y. Cui, *Joule*, 2018, **2**, 2167–2177.
- 393 M. J. Zachman, Z. Tu, S. Choudhury, L. A. Archer and L. F. Kourkoutis, *Nature*, 2018, **560**, 345–349.
- 394 F. Sun, K. Dong, M. Osenberg, A. Hilger, S. Risse, Y. Lu, P. H. Kamm, M. Klaus, H. Markötter, F. García-Moreno, T. Arlt and I. Manke, *J. Mater. Chem. A*, 2018, **6**, 22489–22496.
- 395 L. Zhang, T. Yang, C. Du, Q. Liu, Y. Tang, J. Zhao, B. Wang, T. Chen, Y. Sun, P. Jia, H. Li, L. Geng, J. Chen, H. Ye, Z. Wang, Y. Li, H. Sun, X. Li, Q. Dai, Y. Tang, Q. Peng, T. Shen, S. Zhang, T. Zhu and J. Huang, *Nat. Nanotechnol.*, 2020, **15**, 94–98.
- 396 X. Liu, D. Wang, G. Liu, V. Srinivasan, Z. Liu, Z. Hussain and W. Yang, *Nat. Commun.*, 2013, **4**, 1–8.
- 397 Y. Li, X. Chen, A. Dolocan, Z. Cui, S. Xin, L. Xue, H. Xu, K. Park and J. B. Goodenough, *J. Am. Chem. Soc.*, 2018, **140**, 6448–6455.
- 398 Y. Zhou, M. Su, X. Yu, Y. Zhang, J. G. Wang, X. Ren, R. Cao, W. Xu, D. R. Baer, Y. Du, O. Borodin, Y. Wang, X. L. Wang, K. Xu, Z. Xu, C. Wang and Z. Zhu, *Nat. Nanotechnol.*, 2020, **15**, 224–230.
- 399 A. M. Nolan, Y. Zhu, X. He, Q. Bai and Y. Mo, *Joule*, 2018, **2**, 2016–2046.
- 400 S. Siculo, C. Kalcher, S. J. Sedlmaier, J. Janek and K. Albe, *Solid State Ionics*, 2018, **319**, 83–91.
- 401 Z. Deng, B. Radhakrishnan and S. P. Ong, *Chem. Mater.*, 2015, **27**, 3749–3755.
- 402 P. Sivaraj, K. P. Abhilash, B. Nalini, P. Perumal, K. Somasundaram and P. C. Selvin, *Macromol. Res.*, 2020, **28**, 739–750.
- 403 M. A. Webb, Y. Jung, D. M. Pesko, B. M. Savoie, U. Yamamoto, G. W. Coates, N. P. Balsara, Z. G. Wang and T. F. Miller, *ACS Cent. Sci.*, 2015, **1**, 198–205.
- 404 V. Sethuraman, S. Mogurampelly and V. Ganesan, *Soft Matter*, 2017, **13**, 7793–7803.
- 405 X. He, Y. Zhu and Y. Mo, *Nat. Commun.*, 2017, **8**, 1–7.
- 406 Y. Mo, S. P. Ong and G. Ceder, *Chem. Mater.*, 2012, **24**, 15–17.
- 407 X. He, Y. Zhu, A. Epstein and Y. Mo, *npj Comput. Mater.*, 2018, **4**, 1–9.
- 408 I. Rahwan, M. Cebrian, N. Obradovich, J. Bongard, J. F. Bonnefon, C. Breazeal, J. W. Crandall, N. A. Christakis, I. D.

- Couzin, M. O. Jackson, N. R. Jennings, E. Kamar, I. M. Kloumann, H. Larochele, D. Lazer, R. McElreath, A. Mislove, D. C. Parkes, A. ‘Sandy’ Pentland, M. E. Roberts, A. Shariff, J. B. Tenenbaum and M. Wellman, *Nature*, 2019, **568**, 477–486.
- 409 K. T. Butler, D. W. Davies, H. Cartwright, O. Isayev and A. Walsh, *Nature*, 2018, **559**, 547–555.
- 410 C. F. Hirjibehedin, *Nature*, 2020, **577**, 320–321.
- 411 G. H. Gu, J. Noh, I. Kim and Y. Jung, *J. Mater. Chem. A*, 2019, **7**, 17096–17117.
- 412 P. M. Attia, A. Grover, N. Jin, K. A. Severson, T. M. Markov, Y. H. Liao, M. H. Chen, B. Cheong, N. Perkins, Z. Yang, P. K. Herring, M. Aykol, S. J. Harris, R. D. Braatz, S. Ermon and W. C. Chueh, *Nature*, 2020, **578**, 397–402.
- 413 A. Kilic, Ç. Odabaşı, R. Yildirim and D. Eroglu, *Chem. Eng. J.*, 2020, **390**, 124117.
- 414 X. Chen, H. Lei, R. Xiong, W. Shen and R. Yang, *Appl. Energy*, 2019, **255**, 113758.
- 415 X. Song, F. Yang, D. Wang and K. L. Tsui, *IEEE Access*, 2019, **7**, 88894–88902.
- 416 X. Chen, H. Yang, J. Wun, C. Wang and L. Li, *Energy Explor. Exploit.*, 2020, DOI: 10.1177/0144598720911724.
- 417 K. A. Severson, P. M. Attia, N. Jin, N. Perkins, B. Jiang, Z. Yang, M. H. Chen, M. Aykol, P. K. Herring, D. Fraggadakis, M. Z. Bazant, S. J. Harris, W. C. Chueh and R. D. Braatz, *Nat. Energy*, 2019, **4**, 383–391.
- 418 A. D. Sendek, E. D. Cubuk, E. R. Antoniuk, G. Cheon, Y. Cui and E. J. Reed, *Chem. Mater.*, 2019, **31**, 342–352.
- 419 Z. Ahmad, T. Xie, C. Maheshwari, J. C. Grossman and V. Viswanathan, *ACS Cent. Sci.*, 2018, **4**, 996–1006.
- 420 N. A. Katcho, J. Carrete, M. Reynaud, G. Rousse, M. Casas-Cabanas, N. Mingo, J. Rodríguez-Carvajal and J. Carrasco, *J. Appl. Crystallogr.*, 2019, **52**, 148–157.
- 421 C. Chen, Z. Lu and F. Ciucci, *Sci. Rep.*, 2017, **7**, 1–8.
- 422 M. Sumita, R. Tamura, K. Homma, C. Kaneta and K. Tsuda, *Bull. Chem. Soc. Jpn.*, 2019, **92**, 1100–1106.
- 423 B. Liu, J. Yang, H. Yang, C. Ye, Y. Mao, J. Wang, S. Shi, J. Yang and W. Zhang, *J. Mater. Chem. A*, 2019, **7**, 19961–19969.
- 424 K. Nagao, A. Hayashi and M. Tatsumisago, *J. Ceram. Soc. Japan*, 2016, **124**, 915–919.